Materials Horizons

ROYAL SOCIETY OF CHEMISTRY

REVIEW

View Article Online
View Journal

Check for updates

Cite this: DOI: 10.1039/d6mh00047a

Navigating the labyrinth of isotropic wrinkling: design, fabrication, characterization, and applications

Zain Ahmad and João T. Cabral *

Received 9th January 2026,
Accepted 27th March 2026

DOI: 10.1039/d6mh00047a

rsc.li/materials-horizons

Naturally occurring surfaces exhibit remarkable labyrinthine patterns across scales, from butterfly wings to brain corals. These undulated, highly periodic patterns display defined wavelength and amplitude, with distinctive short-range uniaxial order and long-range isotropic order. This review explores isotropic wrinkles that emerge when a stiff film on a compliant substrate experiences uniform compressive stress in all directions. We categorize their origin and corresponding fabrication approaches, based on the mechanism of stress application in bilayer systems: thermal, light-induced, solvent-mediated, mechanical, chemical, and electrical methods. We discuss analytical techniques for characterizing these complex patterns, including Fourier transform analysis across scales, local coordination, and persistence length measurements. Each approach offers unique opportunities for controlling pattern formation, enabling the tailoring of surface morphologies for specific functional applications, spanning anti-counterfeiting to flexible electronics. Additionally, we explore the evolution of isotropic wrinkles into more complex morphologies, including creases, folds, and hierarchical architectures. Looking forward, we discuss the integration of material design with controlled wrinkling strategies and opportunities for next-generation functional surfaces and skins.

Wider impact

Surface wrinkling has fascinated physicists and engineers, who are interested in applying the fundamentals of morphogenesis and biomimetics to their technological applications. Isotropic wrinkling arises when a thin stiff skin attached to a soft compressible substrate undulates with an exceptionally regular wavelength and amplitude, yielding a pattern with local 1D order but no long-range order. The term derives from the Greek ''isos'' (equal) and ''tropos'' (direction), and such isotropic wrinkling patterns are sometimes referred to as ''labyrinthine'', ''random'', or ''spinodal'', appearing 'polycrystalline' with 'grains' of multiple orientations. We consider the fundamental definitions and theory, classes of fabrication approaches, and fields of technological applications of isotropic wrinkling. A range of thermal, light, mechanical, chemical and electrical fields have been demonstrated to yield exceptional surface patterning and functions over multiple scales and material types. The tuneability, dynamics and responsiveness of the patterns have been exploited in a variety of applications in sensors, electronics and photonics, tuneable colour, camouflage and anti-counterfeiting, wetting, spreading and drag control, antimicrobial action and material property measurements. We conclude by highlighting the need for greater rigor in the analysis of isotropic wrinkling and the opportunities in emerging technologies.

1 Introduction

Nature exhibits an extraordinary diversity of spatio-temporal patterns across various scales and systems (organic, inorganic and hybrid) from sand dunes and snowflakes to animal pigmentation and shell morphologies.[1–4] A significant class of such patterns is the labyrinthine structure, which has fascinated humans since ancient times, epitomized by the mythological maze of Daedalus designed to contain the Minotaur.[5] These patterns combine local order with global disorder, exhibiting regularity at short scales while being complex and irregular over larger areas.[6,7]

Labyrinthine patterns appear across diverse natural contexts and provide specialized functions. Butterfly wings, for instance, can yield omnidirectional anti-reflection properties through randomly arranged nanopillars (Fig. 1a and b);[8] brain corals facilitate seawater circulation while preventing harmful depositions (Fig. 1c);[9] camouflage emerges in puffer fish skin *via* blending of simpler motifs (Fig. 1d);[10] vegetation self-organizes in arid regions as a resource adaptation strategy (Fig. 1e),[11] akin to the resilience afforded to maze-like mussel bed ecosystems.[12]

Department of Chemical Engineering, Imperial College London, London SW7 2AZ, UK. E-mail: j.cabral@imperial.ac.uk

Open Access Article. Published on 31 March 2026. Downloaded on 4/22/2026 5:53:25 AM. This article is licensed under a Creative Commons Attribution 3.0 Unported Licence.

Open Access Article. Published on 31 March 2026. Downloaded on 4/22/2026 5:53:25 AM.
This article is licensed under a Creative Commons Attribution 3.0 Unported Licence.

Similar self-organized patterns emerge in swirling fungal skin infections,[13] and in calcification and mineralization in fundamental physiological processes.[14] The scale of these natural patterns spans several orders of magnitude, from hundreds of nanometers in the anti-reflective structures of butterfly wings to hundreds of meters in vegetation patterns observed through satellite imagery. A defining characteristic of these patterns is their distinctive isotropic spatial organization, manifested by a ring-like distribution in Fourier power spectra, indicative of their nontrivial symmetries (Fig. 1b and e insets) along with local pattern ordering.[15,16] The morphogenesis of labyrinthine patterns has been examined experimentally and theoretically across a range of disciplines,[17–19] encompassing stable configurations, such as domains in ferromagnetic and superconducting films, as well as non-equilibrium conditions, notably those generated by reaction–diffusion systems exhibiting Turing patterns.[20–23] Laboratory observations span diverse systems including Langmuir monolayers,[24] microemulsions,[25] cholesteric liquid crystals,[26] ferrofluids,[27] and polymeric films,[28] with characteristic scales varying from nanometers to centimeters (Fig. 1f(i)), whose universality has motivated mathematical frameworks like the Swift–Hohenberg model,[29–31] which captures the essential features of pattern formation across disciplines from fluid dynamics[31] and surface wrinkling,[32] to optics[33] and ecology.[34]

Surface wrinkling is a versatile and scalable route to generating self-organized, highly ordered, micro- and nanoscale structures.[37,38] Wrinkling occurs when a stiff layer on a compliant substrate (the composite system usually referred to as 'bilayer') experiences compressive stresses beyond a critical threshold.[39] Wrinkling is ubiquitous in everyday life, from human skin, to the shriveled textures of dried fruits.[40–42] While wrinkling or buckling are often detrimental to 'performance' in various contexts,[43–45] such as 'sun kinks' in rail tracks,[46] undulations in aircraft fuselages,[47] or shell buckling in composite fuel tanks,[48,49] it can also provide a powerful and versatile approach for surface structuring. By contrast with conventional top-down patterning approaches such as lithography, hot pressing, or printing, surface wrinkling spontaneously emerges from mechanical instabilities, offering a simple, cost-effective and scalable approach to creating functional patterns down to the nanoscale, without resorting to clean rooms or specialized equipment. The ability to exploit such instabilities has unlocked applications in flexible electronics,[50,51] smart adhesives,[52] antifouling coatings,[53,54] photonic devices,[55] biocompatible interfaces,[56] thin-film property measurements,[57,58] and microfluidic systems,[59] as well as in tuning the wettability,[60] mechanical sensitivity,[61] and optical functionality[62,63] of surfaces and coatings.

Labyrinthine wrinkling patterns emerge when stiff-soft bilayers experience isotropic compressive stress fields, yielding surface patterns with well-defined wavelength and amplitude lacking long-range orientational order. The term 'isotropic' derives from the Greek words isos (equal) and tropos (direction or way), meaning 'equal in all directions', which aptly reflects the omnidirectional stress fields that generate these patterns. Such wrinkles self-organize into domains with distinct local alignments, resembling a polycrystalline material composed of multiple orientational ''grains'' (Fig. 2). Their global rotational invariance appears as a characteristic circular ring in reciprocal space, in a scattering pattern or upon fast Fourier transform (FFT) analysis of labyrinthine morphology (Fig. 2d). Isotropic wrinkling is the energetically favored response of bilayer systems to nondirectional compressive stress,[37,64] and is thus prevalent across diverse experimental conditions, material systems, and length scales.[65,66] Controlled anisotropic patterns, such as unidirectional, herringbone, or checkerboard arrangements, are achieved only through deliberate interventions that break the inherent symmetry of the system, including directional stretching, templating with patterned substrates, imposition of geometric confinement, or due to anisotropic material

Zain Ahmad

Zain Ahmad is a Research Associate in Chemical Engineering at Imperial College London. His research focuses on surface engineering, functional coatings, and structured soft materials, with particular interest in wrinkling, nanocellulose-based films, and stimuli-responsive interfaces. His work integrates experimental design, micro/nanofabrication, and modelling to understand and control interfacial phenomena in applications ranging from antimicrobial coatings to cleaning and sensing. Zain completed his PhD at Imperial College London and has an MSc from KAUST and a BTech from IIT Kharagpur.

João T. Cabral

João T. Cabral is a Professor of Chemical Engineering at Imperial College London (UK). He graduated in Engineering Physics (IST, Lisbon, Portugal), obtained a PhD in polymer blend thermodynamics at Imperial, joined NIST (USA) as a postdoc, and held various visiting positions at the Universities of Chicago (USA), IST Lisbon (Portugal), and Fudan (China). João leads the Soft Matter Engineering laboratory, collaborating closely with industry to develop sustainable materials and processes from the molecular to macroscales. João currently holds a P&G/Royal Academy of Engineering research chair and chairs the UK Polymer Physics group (IoP/RSC).

This journal is © The Royal Society of Chemistry 2026

Open Access Article. Published on 31 March 2026. Downloaded on 4/22/2026 5:53:25 AM.
This article is licensed under a Creative Commons Attribution 3.0 Unported Licence.

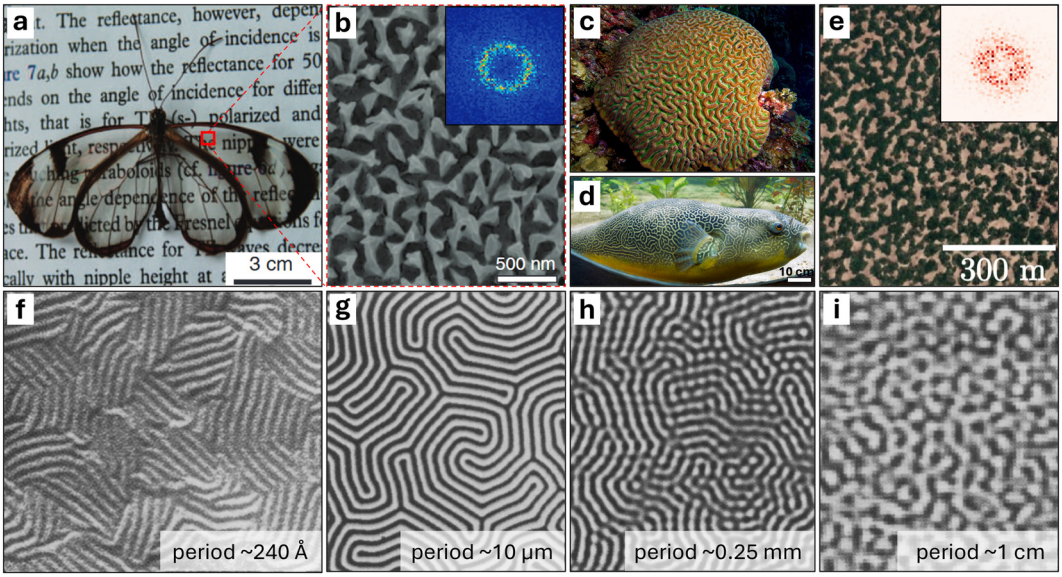

Fig. 1 (a) A glasswing butterfly (*Greta oto*) on a piece of paper displaying its transparent wings. (b) A scanning electron microscope (SEM) image of the transparent region of the butterfly's wings revealing randomly oriented nanopillars. The inset is the two-dimensional Fourier power spectrum of the imaged nanostructure. (a) and (b) Adapted with permission.[8] © 2015, Springer Nature. (c) Brain coral (*Colpophyllia natans*) exhibiting natural labyrinthine surface morphology. Image by Nick Hobgood, licensed under CC BY-SA 3.0.[35] (d) Giant freshwater puffer fish (*Tetraodon mbu*) displaying intricate labyrinthine skin pigmentation patterns. Image by Chiswick Chap, licensed under CC BY-SA 3.0.[36] (e) Satellite imagery showing self-organized vegetation patterns in Niger. The inset displays the corresponding Fourier transform analysis. Adapted with permission.[11] © 2023, American Physical Society. (f) Freeze-fracture electron microscopy reveals the spontaneous organization of phospholipids into vesicular structures. (g) Magnetic domain patterns in ferromagnetic garnet film (grown on gadolinium gallium garnet) visualized through the Faraday magneto-optic effect. (h) Chemical reaction–diffusion system exhibiting stationary Turing patterns, observed through differential light absorption patterns. (i) Dynamic CO_2 gas fluctuations during Rayleigh–Bénard instability captured using shadowgraph imaging. The insets in (f)–(i) show the characteristic scale or period of their respective patterns. (f)–(i) Adapted with permission.[22] © 1995, American Association for the Advancement of Science.

properties.[67,68] Thus, isotropic wrinkling serves as the foundational reference state from which all other wrinkle morphologies deviate, making its comprehensive understanding essential for advancing the field.[39] Furthermore, isotropic wrinkles exhibit unique advantages for applications requiring omnidirectional properties and direction-independent functionality, including optical coatings for structural color and anti-reflective films,[69] biomedical surfaces promoting unbiased cell adhesion,[70] abrasion resistant superoleophilic surfaces,[71] light-trapping in energy devices,[72] mechanically robust strain-accommodating platforms in stretchable electronics,[51] or acoustic metamaterials employed in uniform sound control.[73]

A number of excellent reviews have considered the field of surface wrinkling,[39,41,75,76] and specialized aspects of anisotropic patterning,[67,77–79] dynamic wrinkling,[68,80–83] bio-based wrinkled surfaces,[84] non-planar surfaces,[85,86] wrinkling suppression,[87] hierarchical structures,[88] and applications in sensors,[89,90] electronics,[91] optics,[92] and material property measurements.[57] Here, we focus on ubiquitous 'isotropic wrinkling', which is referred to using various terminology throughout the literature, including "random",[93] "disordered zigzag-based herringbone",[94] "random labyrinth",[95] and "spinodal"[96] patterns, among others. For consistency, we refer to the process as isotropic wrinkling and the resulting morphology as labyrinthine patterns. We begin the review by introducing the fundamentals of wrinkling in Section 2. Section 3 examines various instability routes employed to excite isotropic wrinkling, including thermal, light, solvent, mechanical, chemical, and electrical approaches. Section 4 addresses quantitative assessment methods for isotropic wrinkles, including wavelength determination, domain analysis, and characterization of persistence length. The practical applications of isotropic wrinkles in areas ranging from anti-counterfeiting, dynamic surface modification, tunable material properties, and flexible electronics are discussed in Section 5. Section 6 explores the hierarchical nature of isotropic wrinkles and their transition to more complex morphologies encompassing folds and cracks, while Section 7 concludes with an outlook.

2 Wrinkling mechanics

Understanding the fundamental mechanics of wrinkling and buckling is required to predict and control the formation of labyrinthine patterns. This quest has deep historical roots. Roman architects empirically discovered optimal column dimensions through trial and error, with Vitruvius (1st century BC) establishing rules relating column diameter to height that ensured structural integrity across the monumental architecture of the empire.[97] The first study of column buckling is believed to be that of Petrus van Musschenbroek (1729),[98] followed by Leonhard Euler (1744), who formalized the

Open Access Article. Published on 31 March 2026. Downloaded on 4/22/2026 5:53:25 AM.
This article is licensed under a Creative Commons Attribution 3.0 Unported Licence.

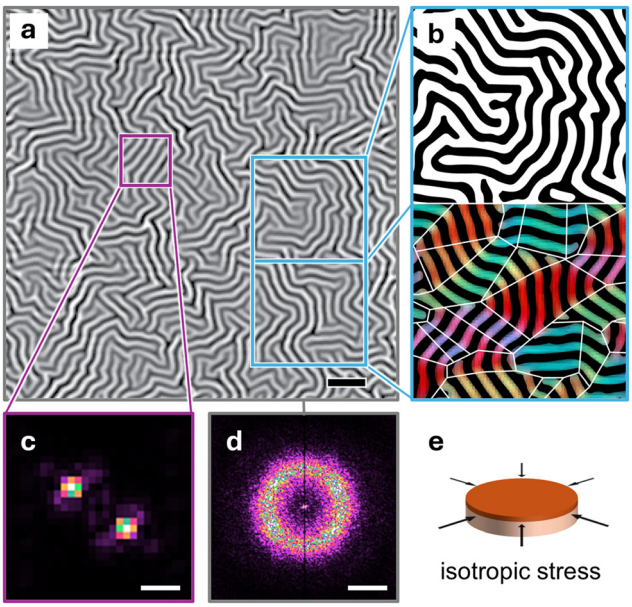

Fig. 2 (a) AFM topography image showing representative isotropic wrinkles (scale bar: 10 μm). The boxed regions highlight areas for analysis. (b) Image processing of the wrinkled surface: upper panel shows threshold ridges for enhanced visualization of wrinkle topology, while the lower panel presents directional segmentation using color coding to represent different wrinkle orientations (analyzed with the OrientationJ[74] plugin in ImageJ), with polygon construction delineating regions of unidirectional wrinkle alignment. (c) Two-dimensional fast Fourier transform (FFT) of a small region containing aligned wrinkles reveals discrete spots corresponding to the dominant orientation, while (d) the 2D FFT of the entire image produces a uniform circular ring, confirming the global isotropic nature of the pattern (scale bar: 0.5 μm^{-1}). (e) Schematic diagram demonstrating the omnidirectional nature of stress fields (indicated by arrows) applied to a circular specimen.

mathematics of elastic curves and derived the celebrated critical load for column buckling.[99,100] Euler's counter-intuitive insight that structures fail not because of material weakness but because of geometric instabilities challenged prevailing engineering thoughts and was initially met with skepticism. By the mid-20th century, this understanding had evolved into rigorous elasticity frameworks: Biot's linear stability analysis of compressed elastic layers,[101,102] Landau and Lifshitz's general theory of elasticity,[103] and Allen's engineering analyses of sandwich structures.[104] Together, these lay the theoretical foundations and physical understanding that underpin the past three decades of research in surface wrinkling and buckling.

2.1 Linear framework and characteristic scales

Labyrinthine patterns consist of locally ordered domains within a globally disordered network, where the cross-sectional morphology is characterized by sinusoidal undulations with wavelength λ and amplitude A (Fig. 3). Surface wrinkling in bilayer systems can be described by theoretical frameworks developed through both force balance and energy balance approaches.[65,105–107] The force balance approach for a bilayer provides a direct method for analyzing wrinkling mechanics by considering the competing contributions of two primary

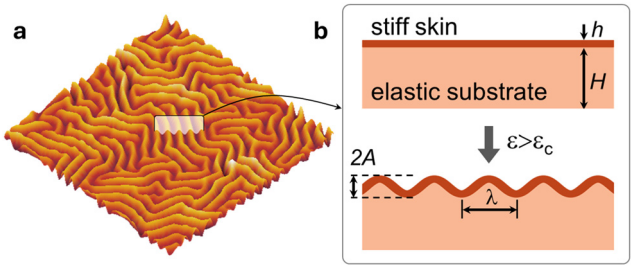

Fig. 3 (a) Three-dimensional reconstruction of representative isotropic wrinkles generated using Gwyddion software. (b) Cross-sectional schematic of the bilayer wrinkling system showing a stiff skin layer (thickness h) bonded to a compliant elastic substrate (thickness H). The bilayer system experiencing compressive strain exceeding the critical buckling threshold ($\varepsilon > \varepsilon_c$) undergoes a wrinkling instability, forming periodic sinusoidal wrinkles characterized by wavelength λ and amplitude A.

forces that oppose each other: the force that resists the bending of the film and the force that opposes elastic deformation of the substrate. The bending resistance force of the film ($F_{B,f}$) and the substrate deformation force ($F_{D,s}$) can be written as,

$$F_{B,f} = E_s\left(\frac{\pi}{\lambda}\right)^2 \frac{wh^3}{3(1-\nu_s^2)} \quad (1)$$

$$F_{D,s} = \left(\frac{\lambda}{\pi}\right)^2 \frac{E_f w}{4(1-\nu_f^2)} \quad (2)$$

where E_s and E_f are the elastic moduli, ν_s and ν_f are the Poisson's ratios of the substrate and film, respectively, h is the film thickness, and w its width. The total force acting on the film is thus,[41]

$$\begin{aligned} F &= F_{B,f} + F_{D,s} \\ &= E_s\left[\left(\frac{\pi}{\lambda}\right)^2 \frac{wh^3}{3(1-\nu_s^2)} + \frac{\lambda}{4\pi}\frac{E_f w}{(1-\nu_f^2)E_s}\right] \end{aligned} \quad (3)$$

Minimizing this force with respect to wavelength ($dF/d\lambda = 0$) yields the fundamental scaling relationships that govern the resulting sinusoidal wrinkling profiles, with wavelength and amplitude:

$$\lambda = 2\pi h\left(\frac{\bar{E}_f}{3\bar{E}_s}\right)^{1/3} \quad (4)$$

$$A = h\left(\frac{\varepsilon}{\varepsilon_c} - 1\right)^{1/2} \quad (5)$$

where $\bar{E} = \dfrac{E}{1-\nu^2}$ is the plane strain modulus (of substrate or film), ε is the applied strain, and

$$\varepsilon_c = \frac{1}{4}\left(\frac{3\bar{E}_s}{\bar{E}_f}\right)^{2/3} \quad (6)$$

is a critical strain that must be exceeded in order to trigger the wrinkling instability. The critical strain relationship is obtained by evaluating the minimum force condition and relating the resulting stress ($\sigma = F/\text{area}$) to strain through elastic theory. Below this threshold, the system can accommodate the strain

This journal is © The Royal Society of Chemistry 2026

Open Access Article. Published on 31 March 2026. Downloaded on 4/22/2026 5:53:25 AM.
This article is licensed under a Creative Commons Attribution 3.0 Unported Licence.

through uniform compression without developing surface undulations. The amplitude scaling emerges from enforcing conservation of the film contour length during wrinkling, combined with the constraint of sinusoidal displacement profiles.

These scaling relationships propose a few simple design principles: pattern wavelength, λ, scales linearly with film thickness h_f, but is independent of strain ε; it varies with the cubic root of the modulus ratio, making it relatively insensitive to material property variations. By contrast, the pattern amplitude grows with the square root of excess strain, beyond the critical threshold, ε_c. In short, one can design a pattern wavelength λ by selecting h_f, and separately adjusting the amplitude using ε. This so-called 'low-deformation' theory predicts wavelength-independence from strain, while experimental observations show slight wavelength reduction with increasing strain, though this effect remains small for strains below approximately 10%, above which a 'large deformation' model[108] becomes appropriate. The predictive nature of bi- (or multi-)layer wrinkling enables thus the quantitative design of surface morphologies with prescribed wavelength and amplitude, through the selection of materials and strain fields. In elastically reversible systems, applied strain can be modulated continuously to achieve tunable, stimuli-responsible and reconfigurable structures.[80–83] Deliberate gradients in film thickness or modulus within a single substrate can further give rise to spatially graded patterns.[109–113]

2.2 Energy framework and wrinkle selection

The energy-based framework provides complementary insights into wrinkle formation mechanics. When a film develops wrinkles with wavelengths significantly exceeding its thickness, the system can be adequately described using the Föppl–von Kármán nonlinear plate equations.[66,103] This approach relates membrane forces, denoted as $N_{\alpha\beta}$, to membrane strains, $\varepsilon_{\alpha\beta}$, through Hooke's law, establishing a foundation for comprehensive energetic analysis.[66,103,114]

Building on the work of Cerda and Mahadevan,[42] and Chen and Hutchinson,[115] Huang *et al.*[66] write the total energy of the film–substrate bilayer system as a function of the amplitude of the wrinkle A,[66,115] taking the general form,

$$U = U^0 + \xi(h\bar{E}_f\Phi - |N_{11}^0|)A^2 + \zeta A^4 \quad (7)$$

where ξ, ζ, and Φ are dependent on λ, and system parameters, h, H, $\bar{E}_f$, $\bar{E}_s$ and ν_s. N_{11}^0 represents the initial membrane force, and U^0 denotes the baseline energy state. This formulation reveals the bifurcation behavior characteristic of wrinkling instabilities. When the membrane force magnitude remains below the threshold $|N_{11}^0| < h\bar{E}_f\Phi$, the energy landscape exhibits a global minimum at $A = 0$, maintaining the film in a stable, flat, configuration (Fig. 4a(i)). Conversely, when compressive forces exceed this critical value ($|N_{11}^0| > h\bar{E}_f\Phi$), the flat configuration becomes a local energy maximum, while the bilayer structure spontaneously develops wrinkles with equilibrium amplitude A_{eq} that minimize the total energy (Fig. 4a(ii)). The equilibrium wavelength remains invariant with respect to the applied membrane force, and persists as the amplitude evolves.

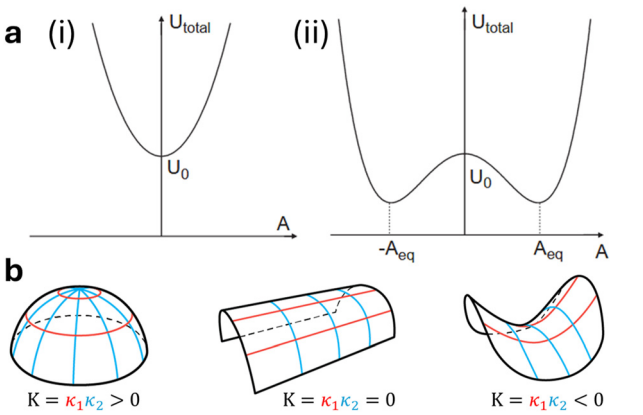

Fig. 4 (a) Energy diagrams as a function of wrinkle amplitude A illustrating the stability in thin films. (i) Below the critical strain threshold, the total energy exhibits a minimum at $A = 0$, corresponding to a stable flat film configuration. (ii) When the strain exceeds the critical threshold, the flat state becomes energetically unstable (local maximum at $A = 0$), while the system develops wrinkles with equilibrium amplitude A_{eq}. Adapted with permission.[66] © 2005, American Society of Mechanical Engineers. (b) Illustration of Gaussian curvature (K) calculated as the product of principal curvatures κ_1 and κ_2 (indicated by blue and red lines) for three fundamental surface geometries: spherical dome (positive curvature), cylindrical surface (zero curvature), and saddle-shaped surface (negative curvature).

While the force balance derivation presented earlier assumed infinitely thick substrates ($h \gg H$, as $H \to \infty$), the energy-based analysis by Huang and coworkers[66] extends these results to systems with finite substrate thickness, broadening the applicability of wrinkling theory to diverse experimental configurations.[66] Beyond establishing characteristic length scales through wavelength and amplitude relationships, the energy framework is useful to understand how wrinkle orientation and pattern morphology emerge from the interplay between strain directionality and energy minimization. The morphological diversity of wrinkled surfaces reflects the response to principal directions of interfacial compressive stress.[94,96,116–119] Uniaxial compression naturally produces parallel stripe patterns aligned perpendicularly to the compression axis, while biaxial and isotropic stress fields generate increasingly complex arrangements, including herringbone and labyrinthine morphologies. Additional patterns, such as concentric target structures, radial spoke configurations, and checkerboard arrays, emerge from specific stress distributions or substrate modifications that further break the symmetry of the system.

Wrinkling theory generally assumes spatially homogeneous, planar, layered systems. In practice, real substrates invariably contain surface imperfections, including topographical irregularities, chemical heterogeneities, and local variations in film thickness or elastic modulus. Wrinkling is a collective mechanical instability, and in real systems, point and line defects, analogous to minutiae in fingerprint patterns, often nucleate at such heterogeneities or at physical boundaries.[120] The history of application of stress fields can further compound this complexity; simulations have demonstrated that different

Open Access Article. Published on 31 March 2026. Downloaded on 4/22/2026 5:53:25 AM. This article is licensed under a Creative Commons Attribution 3.0 Unported Licence.

loading paths, leading to the same final strain state, can yield distinct wrinkling configurations.[121] Flores-Johnson *et al.*[122] showed, with experiment and simulation, that the size and spatial distribution of physical defects govern the interaction between wrinkling branches emanating from neighboring defect sites. The coupling between geometry, topological defects and disclinations has indeed been examined theoretically and experimentally.[123] Therefore, while homogeneous systems are expected to undergo a uniform, collective, wrinkling instability to satisfy force balance and energy minimization, substrate imperfections, boundaries and patterns can inadvertently (or deliberately) direct nucleation and spatial ordering, and thus reflect in part the defect landscape of the underlying soft substrate.

The energetic basis for pattern selection under varying stress conditions was established through comparative analysis of competing morphologies. Chen and Hutchinson[115] employed finite element calculations to compare the energies associated with stripe patterns (one-dimensional wave-like structures), checkerboard configurations (resembling arrays of spherical caps), and the bent structures characteristic of labyrinthine and herringbone patterns.[115] This analysis demonstrates that labyrinthine and herringbone patterns constitute minimum energy states for films subjected to compressive stresses substantially exceeding the critical threshold. These bent configurations achieve the lowest average elastic energy by effectively relieving biaxial prestress in all directions while minimizing the concurrent development of membrane stretch energy.

The energetic preference for labyrinthine morphologies can be rationalized through geometric considerations of surface curvature. Gaussian curvature, calculated as the product of principal curvatures in orthogonal directions (Fig. 4b), provides a measure of surface geometry that directly relates to membrane strain energy.[124,125] One-dimensional stripe patterns exhibit zero Gaussian curvature, curved along one direction while remaining flat in the perpendicular direction, but this geometry proves incapable of relieving biaxial or isotropic compression. Checkerboard patterns, which curve in two orthogonal directions, can accommodate multi-directional stress but necessarily develop non-zero Gaussian curvature. Since Gaussian curvature requires membrane stretching or compression in flat sheets (a consequence of Gauss' *Theorema Egregium*), checkerboard configurations incur stretch energy penalties.[124,126] Labyrinthine patterns circumvent this constraint by assembling locally one-dimensional segments into interconnected zigzag networks. This architecture enables isotropic stress relief while maintaining nearly zero Gaussian curvature over most of the surface; the sharp directional transitions or ''jogs'' that connect adjacent segments concentrate the required membrane strain into small localized regions, thereby minimizing the area-averaged stretch energy.

The understanding of both linear scaling relationships and the nonlinear energetics of pattern selection establishes the theoretical foundation necessary for the control of wrinkling morphology. In the following sections, we examine the diverse experimental approaches employed to generate isotropic wrinkles through the application of these principles.

3 Fabrication methods

Isotropic wrinkles can be fabricated through various approaches that exploit mechanisms that generate compressive interfacial stresses. Surface wrinkles emerge when a stiff film bonded to a compliant substrate experiences sufficient compressive stress, which can be introduced either during film formation or through subsequent processing. The stress generation mechanism varies across techniques, for instance, in metal deposition, heat generated during the process naturally causes substrate expansion and subsequent contraction, while in mechanical compression approaches, stress can be applied independently of bilayer (or multilayer) formation.

Amongst compliant substrates, elastomers and in particular polydimethylsiloxane (PDMS) elastomers are often the material of choice due to its favorable combination of properties: optical transparency, biocompatibility, tunable mechanical properties ($E_s \approx$ 1–3 MPa through controlled crosslinking) and incompressibility $\nu \simeq 0.5$, chemical stability, and fabrication versatility through spin coating, molding (with nm fidelity), and 3D printing.[127–130] Based on the stress induction mechanism, fabrication methods can be categorized into six distinct groups: thermally, light, solvent, mechanically, chemically, and electrically induced (Fig. 5). Each approach offers unique advantages for controlling wrinkle formation, which we consider next.

3.1 Thermally-induced

Surface wrinkling can be achieved through strain generated by a mismatch in thermal expansion coefficients between a stiff film and its compliant substrate. When subjected to temperature changes, the differential thermal expansion coupled with the modulus mismatch between layers can generate compressive stresses sufficiently large to trigger a wrinkling instability. This section explores various approaches to induce such thermal excursions in bilayer systems, including metal deposition, thermal annealing, temperature-responsive chemical reactions, plasma oxidation, and laser irradiation. We begin with thermal stress induced by metal deposition, as this was the foundational approach that established surface wrinkling as a controlled patterning strategy.[64]

3.1.1 Metal deposition. Whitesides and coworkers[64] discovered that a thin metal coating deposited *via* electron beam evaporation on PDMS could spontaneously form periodic wrinkle patterns upon cooling to room temperature. During deposition, the PDMS substrate undergoes thermal expansion due to heat generated by the process, while the metal film forms. Upon cooling, the substrate contracts while the newly formed metal film, with a significantly lower thermal expansion coefficient, resists contraction, generating compressive stress in the film. Since the thermal expansion and contraction occur without directional constraint, the resulting stress field acts isotropically, producing labyrinthine patterns (Fig. 6a).

 This journal is © The Royal Society of Chemistry 2026

Open Access Article. Published on 31 March 2026. Downloaded on 4/22/2026 5:53:25 AM.
This article is licensed under a Creative Commons Attribution 3.0 Unported Licence.

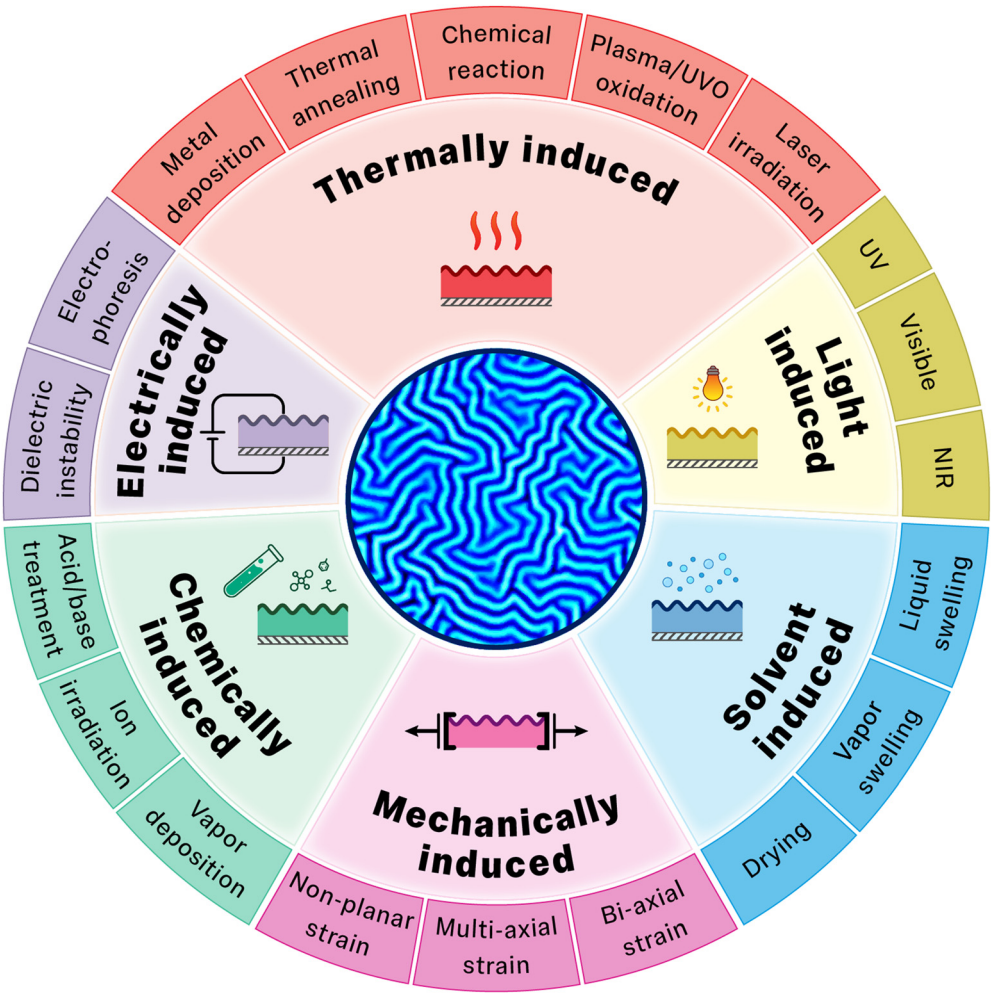

Fig. 5 Schematic illustration of various induction methods to fabricate isotropic wrinkles, categorized into six major approaches.

The thermal mechanism was confirmed by its reversibility: wrinkles disappear upon reheating to the deposition temperature and reappear upon cooling, while metal deposited onto cold PDMS produces no wrinkles. Near substrate edges or around relief structures, geometric constraints break isotropy, leading to locally aligned wrinkle patterns (Fig. 6a(ii)).[64]

Various gradient systems have been explored to understand pattern formation and expand control over wrinkle characteristics, including metal film thickness gradients,[112,136] substrate thickness variations,[113] elasticity gradients,[137] viscoelastic properties of the underlying layer,[111] and even aging effects in unconventional substrates such as vapor-deposited organic films.[138] Wang and coworkers[139] highlighted the importance of deposition sequence by comparing continuous to stepwise deposition, revealing a ''morphology memory effect'' whereby subsequent depositions followed patterns established in previous steps.

Metal deposition is attractive for its simplicity, as wrinkle formation occurs spontaneously upon cooling without requiring complex processing steps. However, the method typically relies on high-vacuum thin-film deposition techniques and specialized equipment, such as thermal evaporation, electron-beam evaporation, or sputtering. While the thermal stress model provides the primary explanation for wrinkle formation, studies have revealed that additional mechanisms can influence or even dominate pattern development in certain systems. Shao and Brook[140] observed that sputtering different metals (Au, Pt, W, Cr) produced wrinkles with varied wavelengths, with gold showing no wrinkle formation despite similar thermal properties. Casper and coworkers[141] demonstrated that chemical modification of the PDMS surface during sputtering can independently drive wrinkle formation through plasma-induced creation of a silica-like surface layer with intrinsic compressive stress. These findings highlight that the interplay between thermal, chemical, and plasma-induced effects can be more complex than initially assumed, requiring careful consideration of the specific deposition conditions and material combinations employed.

3.1.2 Thermal annealing. Thermal annealing has been widely employed to generate isotropic wrinkles in thin film systems, for instance, a metal layer deposited on polystyrene (PS) films supported onto silicon wafers.[142–146] As illustrated in

Open Access Article. Published on 31 March 2026. Downloaded on 4/22/2026 5:53:25 AM.
This article is licensed under a Creative Commons Attribution 3.0 Unported Licence.

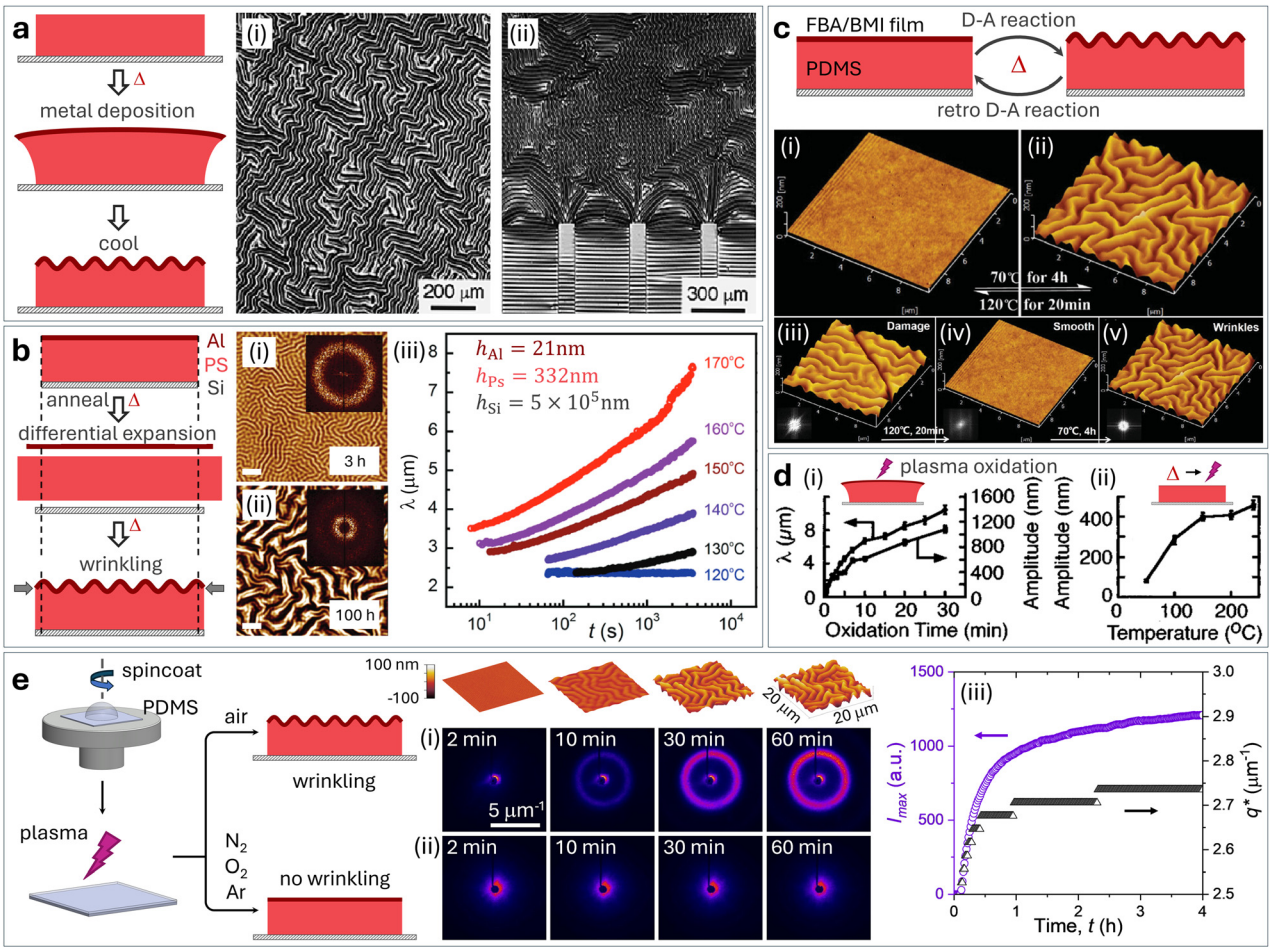

Fig. 6 Temperature-driven approaches for generating isotropic wrinkle patterns. (a) Metal deposition on thermally expanded elastomer: schematic showing metal film deposition on heated PDMS followed by cooling-induced contraction, generating wrinkles. Microscopy images demonstrate (i) isotropic wrinkles and (ii) transition from isotropic to ordered wave patterns in the Au/PDMS system near rectangular edges. Adapted with permission.[64] © 1998, Springer Nature. (b) Thermal annealing of metal/polymer bilayers (*e.g.*, Al/PS/Si), each undergoing different thermal expansion, but due to interfacial constraints, wrinkling occurs. (i) and (ii) Time-resolved AFM topography showing wrinkle formation at 3 h and 100 h (scale bars: 10 μm), and (iii) quantitative wavelength evolution analysis across temperature and time. (i) and (ii) Adapted with permission.[131] © 2005, American Chemical Society. (iii) Adapted with permission.[132] © 2010, American Chemical Society. (c) Reversible wrinkling *via* Diels–Alder (D–A) chemistry: furan-grafted poly(butyl acrylate) (FBA) and bismaleimide (BMI) deposited on PDMS with a (i) flat initial surface, and (ii) wrinkled surface after D–A crosslinking at 70 °C. This process can be reversed through retro D–A reaction at 120 °C. (iii)–(v) Demonstration of self-healing capability: (iii) intentionally damaged wrinkle pattern, (iv) complete erasure of surface features after heating at 120 °C, and (v) successful regeneration of wrinkle patterns upon subsequent heating at 70 °C, as confirmed by FFT analysis (insets). Adapted with permission.[133] © 2016, Wiley-VCH. (d) Plasma oxidation-induced wrinkling, where oxide layer formation occurs on thermally expanded PDMS: (i) wavelength and amplitude of generated wrinkles scale with plasma oxidation time, and (ii) amplitude dependence on substrate preheating temperature. Adapted with permission.[134] © 1999, American Institute of Physics. (e) Spontaneous wrinkling in plasma-oxidized PDMS when exposed to air, whereas no wrinkling occurs when oxidized PDMS is exposed to an inert atmosphere. (i) AFM and SALS diffraction patterns at different time intervals for oxidized surfaces exposed to air, and (ii) absence of diffraction in a N_2 atmosphere. (iii) Temporal evolution of diffraction intensity and wavenumber, corresponding to A and λ, respectively. Adapted under the terms of the CC BY 4.0 license.[135] © 2025 The Authors.

Fig. 6b, when a thin polymer film capped with a metal layer (typically Al) on a Si substrate is heated, the polymer expands more than the metal layer and silicon substrate due to its higher thermal expansion coefficient. Since the layers are bonded together, this differential expansion generates compressive stresses that lead to wrinkling, associated with the viscoelasticity of the polymer. When the temperature exceeds the glass transition temperature (T_g) of the polymer, the layer softens dramatically, increasing its thermal expansion coefficient. If the compressive stress in the metal layer surpasses the threshold needed to overcome the polymer's reduced shear stiffness, the system becomes unstable and the metal film buckles to form wrinkle patterns. Temporal evolution of these patterns has been documented using atomic force microscopy (AFM), revealing progression in wrinkle dimensions over time, as confirmed by FFT patterns shown in the insets (Fig. 6b(i) and (ii)).[131,147] Chan and coworkers[132,146] quantified this temperature dependence, showing how wavelength evolves across different annealing temperatures and timescales (Fig. 6b(iii)).

Open Access Article. Published on 31 March 2026. Downloaded on 4/22/2026 5:53:25 AM. This article is licensed under a Creative Commons Attribution 3.0 Unported Licence.

Various material combinations, beyond Al/PS/Si systems, have been explored.[148–150] Thermoplastic elastomers like polystyrene–polybutadiene–polystyrene (SBS) triblock copolymers can yield stable wave structures that persist after cooling.[149] Systems without metal capping layers have also been developed, including PDMS surfaces treated with UV/ozone and oxygen plasma, where thermal annealing produces wavelength reduction, in contrast to the wavelength increase typically observed in metal-capped systems.[151] Innovative applications have emerged, such as dye-doped polystyrene bilayers capped with higher-T_g materials, which achieve resonant random lasing through thermally-induced surface wrinkling.[152] Pattern characteristics can be tuned through adjusting the annealing temperature and time, polymer molecular weight, and layer thicknesses,[145] enabling tailored surface morphologies for applications ranging from optical devices to mechanical sensors.[132,150,152]

The nature and thermal response of the interface between layers can also play an important role in pattern formation. In standard wrinkling theory, the stiff film is assumed to be perfectly adhered to the compliant substrate, imposing a no-slip boundary condition at the interface.[42,65,66] Under this condition, compressive stresses are transmitted through interfacial shear rather than frictional sliding, meaning the resistance to compression arises from adhesion rather than friction in the classical sense. Evidently, fracture and delamination offer other routes to energy dissipation.[153] In strongly-bonded (*e.g.*, covalent) bilayer systems, interfacial slip is effectively precluded. However, in weakly-bonded or viscoelastic systems, wrinkling response can become time-dependent, and wrinkle patterns may form transiently and subsequently evolve or relax toward planarity as the stored compressive stress dissipates. This is for instance the case for PS/PDMS bilayers, where the viscoelastic stress relaxation is near and above the glass transition temperature of PS,[57,146] or if the film is elastic but the substrate is instead viscoelastic.[105]

3.1.3 Chemical reaction. Surface wrinkling can also be achieved through dynamic chemical reactions that modify material properties in response to thermal stimuli. A notable example exploits the Diels–Alder (D–A) reaction, a thermally reversible cycloaddition between a conjugated diene and an alkene that forms a six-membered ring structure.[154] By incorporating D–A reactive groups into polymer systems, Hou and coworkers[133] developed smart surfaces with controllable topography, generating a bilayer structure by coating PDMS with a reactive layer containing furan-modified poly(butyl acrylate) (FBA) and bismaleimide (BMI) (Fig. 6c). When heated to 70 °C, these components undergo D–A crosslinking, significantly increasing layer rigidity. The substantial difference in mechanical properties between this stiffened top layer and the soft PDMS substrate generates compressive stress upon cooling, resulting in surface wrinkles (Fig. 6c(i) and (ii)). These patterns exhibit excellent stability at room temperature, persisting for over one year without degradation. The wrinkles can be erased by heating to 120 °C, which triggers a retro-D–A reaction that breaks the crosslinks and returns the top layer to its original soft state. This reversibility enables 'self-healing' capabilities, if the wrinkled surface is damaged, and the same thermal cycle can regenerate the original pattern (Fig. 6c(iii)–(v)). Such dynamic control over surface topography through chemical reactions opens possibilities for creating smart materials with switchable properties, offering advantages for applications requiring repeated reconfiguration without material degradation.

3.1.4 Plasma/UVO oxidation. Plasma oxidation and ultraviolet-ozonolysis (UVO) have emerged as facile and widely used treatments to fabricate surface wrinkles on polymeric materials, particularly on PDMS.[96,155,156] Compared to metal deposition approaches, surface oxidation offers advantages of laboratory accessibility and lower processing temperatures, making it particularly attractive for applications involving temperature-sensitive materials or biological systems. When PDMS is exposed to plasma treatment, its surface undergoes chemical modification, forming a thin oxide layer (10 s nm) that resembles porous silica (SiO_2).[116,134,157,158] This ''glassy'' skin exhibits distinct mechanical and chemical properties compared to the bulk polymer. UVO treatment provides an alternative oxidation route, creating a similar glassy silica-like layer through UVO exposure, though typically forming substantially thicker and stepped oxide layers (approximately 1–10 μm) compared to plasma treatment.[96,116,157]

The wavelength and amplitude of plasma and UVO-induced wrinkling can be tuned by controlling plasma exposure time. Bowden *et al.*[134] demonstrated that longer exposure times result in thicker oxide layers and consequently larger wrinkle dimensions (Fig. 6d(i)). Additionally, wrinkles formed on pre-heated samples displayed increased amplitude with higher substrate temperatures (Fig. 6d(ii)). The morphology and characteristics can be further controlled through various processing parameters and material systems.[159–161] The versatility of plasma (and UVO) processing allows precise control over surface topography through multiple parameters: plasma power, gas composition, pressure, exposure time, and substrate thickness, making it a highly tunable approach.[162,163]

Although early reports attributed wrinkling in plasma-oxidized thin PDMS films to thermal cycling,[134] recent work by Ahmad and coworkers[135] revealed an alternative mechanism involving gas sorption. Plasma-oxidized PDMS films placed under an inert atmosphere (N_2/O_2/Ar), develop no wrinkling patterns, whereas oxidized films exposed to air exhibit the characteristic wrinkling behavior (Fig. 6e(i)–(iii)), and the wrinkling amplitude evolves slowly over minutes to days when exposed to different atmospheric conditions. Differential water sorption between bulk PDMS and the oxidized silica-like skin layer was instead found to be responsible for wrinkling, generating in-plane stresses, rationalized in terms of a sorption–swelling–wrinkling mechanism. This process enables applications such as inexpensive optical environmental sensors that respond to changes in atmospheric humidity or temperature.

Beyond PDMS, plasma-induced wrinkling has been demonstrated in other polymer systems, such as polyethylene glycol diacrylate (PEGDA) films.[164] Plasma-based techniques have also

Open Access Article. Published on 31 March 2026. Downloaded on 4/22/2026 5:53:25 AM. This article is licensed under a Creative Commons Attribution 3.0 Unported Licence.

been developed for rapid deposition of thin polymeric films with controlled wrinkle patterns. Gerchman and coworkers[165] employed environmentally-friendly D-limonene precursors in custom plasma setups for one-step fabrication of wrinkled polymer coatings, where pattern formation was attributed to thermal stress arising from differential thermal expansion, and wrinkle dimensions were controlled through deposition time.

3.1.5 Laser irradiation. Laser heating enables precise spatial control over wrinkle formation in multilayer polymer systems through localized thermal delivery. When a CO_2 laser beam interacts with an Al/PS film stack, it creates radially-aligned wrinkles within irradiated spots due to thermal expansion mismatch, while subsequent uniform heating produces isotropic patterns in surrounding areas.[166] Recent advances have expanded this approach using photo-thermal materials, for instance, using carbon nanotube-doped PDMS substrates enable reversible wrinkle formation through near-infrared laser direct writing.[167] The technique has been extended to other systems, including femtosecond laser treatment of shape memory polymers to generate hierarchical patterns.[168] Although less common for isotropic wrinkles, laser-based methods highlight the potential for spatially programmable wrinkling.

3.2 Light-induced mechanisms

Light offers unique advantages for wrinkle fabrication through its ability to remotely trigger photochemical processes with precise spatial and temporal control. Different wavelengths, including ultraviolet (UV), visible, and near-infrared (NIR), can activate distinct mechanisms such as polymerization, crosslinking, degradation, and molecular conformational changes. Wavelength selectivity can also support sophisticated control strategies, from single-step fabrication to reversible pattern manipulation. This section examines how light-activated mechanisms create and modulate isotropic surface wrinkles.

3.2.1 Ultra-violet light. Several photochemical pathways have been developed for wrinkling induced by UV irradiation. One approach exploits self-wrinkling in polymer networks, harnessing gradient-crosslinked structures that form during UV light exposure in the presence of oxygen.[169,170] Oxygen inhibits polymerization at the surface while allowing crosslinking in the bulk, resulting in a modulus gradient. The uncured liquid layer at the surface can subsequently swell the underlying gradient-crosslinked film, spontaneously generating wrinkle patterns within a single fabrication step (Fig. 7a).

This oxygen-mediated process can be precisely controlled using PDMS films of varying thickness as an oxygen reservoir (Fig. 7a(ii)).[169,176,177] Greater PDMS thickness provides more available oxygen, enhancing polymerization inhibition and producing thicker uncured liquid layers, which ultimately increases wrinkling amplitude. The resulting labyrinthine morphology (Fig. 7a(i)) can be tailored through multiple parameters: choice of UV-crosslinkable polymer, photoinitiator concentration, UV exposure conditions, and film thickness.[178–181] This tunability has led to applications such as self-matting coatings (*i.e.*, which promote light scattering) whose 'roughness' can be optimized for specific optical properties.[179,180]

Beyond oxygen-mediated crosslinking, UV light can drive wrinkle formation through photoresponsive chemistries like anthracene dimerization,[171,175,182–184] *e.g.* by increasing crosslinking in polymers containing anthracene groups by photodimerization, and thus also mechanical modulus (Fig. 7b). This localized stiffening triggers wrinkle formation with dimensions that scale with UV exposure time (Fig. 7b(i) and (iii)) and, moreover, the process is reversible to exposure to 254 nm UV or heat, which is able to cleave the dimers and erase the patterns (Fig. 7b(ii)). Additional UV-based mechanisms include photodegradation through chain scission reactions, photoinitiated polymerization of azobenzene-containing compounds, and hybrid approaches combining UV polymerization with sol–gel chemistry.[185–188] This diverse range of UV-induced processes provides precise spatial and temporal control over surface patterns, employing photomasks or direct writing.

3.2.2 Visible light. Visible light control of surface wrinkling exploits photoactive molecules, particularly azobenzene compounds that undergo conformational changes upon illumination. Poly(disperse orange 3) (PDO_3), an amorphous azobenzene polymer with epoxy functionalization, offers an effective photoresponse with absorption spanning 400–600 nm and peak absorption at 478 nm.[172,173] Wang and coworkers[172] demonstrated a bilayer system combining PDO_3 and polystyrene as the stiff film on PDMS substrates. Selective illumination with 450 nm light using a photomask generates labyrinthine patterns in the exposed regions (Fig. 7c). Pattern formation arises from photothermal effects that generate isotropic stresses as the surface temperature increases during illumination. Wrinkle characteristics can be systematically controlled by modifying film thickness and the mechanical properties of the PDO_3 layer. Alternative visible light approaches include systems utilizing styryl-anthracene carboxylic acid (SACA), which undergoes photocycloaddition at 450 nm, leading to enhanced modulus through crosslinking in PS-P_4 VP-PBA/SACA bilayer systems.[189]

Furthermore, substantial efforts have focused on creating rewritable surfaces where wrinkles, initially formed through various stimuli (thermal, UV, or Diels–Alder reactions), can be selectively erased using visible light.[173,190–193] This concept was demonstrated in systems including PDO_3 films on PDMS, where visible light triggers reversible photoisomerization of azobenzene groups (Fig. 7d(i)). The combination of stress release and light-induced material softening results in a gradual reduction of wrinkling amplitude while preserving wavelength (Fig. 7d(ii) and (iii)). This approach has been implemented in increasingly sophisticated systems, including laminated multilayers (PDMS/SiO_x/PDO_3, PDMS/PS/PDO_3),[191] azobenzene-containing epoxy oligomers,[190] azobenzene-containing polyimide,[192] and crosslinked networks combining furan-containing polymers with maleimide-substituted azobenzene.[193] When combined with spatially moduluated illumination, these systems demonstrate potential applications in information encryption and security features.[193,194]

3.2.3 Near-infrared light. Near-infrared (NIR) light has also been employed to manipulating surface wrinkles through

 This journal is © The Royal Society of Chemistry 2026

Open Access Article. Published on 31 March 2026. Downloaded on 4/22/2026 5:53:25 AM.
This article is licensed under a Creative Commons Attribution 3.0 Unported Licence.

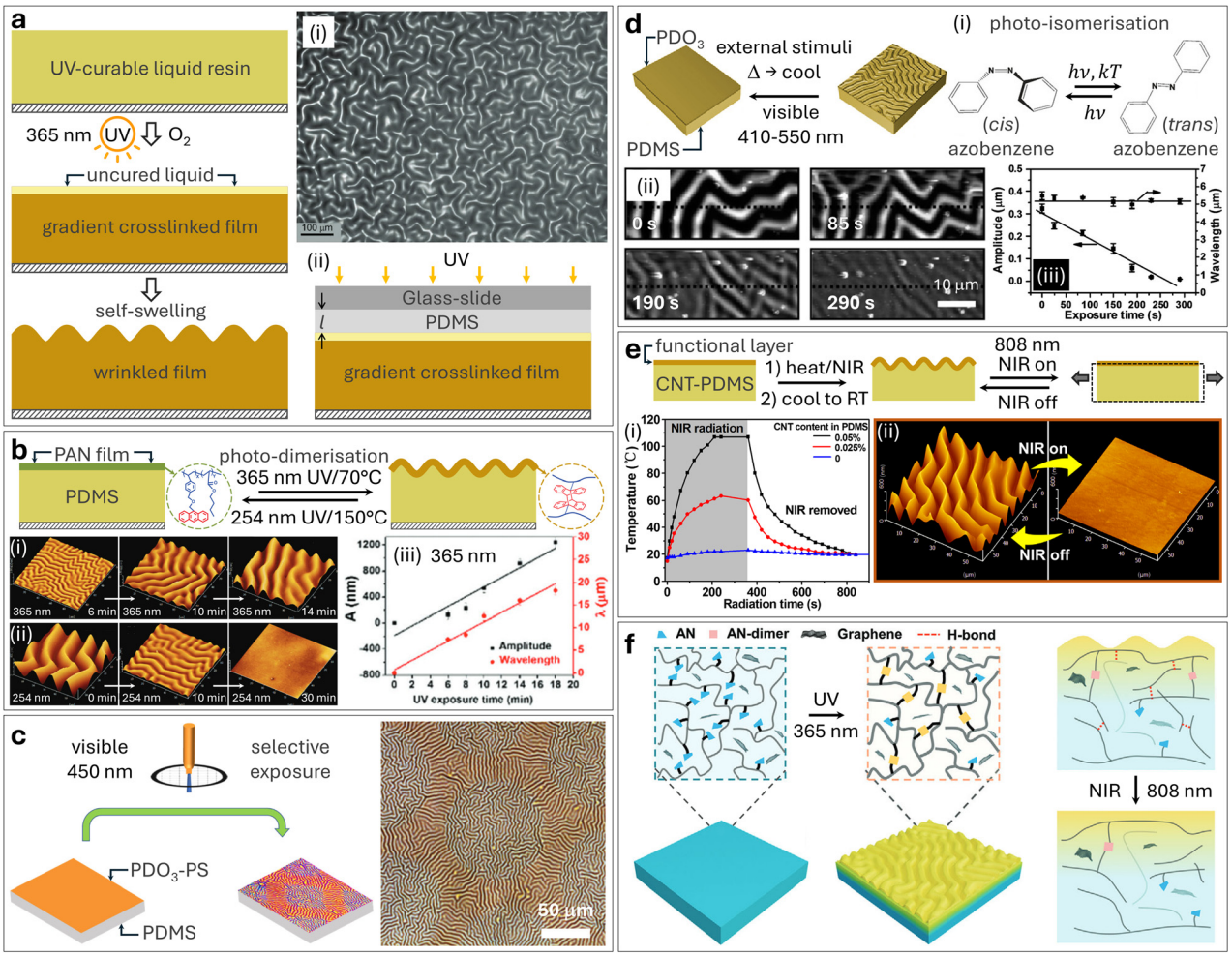

Fig. 7 Light-induced isotropic wrinkling mechanisms across different wavelength regimes. (a) UV-triggered wrinkling in photocurable resins: formation mechanism *via* gradient crosslinking under oxygen exposure and self-swelling of the uncured liquid. (i) Characteristic labyrinthine morphology and (ii) porous PDMS membrane of thickness *l* as an oxygen reservoir for controlled wrinkle formation. Adapted with permission.[169] © 2011, Wiley-VCH (b) Reversible UV-responsive wrinkling using anthracene photochemistry: (i) wrinkle development during 365 nm exposure, (ii) pattern erasure under 254 nm irradiation, and (iii) quantitative evolution of amplitude and wavelength parameters during 365 nm exposure. Adapted with permission.[171] © 2017, Royal Society of Chemistry. (c) Visible light patterning: selective 450 nm laser exposure through copper grid mask creating localized wrinkle formation in PDO_3–PS/PDMS bilayer system. Adapted under the terms of the CC BY 4.0 license.[172] © 2022 The Authors. (d) Visible light-controlled wrinkle erasure *via* azobenzene photoisomerization: (i) molecular switching mechanism, (ii) temporal wrinkle disappearance sequence, and (iii) quantitative amplitude decay with preserved wavelength characteristics. Adapted with permission.[173] © 2016, Wiley-VCH. (e) NIR-responsive wrinkling in CNT-PDMS composites: (i) temperature profiles during NIR on/off cycling for different CNT concentrations and (ii) reversible wrinkle modulation under 808 nm irradiation. Adapted with permission.[174] © 2018, American Association for the Advancement of Science. (f) Dual-wavelength responsive system: UV-induced anthracene dimerization for wrinkle formation and NIR-triggered graphene photothermal heating for pattern erasure. Adapted with permission.[175] © 2024, Wiley-VCH.

photothermal effects. Li and coworkers[174] demonstrated this concept using bilayer systems comprising functional polymers on carbon nanotube-containing PDMS (CNT-PDMS). Initial wrinkle formation occurs upon heating and cooling due to mismatched thermal expansion between film and substrate; when exposed to NIR (808 nm) light, CNTs exhibit efficient photon-to-thermal energy conversion, causing local heating and thus thermal expansion of the substrate. This expansion decreases compressive strain, resulting in pattern erasure (Fig. 7e), driven by a decrease in wrinkling amplitude at largely constant wavelength. The temperature profiles during NIR on/off cycling (Fig. 7e(i)) reveal that wrinkle recovery upon removing NIR exposure occurs more slowly than erasure, attributed to slower heat dissipation compared to rapid photon-to-thermal conversion by CNTs. The system shows excellent reversibility, maintaining consistent wrinkle patterns during over 1000 NIR on/off cycles (Fig. 7e(ii)). While initial studies used a random fluorinated copolymer (PSF) as the functional skin layer, the approach has since been demonstrated with various materials, including PMMA and gelatin.[174]

By combining materials responsive to different wavelengths, sophisticated systems capable of dynamic wrinkle manipulation across the electromagnetic spectrum have been developed. Zhou and coworkers[195] created a dual-responsive system using

Open Access Article. Published on 31 March 2026. Downloaded on 4/22/2026 5:53:25 AM. This article is licensed under a Creative Commons Attribution 3.0 Unported Licence.

anthracene-containing polymer (PAN-BA) on CNT-PDMS, where anthracene groups respond to UV light, while CNTs absorb NIR radiation. Similar approaches have been explored incorporating components to induce structural color and camouflaging capabilities under visible light illumination.[195,196] Yuan *et al.*[175] further advanced this concept by developing anthracene-containing photosensitive polyurethane films with embedded graphene, where UV light triggers anthracene photodimerization for wrinkle formation while NIR absorption by graphene enables thermal control for pattern erasure (Fig. 7f). These multi-wavelength responsive systems demonstrate the potential for creating sophisticated, dynamically tunable surface structures for applications in adaptive optics, smart surfaces, and information storage.

3.3 Solvent- & vapor-induced

Solvent- and vapor-induced wrinkling harnesses strain from chemical interactions with the skin or substrate materials to generate surface patterns, in a simple and reversible manner, as patterns can often be created and erased through controlled environmental exposure. The method is compatible with diverse material systems, from bilayers created through plasma or UVO treatment, metal deposition, and polymer film coating to modulus-gradient films achieved *via* UV curing or chemical reactions. Various solvents, including water, organic liquids, and vapors, can induce the necessary compressive stresses for pattern formation through either swelling or drying mechanisms.

3.3.1 Liquid swelling. The seminal work by Tanaka and coworkers[197] in 1987 demonstrated that crosslinked polymer networks undergo volume phase transitions when immersed in liquids, leading to the spontaneous formation of regular surface patterns. Using acrylamide gels as a model system, pattern formation was shown to initiate when a thin surface layer swells under mechanical constraint; while the outer surface can freely expand, the inner surface remains fixed to the bulk gel (Fig. 8a). When the osmotic pressure exceeds a critical threshold, the outer surface buckles to form structures with wavelengths proportional to the swollen layer thickness.

Building on this understanding, hydrogels with crosslinking gradients have been employed for controlled pattern formation, for instance, using poly(2-hydroxyethyl methacrylate) (PHEMA) networks.[202] Employing UV curing in the presence of oxygen to generate films with a softer surface layer that gradually stiffens with depth (Fig. 8b), differential swelling upon contact with water can lead to stable wrinkle patterns that persist in both swollen and dry states. Furthermore, pattern morphology can be finely controlled through crosslinker concentration, film thickness, UV exposure conditions, substrate properties, and choice of swelling solvent.[202–207]

Beyond hydrogel systems, solvent-induced wrinkling has been demonstrated with various polymers. Crosby and coworkers[198,199,208] explored two distinct swelling mechanisms of films adhered to ultraviolet-ozone (UVO) treated polydimethylsiloxane (PDMS). In one approach, the swelling agent (*n*-butyl acrylate) primarily penetrated and expanded the bulk PDMS relative to the stiff oxidized surface layer (Fig. 8c). In the second approach, UVO-treated PDMS was exposed to ethanol, causing preferentially swelling of the oxidized skin layer relative to the bulk PDMS (Fig. 8d). The mismatch in swelling behavior, coupled with geometric constraints, led to wrinkle pattern formation that could be controlled through oxidation conditions and solvent choice. Patterns formed by *n*-butyl acrylate could be further permanently locked through photopolymerization, while ethanol-induced patterns were reversible upon solvent evaporation.[199,209]

The morphology of solvent-induced wrinkles changed systematically as a function of UVO oxidation time, t_{UVO} (Fig. 8c and e), resulting in a library of surface patterns including dimple, random line, and labyrinthine structures (Fig. 8e(iii)–(v)). With increasing t_{UVO}, both wavelength and amplitude increased due to greater stiffness and larger thickness of the oxidized layer (Fig. 8e(ii)). The reversible nature of these patterns upon wetting and drying enables applications such as tunable optical devices, reconfigurable channels, and dynamic assembly platforms for nanoparticles.[199]

Controlled wrinkling has also been achieved in polymer brush systems through postpolymerization modifications. By selectively crosslinking the outer region of polymer brushes under poor solvent conditions and then exposing them to good solvents, wrinkled morphologies can arise from a mismatch between lateral and perpendicular swelling directions within the brush architecture.[210,211]

3.3.2 Vapor swelling. While liquid solvent-induced wrinkling relies on direct contact between the solvent and material system, vapor-phase solvents can also trigger surface instabilities through controlled diffusion and selective swelling. This approach was demonstrated by Chung and coworkers,[117] who investigated the wrinkling of UVO-treated polystyrene films exposed to toluene vapor. The preferential swelling of unmodified PS regions by vapor sorption generated osmotic stresses that could trigger wrinkling instabilities. When the compressive stress, induced from differential swelling, exceeded a critical threshold, surface wrinkles formed with pattern morphology exhibiting clear dependence on UVO exposure time. Varying UVO exposure (from 2 to 40 min) produced diverse morphologies, including flower-like, radial spokes, concentric targets, labyrinthine networks, and isolated dots (Fig. 8f). Once formed, these patterns remained stable for extended periods following removal from the vapor environment, indicating that the polymer undergoes flow during pattern development and subsequently becomes kinetically arrested in the wrinkled configuration as the solvent evaporates and the material returns to its glassy state. The 2D FFT analysis shown in the insets reveals the characteristic spatial organization of each pattern type. Similarly to liquid-induced swelling, ethanol vapor can preferentially swell the oxidized layer in UVO-treated PDMS compared to the bulk material, with pattern evolution controlled by both vapor pressure and oxidation extent.[212,213]

An important mechanistic insight emerged from recent work on plasma-oxidized PDMS. As discussed in the thermal-induced Section 3.1.4 on plasma oxidation, Ahmad and

 This journal is © The Royal Society of Chemistry 2026

Open Access Article. Published on 31 March 2026. Downloaded on 4/22/2026 5:53:25 AM.
This article is licensed under a Creative Commons Attribution 3.0 Unported Licence.

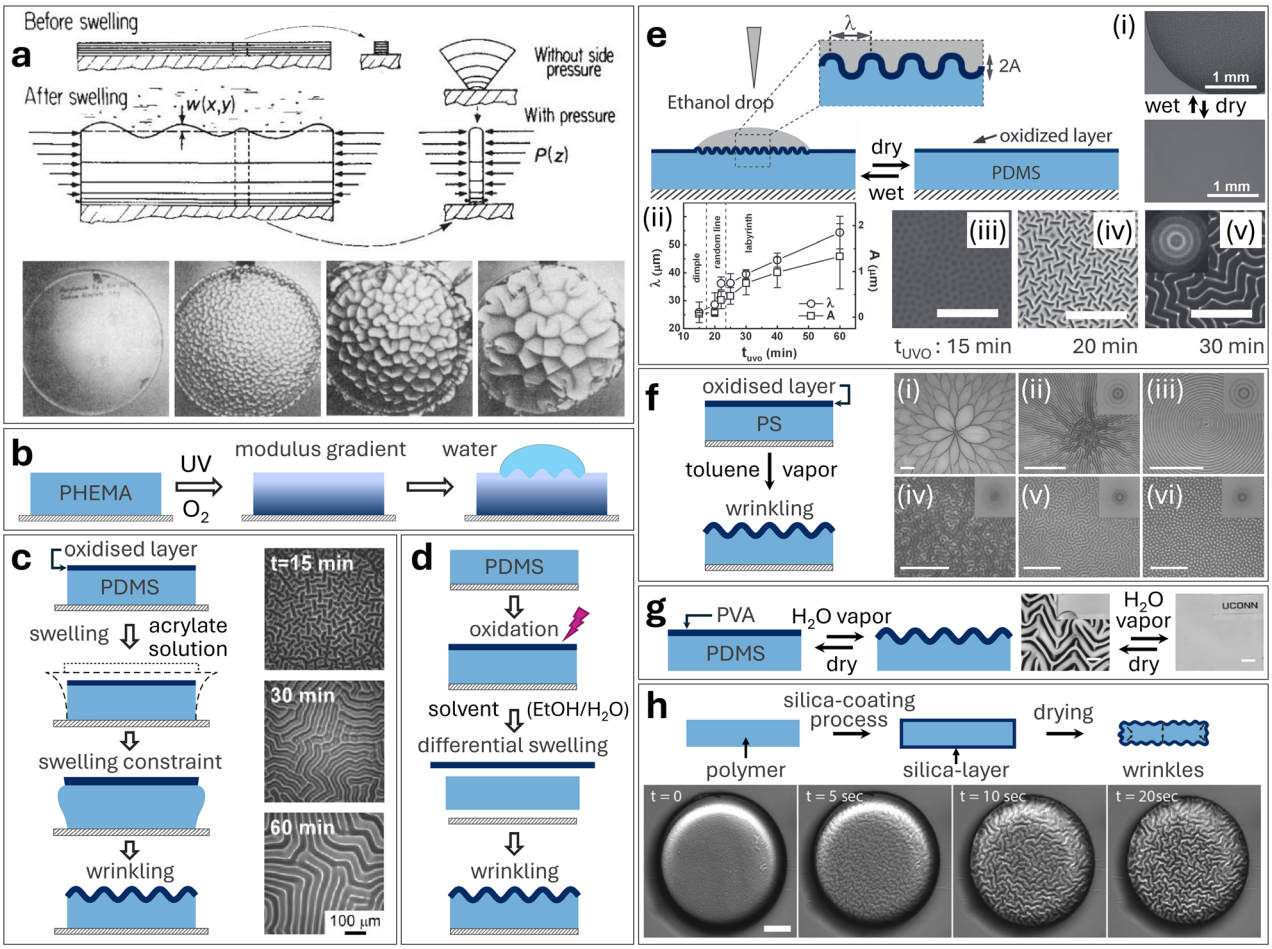

Fig. 8 Solvent-induced isotropic wrinkling through swelling and drying mechanisms. (a) Swelling-driven pattern formation in hydrogel systems: schematic depicting constrained film behavior before and after swelling, with time-series images showing progressive pattern evolution in an ionized acrylamide gel. Adapted with permission.[197] © 1987, Springer Nature. (b) Gradient modulus approach: UV-treated PHEMA film in the presence of O_2 developing surface patterns upon water exposure. (c) Wrinkling from preferential swelling of bulk elastomer upon contact with liquid solvent: acrylate-induced expansion of PDMS relative to the silicate layer creates interfacial strain mismatch, leading to compressive buckling; optical images show different pattern formation with varied UVO oxidation times. Adapted with permission.[198] © 2006, Royal Society of Chemistry. (d) Alternative swelling mechanism for oxidized elastomers exposed to solvent ($EtOH/H_2O$): the oxidized layer exhibits greater solvent uptake than the underlying elastomer, generating interfacial constraint and compression. (e) Reversible wrinkling *via* liquid solvent exposure: (i) ethanol droplet induces transient patterns on UVO-treated PDMS that disappear upon drying, (ii) wavelength and amplitude dependence on oxidation time, and (iii)–(v) morphological transitions from dimples to random lines to labyrinthine patterns with increasing oxidation duration (scale bars: 200 μm). Adapted with permission.[199] © 2011, Wiley-VCH. (f) Vapor-phase solvent exposure: toluene-induced patterns in UVO-treated polystyrene (PS) films showing morphological variations with exposure time ((i)–(vi): 2–40 minutes), with 2D FFT analysis (insets). Scale bars: 30 μm. Adapted with permission.[117] © 2009, Wiley-VCH. (g) Humidity-responsive wrinkling: reversible pattern formation in PVA–PDMS bilayers upon water vapor exposure and removal, demonstrating cyclic stability (scale bars: 100 μm). Adapted with permission.[200] © 2017, Wiley-VCH. (h) Drying-induced wrinkling: temporal evolution of surface patterns during solvent evaporation from silica-coated polymer particles (scale bar: 25 μm).[201] © 2015, Wiley-VCH.

coworkers[135] revealed that wrinkling in plasma-oxidized thin PDMS films occurs not through thermal cycling but *via* differential water sorption between bulk PDMS and the oxidized silica-like skin layer. The dynamic, reversible wrinkling response correlates directly with relative humidity, demonstrating proof-of-concept optical-based environmental, temperature, and humidity sensors.

Beyond modified single-layer systems, vapor-induced wrinkling has been demonstrated in various bilayer configurations. Polyvinyl alcohol/polyethyl acrylate bilayers develop surface patterns through absorption-induced compressive stresses when exposed to moisture.[214] Metal-capped polymer films exhibit progressive pattern evolution as the underlying polymer absorbs organic vapors over time.[215] Uniformly crosslinked PVA films on PDMS substrates exhibit reversible wrinkle formation through moisture absorption and drying cycles (Fig. 8g).[200] By manipulating the crosslinking properties of the PVA film, different wrinkling behaviors can be achieved, enabling dynamic control over surface topography. Alternative approaches have focused on gelatin films containing PS particles on PDMS substrates, where controlling environmental humidity and exploiting regional differences in modulus enable dynamic tuning of

Open Access Article. Published on 31 March 2026. Downloaded on 4/22/2026 5:53:25 AM. This article is licensed under a Creative Commons Attribution 3.0 Unported Licence.

complex surface patterns, making them promising candidates for smart optical devices.[216]

3.3.3 Drying. The reverse process of deswelling or drying in bilayer systems can also generate the necessary strain mismatch for controlled wrinkling. In one approach, polymeric microparticles were synthesized by photopolymerization of ethoxylated trimethylolpropane triacrylate (ETPTA) and 3-(trimethoxysilyl)propyl acrylate (TMSPA) mixtures, then coated with a stiff silica film through tetraethyl orthosilicate (TEOS) injection.[201] Subsequent drying created compressive strain through differential shrinkage of the particle core relative to its rigid silica shell, generating distinctive surface patterns that evolved during evaporation (Fig. 8h). The wavelength of these patterns could be tuned by varying coating time and UV exposure, enabling applications in anti-counterfeiting technologies described in later sections.

Hydrogel systems can also support drying-induced wrinkling, and for instance HEMA-based films form wrinkled surfaces through direct deposition and drying, tunable by the molecular weight of the crosslinking agent.[217,218] Moisture-responsive wrinkled films have been developed through bilayer systems combining cellulose nanofibrils with polyvinyl alcohol–glycerol layers,[219] where differential swelling and modulus mismatch between layers creates reversible wrinkled structures that respond to ambient humidity, enabling passive optical switching for smart building applications.

Polyion complexation offers another route to wrikling,[220] which has been demonstrated with chitosan films immersed in alginate solutions that form a wrinkled skin layer when drying. The stability of these patterns in aqueous environments was achieved through thermal crosslinking of the polyion complex skin layer, enabling their use in wet conditions. Evaporation during spin coating of elastomeric films provides another approach for creating irreproducible wrinkling patterns in styrene–ethylene–butylene–styrene (SEBS) triblock copolymers.[221] The rapid solvent removal provides control over the solvent retention time on the polymer surface and when toluene is applied to UVO-treated SEBS films and rapidly removed *via* spinning, the crosslinked surface undergoes localized swelling followed by omnidirectional compression during evaporation, generating wrinkling patterns with wavelengths of hundreds of micrometers. These patterns exhibit high randomness and irreproducibility, characteristics that have been exploited to create identifiable artificial finger pad electronics that mimic human fingerprint features for applications in soft robotics, authentication systems, and prosthetic devices.

3.4 Mechanically-induced mechanisms

The fabrication methods discussed thus far generate wrinkles through strain fields that are inherently isotropic in nature, without a preferred directional bias. However, labyrinthine patterns can also form through careful and controlled application of biaxial, multi-axial, or non-planar strains. The mechanical approach typically operates in conjunction with other techniques such as metal deposition, plasma oxidation, or polymer coating to create the bilayer structure. While these surface modification methods establish the necessary modulus mismatch, the compressive stress driving wrinkle formation is introduced mechanically through substrate deformation.

This strain-based approach is most commonly employed to create uniaxial wrinkle patterns through unidirectional stretching or compression.[39,67] By manipulating strain directions and magnitudes, the formation of varied anisotropic patterns such as checkerboard or herringbone structures have been demonstrated. This section examines how biaxial, multi-axial, and non-planar strain configurations can be exploited to produce isotropic wrinkle morphologies, with particular attention to the impact of strain release on the final pattern characteristics.

3.4.1 Bi-axial strain. The controlled formation of surface patterns through biaxial strain has been investigated using different surface modification approaches. Lin and Yang[94] investigated plasma-oxidized PDMS, showing that various wrinkling morphologies could be achieved by controlling the release sequence of a prestrained bilayer system. Simultaneous release of equal strain in both planar directions resulted in labyrinthine patterns (corresponding to the energy minimization condition[94]) (Fig. 9a(ii)), while sequential strain release produced ordered herringbone patterns (Fig. 9a(i)). Pattern formation occurred immediately upon reaching the critical buckling threshold, with wrinkle amplitude increasing upon further strain release.

Alternative surface modification techniques include initiated chemical vapor deposition (iCVD), a solvent-free technique for depositing thin polymer films (discussed in Section 3.5), to create the rigid top layer on prestrained PDMS (Fig. 9b).[222] Consistent with the observations employing plasma oxidation, simultaneous strain release produced labyrinthine patterns while sequential release yielded herringbone morphologies. Importantly, pattern reversibility varied significantly: herringbone patterns could be cycled repeatedly through stretching and release, whereas labyrinthine patterns showed irreversible deformation due to localized regions of high strain that created permanent topological defects.[225] More recently, UVO treatment of prestrained elastomers like Ecoflex has enabled the fabrication of crack-free wrinkled surfaces capable of withstanding much larger strains, expanding the range of achievable pattern dimensions and potential applications.[226]

3.4.2 Multi-axial strain. Strain engineering through multi-axial mechanical deformation further widens the spatial control over wrinkling patterns. Wang and coworkers[223] utilized a strain stage with three axes arranged at 120° intervals (Fig. 9c(i)). When subjected to equal strain application along all three axes, this configuration creates position-dependent stress anisotropy across triangular samples (Fig. 9c(ii)). The resulting multi-mode wrinkle patterns exhibit labyrinthine morphology in the central region experiencing near-isotropic stress, while other regions of the sample display anisotropic patterns: aligned stripes radiating from corners toward the center, and ripples along the edges (Fig. 9c(iii) and (iv)). The versatility of this approach has been demonstrated across different surface modification techniques, including physical vapor deposition of metal films (tantalum on PDMS, Fig. 9c(iii)),

 This journal is © The Royal Society of Chemistry 2026

Open Access Article. Published on 31 March 2026. Downloaded on 4/22/2026 5:53:25 AM.
This article is licensed under a Creative Commons Attribution 3.0 Unported Licence.

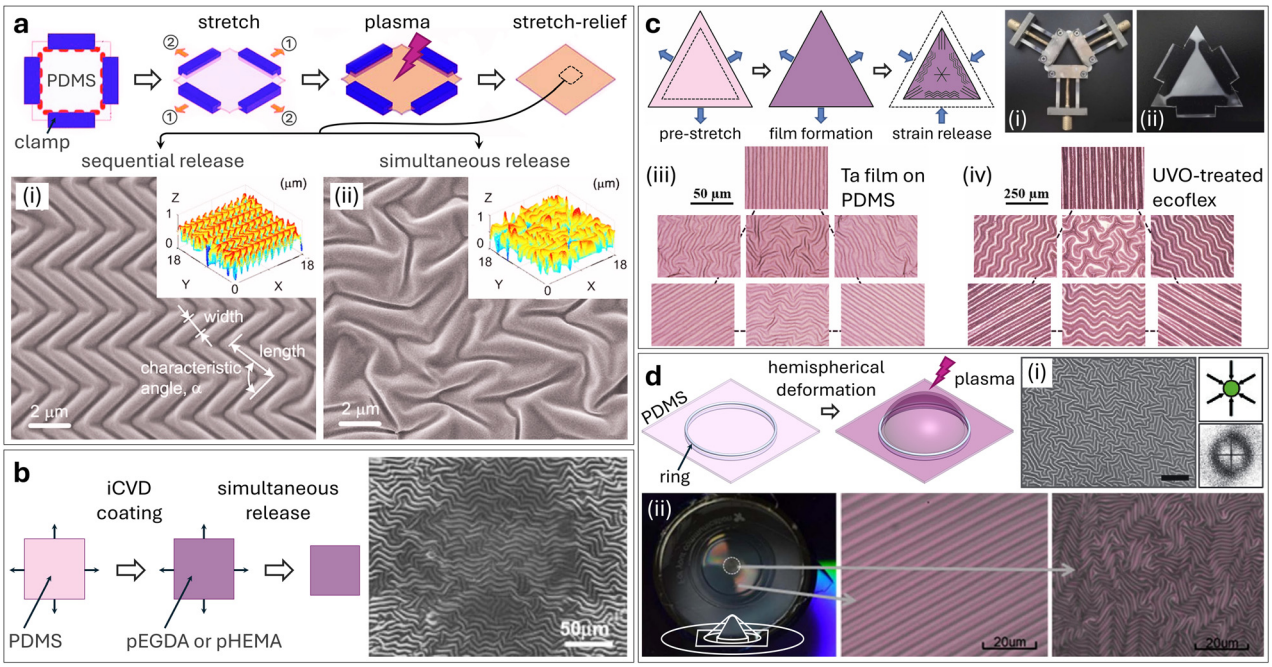

Fig. 9 Mechanically-induced isotropic wrinkling through controlled bi-axial/multi-axial/non-planar strain fields. (a) Biaxial strain approach: fabrication schematic showing clamped PDMS stretched biaxially, plasma-treated, and released to generate wrinkles. SEM images with AFM topography (insets) reveal (i) ordered herringbone morphology from sequential strain release and (ii) disordered labyrinthine patterns from simultaneous release. Adapted with permission.[94] © 2007, American Institute of Physics. (b) Chemical vapor deposition on prestrained substrates: process schematic for iCVD coating of p(EGDA) or p(HEMA) onto stretched PDMS, with SEM showing disordered wrinkle formation after simultaneous release of 10% equibiaxial strain in a 100 nm p(EGDA)/PDMS system. Adapted with permission.[222] © 2012, Wiley-VCH. (c) Three-axial strain engineering for spatial pattern control: fabrication sequence from substrate prestretch through rigid layer formation to controlled strain release, with (i) a tri-axial stretching device, (ii) triangular PDMS specimen after modification and release, and location-dependent morphologies in (iii) tantalum-coated PDMS and (iv) UVO-treated Ecoflex showing transitions from parallel stripes at the edges to labyrinthine structures at the center. Adapted with permission.[223] © 2024, Elsevier. (d) Non-planar strain fields: (i) hemispherical deformation of ring-constrained PDMS, followed by plasma oxidation, generates labyrinthine patterns (optical microscopy with FFT analysis). Scale bar: 20 μm. Adapted with permission.[96] © 2008, Royal Society of Chemistry. (ii) Mechanical deformation of the PDMS film on a CD using a semi-spheroidal indenter and subjected to metal deposition (Au on PDMS), showing concentric wrinkle formation in outer regions and isotropic wrinkles at the center. Adapted under the terms of the CC BY license.[224] © 2013 The Authors.

surface oxidation through UVO treatment of Ecoflex elastomers (Fig. 9c(iv)), and solution-processed graphene oxide coatings. An alternative strategy employs flame oxidation, a simple yet effective method using conventional burners to modify PDMS surfaces, combined with various strain configurations, including sequential and simultaneous biaxial strains, as well as strains acting in three and four directions.[93]

3.4.3 Non-planar strain. Non-planar deformation of elastomeric films has proven effective for generating isotropic wrinkles. Chiche and coworkers[96] achieved isotropic wrinkle patterns by plasma oxidation of thin PDMS membranes (500 μm) molded into hemispherical geometries, by clamping PDMS membranes between rigid rings, then stretched outward into dome surfaces (Fig. 9d(i)). In this deformed state, the films were exposed to plasma oxidation to create a stiff 'glassy' layer, yielding labyrinthine wrinkle patterns upon strain release and returning the film to its flat configuration, as shown by optical microscopy and FFT analysis (Fig. 9d(i)). Similar morphologies were observed when PDMS films under non-planar deformation were subjected to UVO treatment.[227]

An alternative non-planar approach utilized a gold-coated PDMS film deformed using a semi-spheroidal indenter mounted on a compact disc (CD) support (Fig. 9d(ii)).[224] The film was stretched up to 40% while minimizing azimuthal strain through careful indenter design and lubrication, yielding concentric wrinkling rings in the outer regions, with a distinct transition to labyrinthine patterns in areas experiencing isotropic strain near the indenter contact point (Fig. 9d(ii)). Flame oxidation of bent PDMS films, where opposing tensile and compressive strains on convex and concave surfaces were also shown to yield labyrinthine patterns (on concave surfaces).[93]

3.5 Chemically-induced mechanisms

Various chemical modifications, including vapor deposition, ion beam irradiation, and pH-modulated treatments, have been demonstrated in the controlled formation of isotropic wrinkling patterns by creating compressive stress through localized modulation of material composition and mechanical properties at the surface.

3.5.1 Vapor deposition. Polymer films fabricated by initiated chemical vapor deposition (iCVD) can wrinkle due to the deposition process itself, even in the absence of external mechanical strain.[222,225] The iCVD process follows conventional radical polymerization mechanisms where vaporized

Open Access Article. Published on 31 March 2026. Downloaded on 4/22/2026 5:53:25 AM.
This article is licensed under a Creative Commons Attribution 3.0 Unported Licence.

initiator molecules (typically peroxides) are thermally decomposed into radicals using heated filaments, while monomers adsorb onto a cooler substrate surface (Fig. 10a).[228,229] The radicals then react with adsorbed monomers, leading to polymer chain growth that terminates upon encountering another radical. This solvent-free process operates under mild vacuum conditions and low substrate temperatures, yielding conformal coating of polymer films even on delicate or three-dimensional substrates.

Spontaneous wrinkling during iCVD has been demonstrated across various polymer systems. Deposition of fluoropolymer poly(perfluorodecyl acrylate) (pPFDA) on elastomeric substrates generates wrinkles whose dimensions can be controlled by coating thickness.[228,235] In pharmaceutical applications, deposition of poly(2-hydroxyethyl methacrylate) (pHEMA) on clotrimazole drugs showed that wrinkle formation depends critically on the thickness and crystallinity of the drug layer, with patterns emerging only above a threshold thickness (Fig. 10a).[230] Similarly, thermoresponsive poly(*N*-vinylcaprolactam) films deposited on methacrylic acid copolymer (Eudragit) layers exhibited tunable wrinkle morphologies based on film thickness and crosslinking density.[236] In these systems, wrinkling stems from compressive stresses that develop inherently during film growth rather than from external stimuli. Alternative chemical vapor approaches include radio frequency plasma-assisted chemical vapor deposition for thin diamond-

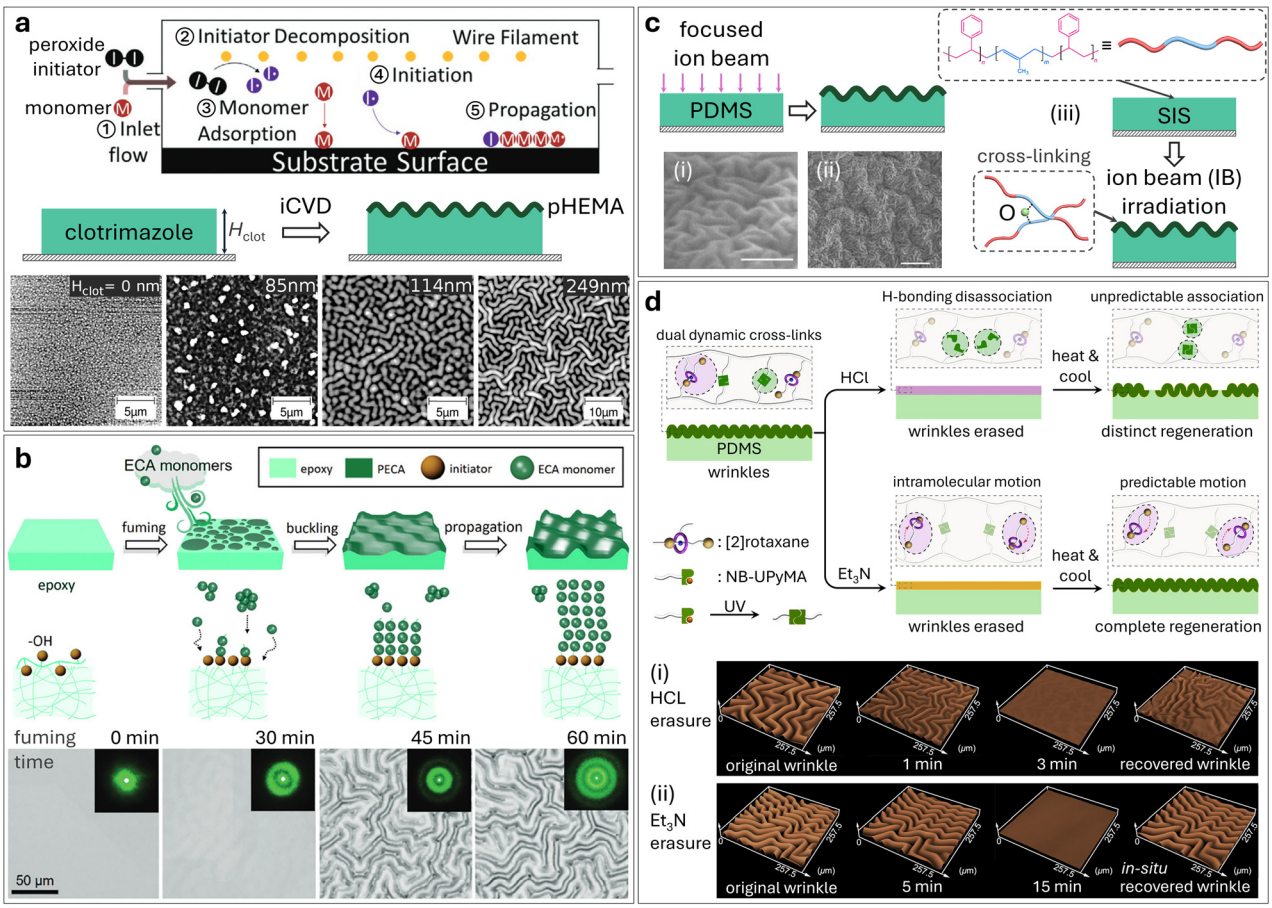

Fig. 10 Chemically-induced isotropic wrinkling through vapor deposition, ion irradiation, and pH modulation. (a) Initiated chemical vapor deposition (iCVD): process schematic showing (1) gas introduction, (2) initiator decomposition, (3) monomer adsorption, (4) initiation, and (5) surface polymerization leading to wrinkle formation. Adapted with permission.[228] © 2022, Wiley-VCH. AFM images demonstrate morphological evolution from no wrinkles (H_{clot} = 0, 85 nm) to increasingly wrinkled surfaces with clotrimazole thickness (tH_{clot} = 114, 249 nm) beneath pHEMA films (h = 206 nm). Adapted under the terms of the CC BY-NC license.[230] © 2016 The Authors. (b) Ethyl cyanoacrylate (ECA) fuming: schematic depicting wrinkle development through interfacial polymerization on epoxy substrates, from initial fuming through buckling to pattern propagation, with molecular-level organization shown below. Time-lapse optical microscopy (0–60 min) reveals progressive pattern formation with laser scattering analysis (insets). Adapted with permission.[231] © 2024, Wiley-VCH. (c) Focused ion beam irradiation: schematic showing ion beam exposure on PDMS generating (i) labyrinthine (scale bar: 400 nm) and (ii) hierarchical wrinkle (scale bar: 5 μm) patterns, by varying the ion-beam acceleration voltage and fluence. Adapted with permission.[232] © 2007, Elsevier. (iii) Crosslinking mechanism in ion-irradiated styrene-*b*-isoprene-*b*-styrene (SIS) with an illustration of the molecular structure. Adapted with permission.[233] © 2020, American Chemical Society. (d) pH-responsive dynamic wrinkling in a dual crosslinked mechanically interlocked network (MIN)/PDMS bilayer containing [2]rotaxane and nitrobenzyl-caged ureidopyrimidinone (NB-UPy) units. 3D confocal microscopy showing reversible wrinkle modulation *via* (i) acid treatment followed by heating (distinct regeneration) and (ii) base treatment followed by heating (complete regeneration). Adapted under the terms of the CC BY 4.0 license.[234] © 2024 The Authors.

Open Access Article. Published on 31 March 2026. Downloaded on 4/22/2026 5:53:25 AM. This article is licensed under a Creative Commons Attribution 3.0 Unported Licence.

like carbon films at room temperature, and pulsed plasma polymerization of maleic anhydride with cellulose nanowhiskers.[237,238]

Atomic layer deposition (ALD) offers a distinct route for generating wrinkled surfaces through controlled vapor-phase modification of polymeric substrates.[239] This technique employs alternating exposure to gaseous precursors in a cyclic process, enabling precise deposition of metal oxide layers (such as Al_2O_3, TiO_2, and ZnO) that can form wrinkled and creased patterns on polymer surfaces.[240,241] The resulting morphologies arise from differential growth mechanisms: some oxides deposit on the polymer surface while others infiltrate into the substrate volume through vapor phase infiltration, with wrinkle characteristics tunable through the number of deposition cycles and choice of oxide material.[241]

An innovative approach to chemically induced wrinkling utilizes interfacial fuming, inspired by the forensic technique of superglue fuming for fingerprint visualization. In forensics, this technique relies on ethyl cyanoacrylate (ECA) vapor polymerizing upon contact with electronegative components present in fingerprint residues (primarily amino acids and proteins in sweat), forming visible white deposits along ridge patterns.[242] Building on this principle, Chen and coworkers[231] developed a surface patterning strategy that exploits the ability of ECA vapors to polymerize upon contact with surfaces containing electronegative functional groups, such as epoxies (containing hydroxyl and carbonyl groups), which undergo interfacial polymerization to form poly(ethyl cyanoacrylate) (PECA). The penetration of monomers causes initial substrate swelling, followed by volumetric shrinkage during polymerization, generating compressive stresses that induce wrinkle formation (Fig. 10b). Wrinkle characteristics can be tuned through reaction time and temperature, which control PECA layer thickness. This ambient pressure process eliminates the need for vacuum conditions and offers the possibility of creating switchable patterns through thermal removal and reapplication of the PECA layer.

3.5.2 Ion irradiation. Ion beams can interact with polymeric surfaces, such as PDMS, to create a stiff silica-like skin layer through processes of chain scission and crosslinking.[232,243,244] A strain mismatch between this modified surface layer and the underlying substrate can generate compressive stress that, in turn, results in wrinkle formation. Pattern morphology is tuneable *via* processing parameters including ion beam acceleration voltage, fluence, and ion-incidence angle, for instance, transitioning from isotropic patterns at low fluence (Fig. 10c(i)) to more complex hierarchical patterns (discussed in Section 6) at higher fluences (Fig. 10c(ii)).[232,243,245]

Ion beam-induced wrinkling has been demonstrated with a variety of polymers. In block copolymers such as styrene-*b*-isoprene-*b*-styrene (SIS), ion irradiation induces selective crosslinking of the surface layer (Fig. 10c(iii)),[233,246] specifically unsaturated isoprene segments, while the styrene blocks provide structural integrity, creating a stiffness gradient that drives pattern formation. Diamond-like carbon (DLC) films have also been wrinkled using ion beam bombardment,[247] with high aspect ratio wrinkles achieved by combining ion beam prepatterning with carbon film deposition at varying angles.[247,248]

Localized patterning is supported by this technique, employing masking during ion beam exposure to spatial control of wrinkling morphology, transitioning from ordered structures near pattern edges to labyrinthine patterns in central regions.[95] Pattern formation is highly tunable through multiple parameters including substrate properties (such as PDMS curing temperature), selection of ion species (*e.g.*, hydrogen or argon), and irradiation time, enabling applications ranging from liquid crystal alignment to biomedical surface modification.[56,249–251] This technique offers precise control over pattern characteristics through beam parameters, though it requires specialized equipment and careful control of irradiation conditions.

3.5.3 Acid/base treatment. Chemical modification through pH adjustment provides another route to induce surface wrinkling. For instance, when PDMS is exposed to mixtures of sulfuric acid (H_2SO_4) and nitric acid (HNO_3), its surface undergoes oxidation, creating a bilayer system where a stiff oxidized layer develops atop the softer bulk 'substrate'.[252,253] This oxidation is visible by a color change from optically transparent to white, and the wrinkling wavelength can be controlled by varying the duration of acid exposure. Notably, acid treatment not only induces wrinkle formation but can also erase existing patterns, enabling dynamic and reversible surface texturing. This concept has been demonstrated in a dual-responsive system where the skin comprises a supramolecular network of pyridine copolymer (P4VP-nBA-S) and hydroxyl distyrylpyridine (DSP-OH),[254] exhibiting both topographical changes through wrinkling and optical changes through fluorescence when exposed to acid gas. The mechanism involves an acid-induced disruption of hydrogen bonding, which causes network breakage and stress release while color shifting from blue to orange-red upon protonation. The reversible nature of these changes, achieved through thermal treatment, makes such systems attractive for applications requiring switchable surface patterns.

Recent work has expanded this concept to include dually crosslinked networks incorporating mechanical bonds, noncovalent topological interlocking that permits molecular sliding, alongside dynamic covalent bonds.[234,255] Yang *et al.*[234] developed a mechanically interlocked network (MIN) containing [2]rotaxane crosslinks and nitrobenzyl-caged ureidopyrimidinone (NB-UPy) units that provide quadruple hydrogen bonding (Fig. 10d). Each crosslinking type responds selectively to chemical stimuli, creating two independent pathways for controlling surface topography. Exposure to HCl vapor causes rapid breakdown of hydrogen bonds, destabilizing the network structure and erasing wrinkles within minutes. Following acid exposure, thermal annealing can restore wrinkled morphology, though the regenerated patterns differ structurally from the original configuration due to network reorganization (Fig. 10d(i)). Conversely, treatment with Et_3N vapor selectively interferes with the rotaxane host–guest recognition without compromising overall network integrity. The resulting intramolecular movement within rotaxane units releases stress, causing wrinkles to

Open Access Article. Published on 31 March 2026. Downloaded on 4/22/2026 5:53:25 AM. This article is licensed under a Creative Commons Attribution 3.0 Unported Licence.

disappear gradually even after the sample is removed from the base environment. Thermal treatment following base exposure regenerates wrinkles that closely match the original pattern (Fig. 10d(ii)). By integrating complementary responsive elements, such systems achieve multifaceted control spanning different pH conditions, variable contact requirements, contrasting response timescales, and distinct regeneration outcomes ranging from irreversible structural changes to reversible pattern restoration.

3.6 Electrically-induced mechanisms

Surface instabilities in thin films can be induced through electrical stimuli, employing electric fields to create patterns through dielectric forces in polymer films or *via* electrophoresis in charged hydrogel systems, generating wrinkles through ionic migration and complex formation. These methods offer opportunities for creating dynamically tunable surface patterns with reversible and spatially programmable control.

3.6.1 Dielectric instability. Electric field-induced surface instabilities in dielectric media were exploited by Schäffer *et al.*,[256] subjecting dielectric materials to electric field gradients. In their experimental setup, a polymer film heated above its glass transition temperature was placed between two electrodes with an air gap, leading to surface undulations dependent on field strength and annealing conditions, sparking further studies that revealed distinct surface instability modes, including creases and wrinkles, with their formation governed by polymer surface energy, shear modulus, and thickness.[257–259] Ende and coworkers[260] advanced this concept by developing a system comprising an acrylate-based elastomer sandwiched between an ITO-coated glass panel and a thin gold top electrode, where the latter's excellent fatigue characteristics enabled it to function as a deformable electrode. Their work revealed a spontaneous transition from flat to wrinkled states beyond a critical voltage threshold. Interferometric height measurements of wrinkles demonstrated voltage-dependent pattern formation influenced by both elastomer thickness (H) and gold electrode thickness (h) (Fig. 11a). Lin *et al.*[261] further incorporated a rigid dielectric layer between a printed bottom electrode and the elastomer layer, which effectively constrained lateral expansion and further facilitated anisotropic pattern formation. Overall, these studies established the feasibility of triggering and controlling out-of-plane wrinkling instabilities through electric fields, achieving reversible pattern formation without mechanical strain, a capability particularly valuable for applications in smart optics and adaptive surfaces.

3.6.2 Electrophoresis. The formation and modulation of surface wrinkling *via* electrophoresis was demonstrated by Kato and coworkers[262] employing charged hydrogels. Their initial studies focused on wrinkle formation at the interface between two hydrogels with opposing charges, specifically copolymer

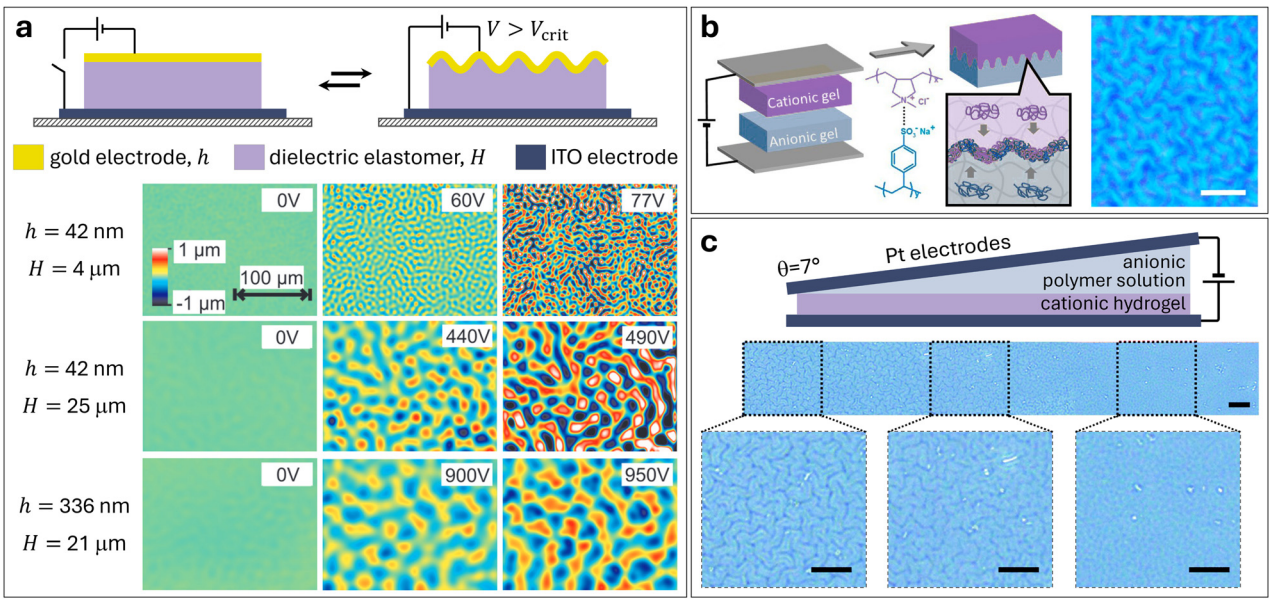

Fig. 11 Electrically-induced isotropic wrinkling through dielectric instability and electrophoresis. (a) Voltage-triggered wrinkling in dielectric elastomer systems: schematic showing device architecture with gold electrode/dielectric elastomer/ITO electrode configuration before and after voltage application, demonstrating wrinkle formation when the applied voltage exceeds a critical threshold ($V > V_{crit}$). Interferometric height maps showing surface morphology below and above the critical voltage for various elastomer thicknesses (H) and gold electrode thicknesses (h), revealing voltage-dependent pattern formation. Adapted with permission.[260] © 2013, Wiley-VCH. (b) Electrophoresis-driven wrinkling in ionic hydrogel bilayers: device schematic illustrating cationic and anionic gel layers between electrodes with corresponding polymer chemical structures. Electrostatic interactions at the gel interface generate surface instabilities, visualized by phase-contrast microscopy (scale bar: 10 μm). Adapted with permission.[262] © 2016, American Chemical Society. (c) Gradient pattern formation using sloped electrode geometry: experimental configuration with tilted platinum electrodes positioned above the anionic polymer solution (sodium poly(styrenesulfonate)) and cationic hydrogel layer. Phase-contrast microscopy demonstrates spatial variation in wrinkle morphology from dense labyrinthine patterns to sparse features across the sample, with magnified views showing morphological transition (scale bars: 30 μm). Adapted with permission.[263] © 2019, Royal Society of Chemistry.

Open Access Article. Published on 31 March 2026. Downloaded on 4/22/2026 5:53:25 AM.
This article is licensed under a Creative Commons Attribution 3.0 Unported Licence.

gels and semi-interpenetrating polymer networks (semi-IPNs), where one polymer network is crosslinked while another remains linear and entangled within it (Fig. 11b). When these cationic and anionic hydrogels were subjected to an electric field, the charged polymer chains migrated toward their respective electrodes due to electrophoresis, forming polyion complexes (PICs) at the interface. This process, coupled with the elasticity mismatch between the hydrogels, generated wrinkles visible under phase-contrast microscopy that enhanced interfacial adhesion (Fig. 11b).

A simplified system replacing the anionic gel with a polymer solution was subsequently developed,[263] whereby poly(diallyldimethylammonium chloride) (PDDA) served as the cationic component within the hydrogel network and poly(styrenesulfonate) (PSS) as the anionic polymer in solution. When an electric field was applied, PSS chains migrated toward the PDDA-containing hydrogel surface, forming a PIC layer that induced surface wrinkling. Wrinkling wavelength was adjusted by electric field strength, demonstrated using a tilted electrode configuration that created a gradient of field intensities and consequently a gradient of wrinkle periodicities (Fig. 11c), accompanied by a spatial variation in wrinkle morphology from dense labyrinthine patterns to sparse features. This electrophoretic approach operates under mild aqueous conditions at room temperature, making it particularly suitable for soft matter and biointerface applications requiring gentle processing. Recent work has extended this approach to create antifouling coatings by electrodepositing anionic cellulose nanocrystals (CNCs) onto cationic hydrogel surfaces, where the elastic mismatch between the CNC layer and hydrogel substrate generates wrinkled structures with tunable dimensions controlled by the hydrogel's elastic modulus.[264] The resulting wrinkled surfaces exhibit enhanced hydrophilicity and oil-repellency in aqueous environments, demonstrating the potential of electrophoretic wrinkling for developing simple, cost-effective antifouling coatings for underwater applications.

4 Characterization of isotropic wrinkles

The characterization of isotropic wrinkling patterns involves the quantitative assessment of pattern dimensions, structural order, and morphological classification. We next discuss the various imaging and scattering approaches employed to characterize wrinkled surfaces, the analytical methods used to extract pattern wavelengths, amplitudes, spatial organization and disorder, and computational frameworks that complement experimental observations.

4.1 Imaging techniques

Isotropic wrinkling patterns can be examined using a variety of microscopy, surface analysis and scattering techniques, with associated spatial resolution and dynamic range (minimum and maximum dimensions), contrast mechanisms, temporal frequency, and accessibility (Fig. 12a). The choice of imaging and scattering method depends evidently on factors including wrinkle dimensions, substrate properties, contrast, and time-resolution requirements, if the pattern evolves in time and/or under environmental conditions or external stimuli.

Optical microscopy provides a rapid, non-destructive approach for initial pattern assessment, offering wide field-of-view imaging that captures the global organization of labyrinthine structures (Fig. 12a(i)).[96] This technique is suitable for micron-scale wrinkles with moderate contrast and enables real-time monitoring during dynamic processes such as solvent exposure. However, diffraction-limited resolution (approximately 200–300 nm) and limited depth sensitivity make it unsuitable for submicron or shallow wrinkles. Phase-contrast microscopy enhances visualization of transparent samples, including hydrogels, making it suitable for characterizing patterns whose height variations produce only minor optical intensity differences (Fig. 12a(ii)).[262] Overall, optical microscopy is well suited to quantify microscale pattern wavelengths and wrinkling domains, as well as pattern evolution without requiring labeling or coating, albeit offering primarily qualitative height information.

Stylus and optical profilometry, employing vertical scanning interferometry, can measure both wrinkling wavelength and amplitude over large areas (square millimeters) with sub-μm vertical resolution (Fig. 12a(iii)), depending on the specific modality and surface properties.[229,260] Its non-contact nature preserves soft surfaces and is valuable for measuring wrinkle amplitudes and generating topographic maps of large patterned areas. Confocal laser scanning microscopy (CLSM) offers optical sectioning capabilities that enable three-dimensional reconstruction of wrinkled surfaces with improved depth discrimination compared to conventional optical microscopy (Fig. 12a(iv)),[231] and is particularly useful for mapping topographies across varying heights in thick or optically complex samples.

Atomic force microscopy (AFM) provides high-resolution topographical information through direct mechanical probing of the surface, generating detailed three-dimensional maps with sub-nanometer vertical resolution (Fig. 12a(v)).[133] AFM is ubiquitous in the quantification of fine wrinkling features, local amplitude, and curvature, and can additionally provide mechanical property maps correlated with wrinkle geometry. Limitations include generally smaller scan areas (typically $<100^2$ μm^2 without stitching), slower imaging speeds, and potential tip-sample interactions and artifacts that can affect soft material imaging. Scanning electron microscopy (SEM) provides also high-resolution imaging, revealing fine structural details of patterns (Fig. 12a(vi)).[178] However, insulating polymer samples often require a conductive coating (such as an evaporated metal), which may alter wrinkle morphology, and the technique provides limited quantitative height information. Cross-sectional SEM imaging of fractured or sectioned samples additionally provides direct visualization of wrinkling profiles, and subsurface bilayer structure. Electron microscopes generally operate at low pressures, which also impacts the study of environmental or dynamic/actuated systems, although low-vacuum and environmental microscopy is possible with various tradeoffs.

Open Access Article. Published on 31 March 2026. Downloaded on 4/22/2026 5:53:25 AM.
This article is licensed under a Creative Commons Attribution 3.0 Unported Licence.

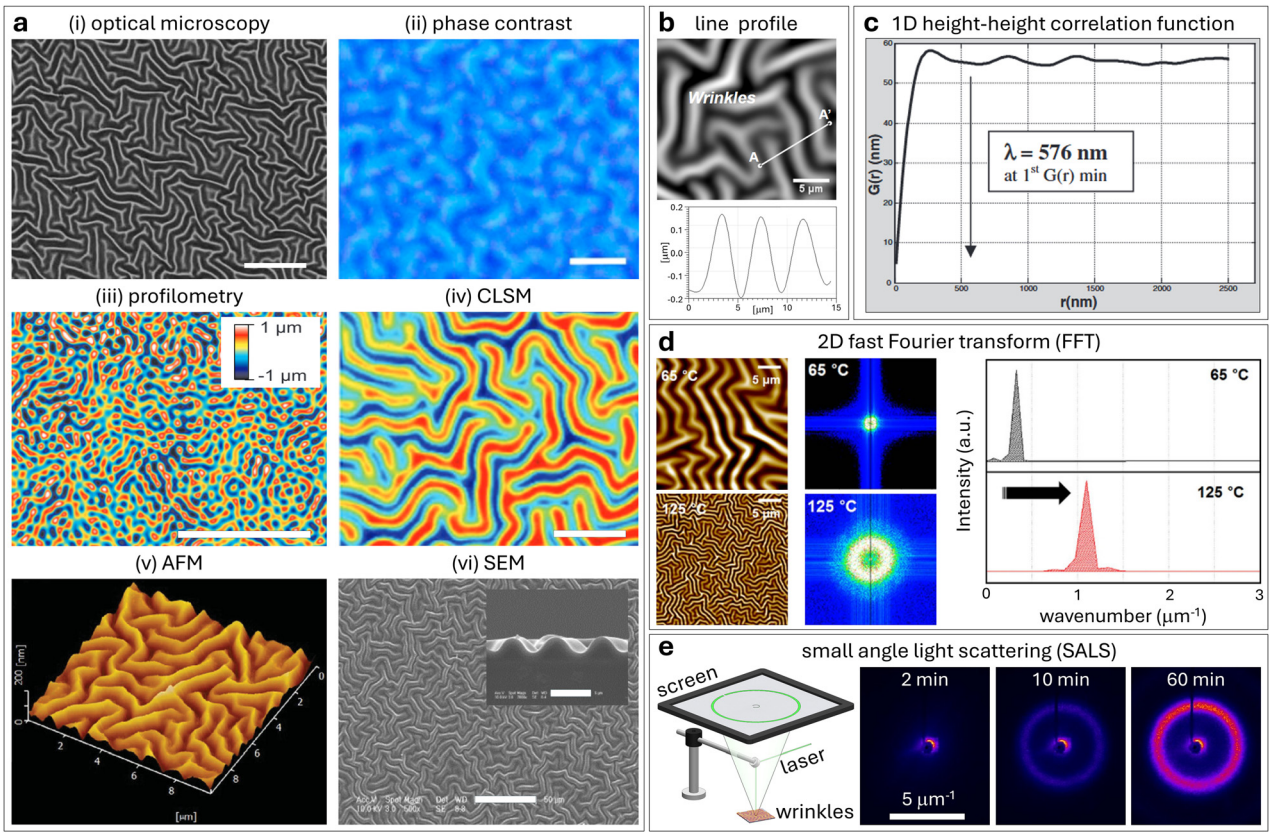

Fig. 12 (a) Imaging techniques for characterizing isotropic wrinkle patterns. (i) Optical microscopy of wrinkles in plasma-oxidized PDMS film after mechanical stretching (scale bar: 20 μm). Adapted with permission.[96] © 2008, Royal Society of Chemistry. (ii) Phase-contrast microscopy of the wrinkled interface of adhered gel bilayers induced by electrophoresis (scale bar: 10 μm). Adapted with permission.[262] © 2016, American Chemical Society. (iii) Optical profilometry using vertical scanning interferometry showing a surface height map of the voltage-induced wrinkles in the dielectric elastomer between electrodes (scale bar: 100 μm). Adapted with permission.[260] © 2013, Wiley-VCH. (iv) Confocal laser scanning microscopy (CLSM) of wrinkles formed through ethyl cyanoacrylate interfacial polymerization on an epoxy substrate (scale bar: 25 μm). Adapted with permission.[231] © 2024, Wiley-VCH. (v) Atomic force microscopy (AFM) in tapping mode revealing three-dimensional topography of thermally-induced wrinkles in a functional polymer/PDMS bilayer *via* Diels–Alder crosslinking. Adapted with permission.[133] © 2016, Wiley-VCH. (vi) Scanning electron microscopy (SEM) showing the top view (scale bar: 50 μm) and cross-sectional morphology (inset, scale bar: 5 μm) of wrinkles in a UV-cured liquid prepolymer film. Adapted with permission.[178] © 2017, Elsevier. (b)–(e) Methods for quantifying isotropic wrinkle wavelength: (b) AFM image showing isotropic wrinkles with corresponding line profile analysis along A–A′. Adapted with permission.[176] © 2011, Springer Nature. (c) Height–height correlation function $G(r)$ analysis revealing a characteristic wavelength of 576 nm at the first minimum for wrinkles generated by plasma oxidation of PDMS. Adapted with permission.[265] © 2007, IOP Publishing. (d) AFM topography images showing wrinkle patterns on PDMS films annealed at 65 °C and 125 °C followed by ion beam irradiation, with corresponding 2D Fast Fourier Transform (FFT) patterns (center) and wavenumber intensity distributions (right). Adapted under the terms of the CC BY 4.0 license.[249] © 2015 The Authors. (e) Small-angle light scattering (SALS) setup: schematic showing the laser and detection screen configuration for real-time characterization. Time-resolved SALS patterns demonstrating progressive wrinkle development during moisture sorption in an oxidized PDMS film. Adapted under the terms of the CC BY 4.0 license.[135] © 2025 The Authors.

The complementary nature of these imaging techniques often necessitates employing several approaches to characterize wrinkling patterns across scales. A practical consideration in characterizing wrinkled surfaces is the distinction between true morphological features and imaging artifacts. The finite depth of field of imaging approaches means that wrinkle crests and troughs may not be simultaneously in focus, potentially introducing contrast inconsistencies that may be misinterpreted as structural features; confocal laser scanning microscopy and vertical scanning interferometry mitigate this limitation through optical sectioning and non-contact surface profiling respectively. The deposition of conductive metal layers for electron microscopy imaging can alter wrinkling morphologies and thus introduce artifacts, and therefore, minimizing coating thickness, limiting beam exposure time, and using low-voltage imaging is recommended to mitigate these effects. Contact imaging techniques, such as stylus profilometry or AFM, are susceptible to tip-sample convolution artifacts, and thus light tapping conditions and well-characterized tips are recommended to ensure fidelity. Cross-referencing observations across multiple complementary techniques, for instance combining non-contact optical methods with high-resolution scanning probe measurements, or measurements in real- and reciprocal-space, is arguably the most reliable strategy to elucidate wrinkling morphology with minimal artifacts. While this review focuses on the most commonly employed methods, the

Open Access Article. Published on 31 March 2026. Downloaded on 4/22/2026 5:53:25 AM. This article is licensed under a Creative Commons Attribution 3.0 Unported Licence.

characterization toolkit continues to grow and evolve, with advanced techniques such as grazing-incidence small-angle X-ray scattering (GISAXS), digital holographic microscopy (DHM), digital image correlation (DIC), and transmission electron microscopy (TEM), offering complementary structural or dynamic insights into wrinkled surfaces.

4.2 Image analysis of global wrinkling wavelength and amplitude

Labyrinthine patterns requires additional metrics compared to, for instance, uniaxial counterparts, whose wavelength and amplitude can be obtained from a single profile perpendicular to the wrinkle direction.[96,116] A full description of isotropic morphologies must account for the multidirectional nature and local order ('grain' size, shape, and orientation) of isotropic patterns. Nevertheless, an initial approach generally involves extracting line profiles, employing AFM or optical profilometry, along a direction of local alignment within a 'crystalline grain' (Fig. 12b).[176] This provides high-resolution local information on wrinkle wavelength and amplitude, but is inherently one-dimensional and overlooks orientational variations in complex patterns. Multiple line profiles across different 'grains' are hence required to obtain representative measurements and distribution functions. A complementary statistical approach is provided by the height-height correlation function (HHCF), which measures how surface height correlates as a function of lateral separation.[163,265] The dominant wrinkle periodicity can be extracted from the first minimum of this function (Fig. 12c), while the decay of correlation provides insight into the degree of spatial order: slow decay indicates long-range correlation and more ordered patterns, while rapid decay indicates disorder. This method captures ensemble behavior rather than local variations, making it well-suited for disordered or globally isotropic patterns. Evidently, a range of spatial correlation functions can be computed and evaluated.

Two-dimensional fast Fourier transform (2D FFT) analysis converts real-space surface data into its spatial frequency domain components, providing complementary information about both wavelength and directional ordering.[109,117,135,207,246,249,266] For isotropic wrinkles, the 2D FFT produces a characteristic ring pattern in reciprocal space, where the wavenumber at maximum intensity (or the 'radius' of the ring), q^* corresponds to the inverse of the wrinkle wavelength, as $q^* \equiv 2\pi/\lambda$ (Fig. 12d).[62,267] An azimuthal average of the 2D FFT at q^* is employed to ensure the angular independence of the profile, followed by a radial average of 2D FFT to enable an accurate extraction of the dominant wavenumber q^* and its associated distribution.[249] Sharp peaks in the radial distribution indicate highly regular periodicity, while broader peaks show greater wavelength heterogeneity, often associated with defects and grain boundaries. This analysis is routinely performed on real-space images, acquired by microscopy or imaging techniques.

4.3 Scattering in pattern quantification

Small-angle light scattering (SALS) of a wrinkled surface yields a scattering pattern analogous to the output of 2D FFT analysis of a wrinkling pattern. In SALS, a light beam impinges onto the wrinkled surface at normal incidence, in transmission or reflection geometry. Generally, the footprint of the beam, (typically a laser), is larger than the 'grain' size of the wrinkling pattern, and the scattered light captured on the detector (or imaging plate) yields the characteristic ring profile of isotropic patterns in Fourier space (Fig. 12e).[135,146,268] The periodic surface patterns act as a diffraction grating, with the wavenumber corresponding to the ring radius being inversely proportional to wrinkle wavelength, written as $q^* = 2\pi/\lambda$. Employing focusing optics, a beam of small footprint (albeit with greater divergence) can be used to raster along the sample and record a series of 1D 'polycrystalline' diffraction profiles effectively.

The diffraction intensity profile also enables the pattern amplitude to be estimated through data modelling using Fourier optics,[57,62,135,267] where scattering depends on both spatial frequency and surface height modulation. This quantitative framework supports the predictive design of structural color for biomimetic and device applications, including for orientation-independent color.

SALS provides non-contact, large-area characterization with real-time monitoring capabilities, making it valuable for studying dynamic processes such as heating or swelling. While lacking the local spatial resolution of real-space approaches, SALS provides statistically robust measurements (typically over millimeter scales), without requiring mathematical operations such as 2D FFT and associated image manipulation, with minimal sample preparation. Together, these techniques provide complementary views across length scales from nanometers to macroscales, enabling comprehensive analysis of wrinkle wavelength, amplitude, and their associated spatial distributions.

4.4 Local pattern order and 'grain' envelope

The presence of a ring profile or 'powder average' in a 2D FFT or diffraction pattern alone is insufficient to identify and characterize isotropic wrinkling, and indeed similar patterns can arise from disordered patterns, including hexagonal arrangements (Fig. 13a).[213] A key distinguishing feature is that isotropic wrinkles exhibit locally single wave numbers (and associated distribution), while hexagonal patterns, for instance, show three characteristic wave vectors locally.[6,213,269] This observation has led to a refined definition of labyrinthine patterns as structures showing short-range order characterized by a single wave number combined with a powder spectrum.[15]

Isotropic wrinkling patterns can exhibit the same overall FFT ring profile and local wavenumber, despite large morphological differences, as illustrated in the numerical Turing-Swift–Hohenberg simulations of distinct pattern categories including 'fingerprint-type', 'glassy', and 'scurfy' labyrinthine patterns (Fig. 13b–e).[6] The type, density, and arrangement of pattern defects can result in diverse morphological manifestations, despite their shared underlying 1D characteristics, underscoring the need for more sophisticated analytical tools beyond the dominant length scale and global rotational invariance of these labyrinthine patterns. The distinction becomes apparent

Open Access Article. Published on 31 March 2026. Downloaded on 4/22/2026 5:53:25 AM.
This article is licensed under a Creative Commons Attribution 3.0 Unported Licence.

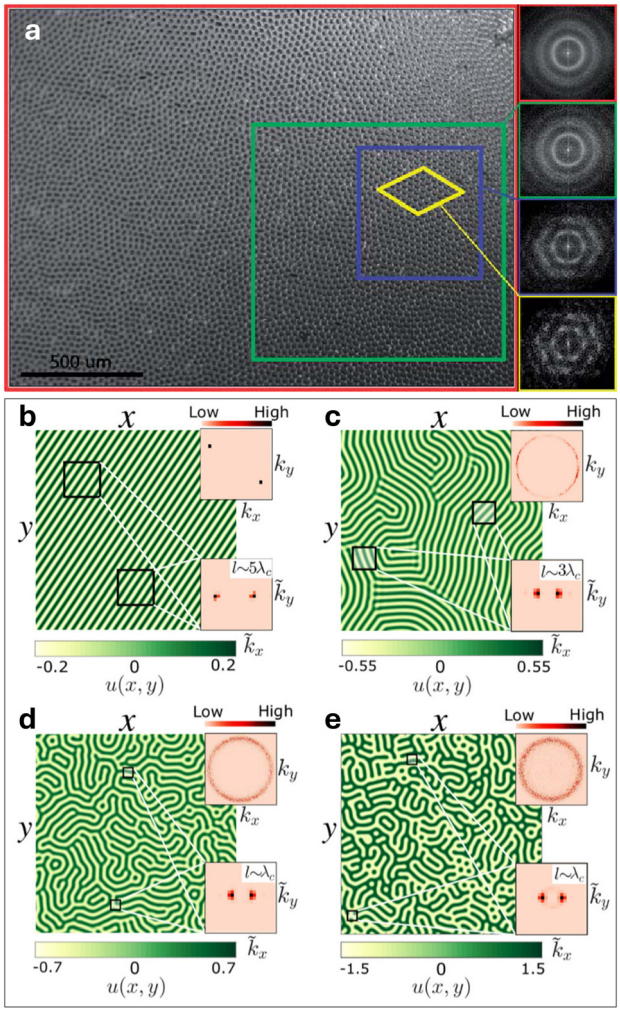

Fig. 13 Surface patterns and their Fourier transform analysis. (a) Large-area optical micrograph demonstrating dimple patterns formed by ethanol vapor exposure of UVO treated PDMS. Sequential FFT analyses of nested regions (red → green → blue → yellow boxes) reveal the emergence of hexagonal ordering at smaller length scales. Adapted with permission.[213] © 2011, Royal Society of Chemistry. (b)–(e) Numerical solutions of the Turing-Swift–Hohenberg equation showing evolution of pattern complexity: (b) striped pattern, (c) fingerprint-like labyrinthine pattern, (d) glassy labyrinthine pattern, and (e) scurfy pattern. Each panel includes both global (upper inset) and localized (lower inset) Fourier transforms, with the latter analyzed over windows of size l relative to the critical wavelength λ_c. (b)–(e) Adapted under the terms of the CC BY 4.0 license.[6] © 2020 The Authors.

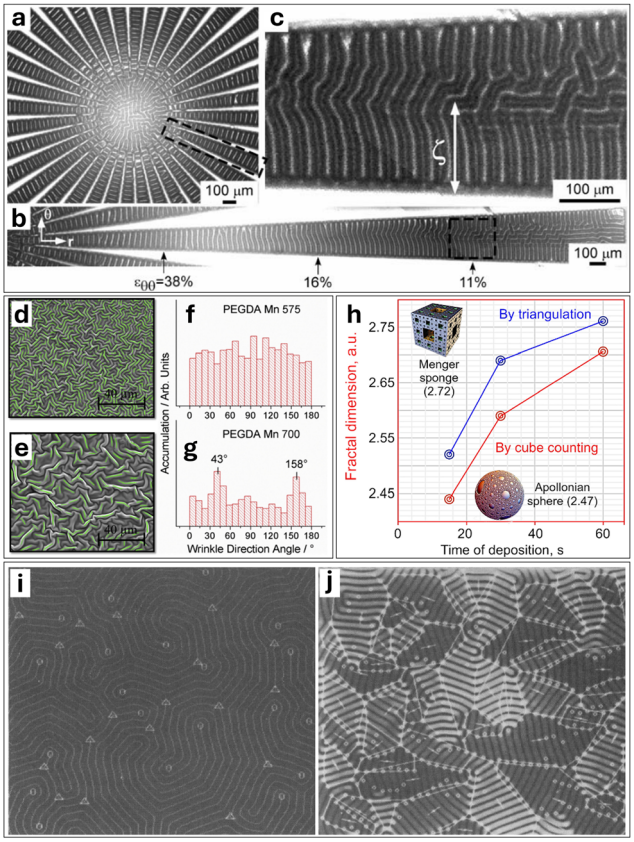

Fig. 14 Diverse approaches for characterizing isotropic wrinkle patterns. (a) Star-burst pattern demonstrating radially-oriented surface buckles generated through UVO line patterning. (b) Gradual transition from ordered to disordered wrinkles within a UVO stripe, with varying azimuthal strain values ($\varepsilon_{\theta\theta}$) indicated. (c) Determination of persistence length ζ at the order-disorder transition boundary. (a)–(c) Adapted with permission.[198] © 2006, Royal Society of Chemistry. (d) and (e) SEM micrographs showing wrinkle patterns formed using different molecular weights of hydrogel PEGDA: (d) PEGDA575 and (e) PEGDA700, with green lines highlighting wrinkle orientations. (f) and (g) Corresponding angular distribution histograms of wrinkle orientations for PEGDA575 and PEGDA700, respectively. (d)–(g) Adapted with permission.[217] © 2016, American Elsevier. (h) Evolution of fractal dimension with plasma deposition time, calculated using two different methods (triangulation and cube counting), with reference fractals shown in the insets. Adapted with permission.[165] © 2024, Elsevier. (i) and (j) Analysis of isotropic labyrinth patterns in ferrimagnetic garnet films: (i) skeleton analysis showing pattern defects – endpoints (circles) and branch points (triangles), (j) geometric analysis where polygonal boundaries (convex hulls) enclose segment clusters, with center lines indicating average segment orientation. (i) and (j) Adapted with permission.[21] © 1991, American Association for the Advancement of Science.

through localized Fourier analysis over windows of varying size relative to the characteristic wavelength and grain size, and can be rationalized by examining the spatial organization of pattern features, including persistence length, orientation distributions, and defect arrangements that global transforms cannot capture.

The wrinkle persistence length, defined as the distance a wrinkle maintains its direction before terminating or changing course, provides a useful handle into pattern organization (Fig. 14a–c).[198,211,270] This metric can be quantified through both direct measurement along wrinkle paths and theoretical frameworks based on how quickly wrinkle orientation decorrelates. Longer persistence lengths indicate more ordered structures, while shorter lengths signify greater disorder. Skeletonization techniques allow extraction of wrinkle centerlines, enabling detailed analysis of orientation distributions (Fig. 14d–g).[95,217,271] Angular distribution histograms reveal the degree of preferential alignment *versus* random orientation. These distributions can be quantified through order parameters that range from 0 (completely disordered) to 1 (perfectly aligned), providing a single metric for comparing different wrinkle patterns.

Open Access Article. Published on 31 March 2026. Downloaded on 4/22/2026 5:53:25 AM. This article is licensed under a Creative Commons Attribution 3.0 Unported Licence.

A fractal dimension analysis can also capture the space-filling nature of labyrinthine patterns, with values ranging between 1 and 2 for two-dimensional projections or 2 and 3 for surface topographies (Fig. 14h).[165,261] Fractal analysis quantifies pattern complexity through methods such as box counting or triangulation, revealing how complexity evolves with processing conditions. Higher fractal dimensions indicate more intricate, space-filling disordered structures. Additional metrics can then provide complementary perspectives on pattern organization. For instance, tortuosity measures path windiness, quantifying how much wrinkle paths deviate from straight lines.[261] Branching statistics characterize the frequency and geometry of wrinkle intersections.[176] Higher-order statistical moments of surface height distributions (skewness and kurtosis) enable scale-invariant roughness characterization.[272] Advanced mathematical tools, including Jacobian analysis of orientation fields and Minkowski functionals, provide geometric characterization through a set of morphological measures, including area, perimeter, and connectivity.[165,261,273]

In our view, a widely accepted, rigorous, and comprehensive framework to classify isotropic wrinkling patterns remains lacking, contrasting with adjacent fields such as liquid crystals,[274] ferromagnetic materials,[21,22] and block copolymer thin films,[275] where rigorous pattern classification is routine. In these established fields, defects are systematically categorized as point defects (disclinations) or line defects (dislocations), with topological charges assigned based on local symmetry breaking. Patterns are further characterized by their grain size, representing regions of locally uniform orientation separated by defects. Wrinkle patterns exhibit analogous features: ridge endings function as point defects while bifurcations represent line defect junctions. Defect density analysis quantifies these endpoints and branch points in skeleton representations (Fig. 14i), measuring structural discontinuities.[6,21] Complementary approaches include convex hull analysis, which characterizes segment clusters by identifying the smallest convex polygon containing each cluster (Fig. 14j) and reveals how wrinkle segments organize into larger structural units,[21] and Voronoi tessellation, which partitions space based on defect positions to quantify spatial correlations and clustering behavior.[276] Examination of wave vector fields enables classification of defect types and their spatial distribution, connecting local structural features to global pattern properties.[15,18,19,277,278]

4.5 Computational modeling

The analytical techniques described above can be complemented and extended through numerical simulations that computationally generate isotropic wrinkles. Such computational approaches provide opportunities for testing hypotheses about pattern formation mechanisms, exploring parameter spaces inaccessible to experiments, and validating analytical predictions.

Significant theoretical work has focused on understanding pattern selection between different morphologies (labyrinthine, herringbone, checkerboard, or striped) through analysis of elastic energy minimization under various stress conditions.[65,66,270,279] These studies revealed that the directionality and magnitude of applied stress fundamentally determine which pattern emerges. Particular attention has been directed toward coarsening dynamics on viscoelastic substrates, where patterns evolve gradually over time rather than forming instantaneously.[105,280,281]

Numerical approaches, particularly finite element modeling, have provided detailed insight into isotropic pattern formation by incorporating complex material behaviors, geometries, and loading conditions.[32,282–285] These simulations track progression from flat films through initial instability to fully developed patterns, thus providing insight into the spatiotemporal evolution of patterns that can be elusive in experiments. By introducing small perturbations, the models trigger bifurcation modes and capture subsequent evolution in single simulation runs. Simulations examining pattern transitions on bilayers subjected to an equibiaxial strain demonstrate this progression clearly.[66] At strain values just above the critical threshold, a square checkerboard pattern emerges, which progressively transitions into labyrinthine structures with increasing strain (Fig. 15). The corresponding Fourier transforms reveal pattern complexity evolution: checkerboard patterns produce discrete spots corresponding to single periodicities in orthogonal directions, while labyrinthine patterns generate broader rings signifying wavelength distributions and loss of directional order.

This observation highlights an important consideration: while uniaxial wrinkling theory predicts well-defined equilibrium wavelengths, isotropic wrinkles exhibit wavelength distributions due to their relative disorder and multi-grain nature, which is thus related to the number density and nature of defects

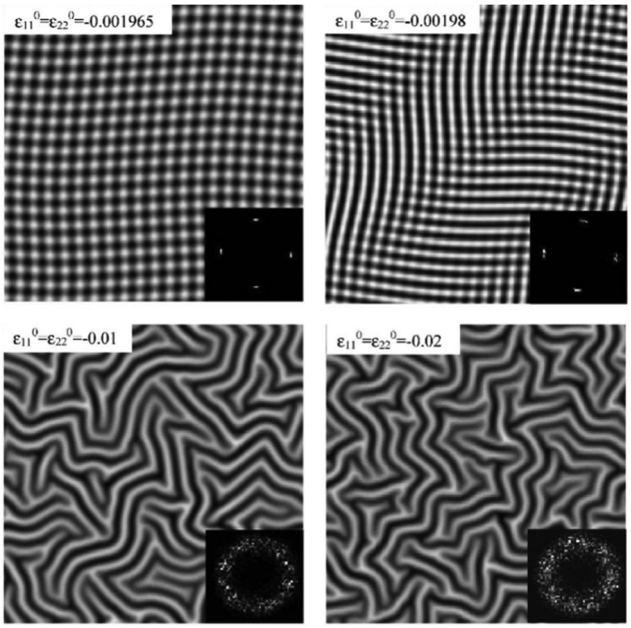

Fig. 15 Simulation results showing the evolution of wrinkle patterns under varying levels of isotropic strain. At strain values just above the critical threshold (ε_c = 0.00192), a square checkerboard pattern emerges, which progressively transitions into complex labyrinthine structures with increasing strain magnitude. The insets display the corresponding Fourier transforms. Adapted with permission.[66] © 2005, Elsevier.

Open Access Article. Published on 31 March 2026. Downloaded on 4/22/2026 5:53:25 AM. This article is licensed under a Creative Commons Attribution 3.0 Unported Licence.

and grain boundaries. Although simulations[66] show relatively small deviations, of less than 1%, between the (amplitude-weighted) average wavenumber in isotropic patterns from the uniaxial counterpart, for instance $\bar{k} \equiv \frac{\sum \hat{w}_{mn}^2 k_{mn}}{\sum \hat{w}_{mn}^2}$, where k_{mn} is the wavenumber and $\hat{w}_{mn}$ the amplitude, at a given grid point (m, n), with respect to the equilibrium wavenumber of striped patterns, further work is needed to quantitatively the distribution of periodicities and their significance in both computational and experimental systems. Understanding whether distributions represent equilibrium features or transient states, and their dependence on material properties and loading conditions, remains thus largely unexplored, potentially necessitating the refinement of theoretical frameworks for labyrinthine wrinkling patterns.

5 Applications

Isotropic wrinkling has been deployed across numerous applications that exploit their unique surface topography, tunable dimensions, and stimulus-responsive behavior. Surface patterns can modulate interfacial properties such as wetting and spreading,[111,139,159] adhesion,[52,241,286] and optical and photonic properties (including color and spectroscopic enhancement).[109,195,287,288] In biomedical applications, wrinkled substrates can influence cell behavior, from directing morphology and differentiation of marrow-derived stem cells to improving cytocompatibility and reducing genotoxicity.[56,203,205,289–291] The electrical and optical properties of wrinkled films have been leveraged to create flexible electronic and photonic devices, including perovskite-based optoelectronics, stretchable conductive films, photodetectors, and high-performance solar cells.[292–303] Wrinkled surfaces have also found practical utility in anti-fingerprint coatings and tactile wood surfaces that mimic natural skin-feel.[304,305] Studies of tactile perception have shown that humans can resolve sub-micron wrinkling patterns with amplitudes as low as 13 nm.[306] Coupled with rigorous mechanical and rheo-mechanical models, surface wrinkles have also enabled fundamental materials characterization, including measurement of elastic moduli, viscoelastic properties, and compressive strain in thin and ultrathin films.[132,211,268] Many wrinkled systems can be made dynamic and reversible through external stimuli including moisture, light, temperature, solvents, and electric fields, yielding smart surfaces that switch between different functional states.[68,260,307–309]

The overall mechanical response of wrinkled bilayer systems is largely governed by the thicker, substrate layer, often a soft elastomer, which may restrict some practical uses. This can be resolved or alleviated by inducing wrinkling in a transient manner, during processing, for example through thermal expansion mismatch, solvent swelling, or mechanical pre-strain, after which the substrate may stiffen upon cooling, crosslinking, or solvent removal while retaining the wrinkled morphology.[64,132] Wrinkled surfaces can also serve as molds or templates for pattern transfer into mechanically robust materials, decoupling the properties of the functional device from those of the original bilayer (*e.g.*, in cellulose films[310]). However, numerous target applications for isotropic wrinkled surfaces, including flexible electronics, conformal biomedical interfaces, and smart coatings, are precisely those where mechanical compliance is advantageous, and where deformation-induced pattern changes can be exploited as a functional response. The following subsections illustrate specific examples showcasing how isotropic wrinkles can be engineered to create functional materials by exploiting features such as controlled structural color, unique identification characteristics, switchable wettability, mechanical flexibility, enhanced electrical conductivity, and tunable surface activity.

5.1 Anti-counterfeiting

The unique and irreproducible characteristics of isotropic wrinkles make them ideal candidates for protecting valuable items such as official documents, jewelry, and medicines from forgery and duplication. Bae *et al.*[201] demonstrated how isotropic wrinkle patterns could serve as unique identification tags analogous to human fingerprints (Fig. 16a). Employing maskless lithography, polymeric microparticles with silica film coatings developed distinctive wrinkle patterns upon drying. These patterns exhibited characteristic features called minutiae, specifically ridge endings and bifurcations, analogous to identifying markers in human fingerprints (Fig. 16b), with tunable wrinkling wavelength, and patterns constrained within particles of various geometries (Fig. 16c). Importantly, each particle exhibited a unique and non-replicable wrinkling pattern that remained stable under severe environmental conditions, including temperature variations, swelling/deswelling cycles, and sonication.

This concept was further advanced through the development of Physical Unclonable Function (PUF) labels combining surface wrinkling with block copolymer phase separation.[312] The system employed anthracene-functionalized polystyrene-*block*-polybutadiene-*block*-polystyrene (SBS-CAN), where thermal annealing induced spinodal phase separation, creating continuous lamellar domains with fingerprint-like morphology at the nanoscale.[313,314] Subsequent UV exposure triggered gradient photocrosslinking that generated microscale wrinkles atop this nanostructured template (Fig. 16d). Dual-level structural control enabled information density over 1000 times higher than human fingerprints. To facilitate practical implementation, an authentication pipeline based on deep learning was developed for reliable pattern recognition. The field continues to evolve with the development of dynamic, reversible wrinkle patterns that respond to various stimuli like infrared light, visible light, or acid exposure, offering additional security features for anti-counterfeiting applications.[254,315–317]

5.2 Camouflage: tunable smart optical surfaces

The ability to dynamically alter surface appearance and blend with surroundings is widespread in nature, particularly exemplified by cephalopods like octopi and squid. These marine creatures utilize specialized cells called chromatophores

 This journal is © The Royal Society of Chemistry 2026

Open Access Article. Published on 31 March 2026. Downloaded on 4/22/2026 5:53:25 AM.
This article is licensed under a Creative Commons Attribution 3.0 Unported Licence.

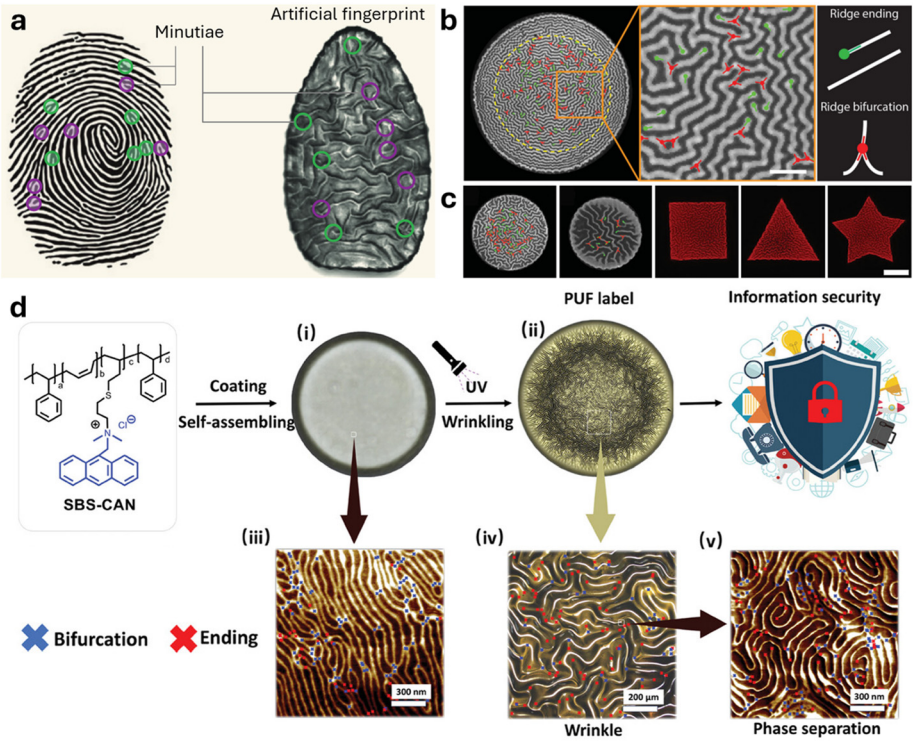

Fig. 16 Wrinkles for an unclonable anti-counterfeiting strategy. (a) Comparison between human fingerprints and artificial wrinkle patterns showing analogous minutiae features – ridge endings and bifurcations that provide unique identifying characteristics. Adapted with permission.[311] © 2015, Springer Nature. (b) Analysis of wrinkle pattern features showing ridge endings (green) and bifurcations (red) with their directional orientations, demonstrating the complexity and uniqueness of the patterns. Scale bar: 25 μm. (c) Examples of fabricated artificial fingerprints with tunable wavelengths for different security levels and various geometric shapes. Scale bar: 50 μm. (b) and (c) Adapted with permission.[201] © 2015, Wiley-VCH. (d) Development of a hierarchical PUF security label using the block copolymer SBS-CAN: (i) and (ii) formation of wrinkle patterns through UV exposure, and (iii)–(v) structural characterization showing nanoscale self-assembly and microscale wrinkle formation. Adapted with permission.[312] © 2024, Wiley-VCH.

(pigment-containing) and iridocytes (structural color-producing) to rapidly change their coloration and patterning.[318,319] Drawing inspiration from these biological systems, synthetic analogs using wrinkled polymer surfaces have been developed to achieve similar adaptive camouflage capabilities. A notable example involves a two-layer structure with an anthracene-containing polymer (PAN) film atop pigment-doped PDMS, where the PAN layer acts analogously to iridocytes while the pigmented PDMS mimics chromatophores.[196] Various light-responsive pigments like carbon nanotubes, iron oxide, and organic dyes have been incorporated to enable selective responses to different wavelengths.

The wrinkled state creates distinct optical effects through a combination of structural color from film interference and pigment coloration, making the pattern visible against the background. Upon light exposure (UV, NIR, or sunlight), the photothermal effect causes local heating and expansion of the pigmented layer, temporarily eliminating wrinkles and reverting the surface to a flat state that blends with surroundings. This transformation enables on-demand control over surface visibility, demonstrated through various configurations including annular patterns, butterfly shapes, and transparent designs using specialized polymers like isoindigo-Bodipy copolymers (Fig. 17a–d). System reliability has been verified through repeated switching cycles without loss of pattern fidelity (Fig. 17e), with applications extending beyond camouflage to dynamic diffraction gratings (Fig. 17f) and encryption.[175,193,309,320] The simplicity, versatility, and passive operation without external sensors make this approach particularly promising for practical adaptive camouflage applications.

5.3 Multifunctional user-interactive e-skin

The versatility of isotropic wrinkled surfaces has enabled significant advances in user-interactive electronic skins (e-skins), particularly for healthcare and human–machine interface applications. A notable demonstration combines thermotherapy with visual feedback through a device fabricated using wrinkled surfaces created by mechanical stretching and UV-ozone treatment (Fig. 18).[321] The device comprises a silver nanowire (AgNW) network as an active sensing layer deposited on the wrinkled surface, topped with thermochromic dyes that change color at specific temperatures (transitioning between blue, yellow, magenta, and colorless). When applied to body joints, the device's electrical resistance changes with movement, allowing controlled heat delivery while preventing burns through visual color indicators. The system demonstrates excellent mechanical properties, withstanding 100% strain and 1000 repeated cycles without degradation.

Open Access Article. Published on 31 March 2026. Downloaded on 4/22/2026 5:53:25 AM.
This article is licensed under a Creative Commons Attribution 3.0 Unported Licence.

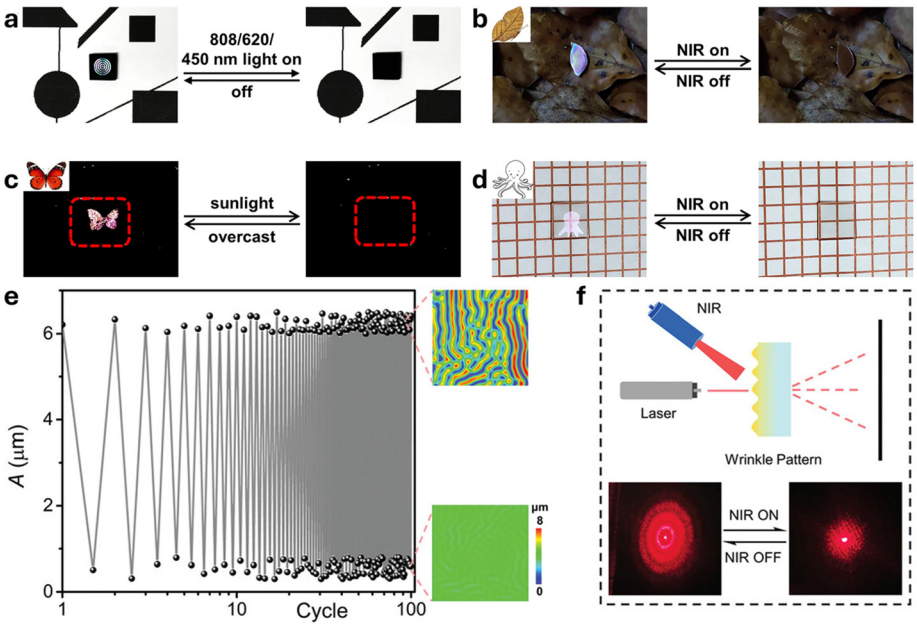

Fig. 17 Dynamic wrinkles for adaptive camouflage applications. (a)–(d) Demonstration of camouflage capabilities: (a) PAN/CNT-PDMS pattern responsiveness to different wavelengths of light, (b) PAN/cFe_2O_3-PDMS Kallima-inachus butterfly mimicry with NIR-triggered wrinkle formation, (c) PAN/CNT-PDMS sunlight-adaptive wrinkle patterns showing butterfly camouflage, and (d) PAN/PIB-PDMS octopus-inspired design showing pattern adaptation on a grid background. (a)–(d) Adapted with permission.[196] © 2021, National Academy of Sciences of the USA. (e) Durability assessment showing wrinkle amplitude over 100 formation/extinction cycles with corresponding confocal microscopy images of the wrinkle patterns (wrinkled state – top, smooth state – bottom). (f) Schematic illustration of NIR-controlled dynamic light diffraction with corresponding diffraction patterns in wrinkled (left) and smooth (right) states. (e) and (f) Adapted with permission.[175] © 2024, Wiley-VCH.

Expanding the material palette for such sensing platforms, alternative systems using conductive hydrogels, Au/PDMS films, and materials incorporating MXenes with ZnO nanowires or carbon nanotubes have been developed to create multi-dimensional sensors.[61,181,322,323] These systems can simultaneously detect multiple stimuli like pressure, strain, and movement, enabling applications ranging from robotic grip control to voice and textual recognition. The ability to integrate multiple functionalities while maintaining mechanical flexibility demonstrates the potential of wrinkle-based platforms for next-generation wearable technologies that actively interact with users through visual, thermal, and mechanical feedback mechanisms.

5.4 Water-repellant sensors

Isotropic wrinkled surfaces have emerged as a powerful platform for developing water-repellent electronic sensors that maintain functionality under mechanical deformation, a critical requirement for wearable electronics, robotics, and prosthetics. By combining reactive ion etching, thermal treatment, and selective deposition of conductive materials such as carbon nanotubes on textured PDMS surfaces, superhydrophobic sensors with water contact angles exceeding 165° have been achieved (Fig. 19).[324] This extreme water repellency results from the Cassie-Baxter wetting state, where air pockets trapped within wrinkled microstructures prevent water from fully wetting the surface.[325,326] The sensors exhibit impressive durability, withstanding 5000 stretching-relaxing cycles and 10 000 twisting cycles while maintaining superhydrophobic properties, along with high transparency both in air and underwater (Fig. 19). These characteristics make them suitable for tracking human motion when mounted on joints like fingers, wrists, or the forehead through resistance changes.

Recent advances have further expanded this concept using ionic conducting elastomers with wrinkled surfaces, where controlled movement of ionic species within the polymer network enables stable electrical conductivity even underwater.[327] This represents a significant advancement toward robust waterproof electronics that can operate reliably in challenging environments while maintaining mechanical flexibility and sensing capabilities.

5.5 Membrane separation

Isotropic wrinkled surfaces have demonstrated potential in advancing membrane separation technology, particularly for water purification applications. Tan and coworkers[328] incorporated nanosized wrinkles on polyamide (PA) membrane surfaces, which they referred to as 'Turing structures,' to enhance water permeability while maintaining excellent salt rejection, surpassing performance limits of conventional desalination membranes. The enhanced performance was attributed to the increased surface area provided by the wrinkled topology, which created preferential water transport pathways. Building on this concept, increasingly sophisticated approaches to generate controlled wrinkle patterns in membrane structures have been developed.[329–331]

Open Access Article. Published on 31 March 2026. Downloaded on 4/22/2026 5:53:25 AM.
This article is licensed under a Creative Commons Attribution 3.0 Unported Licence.

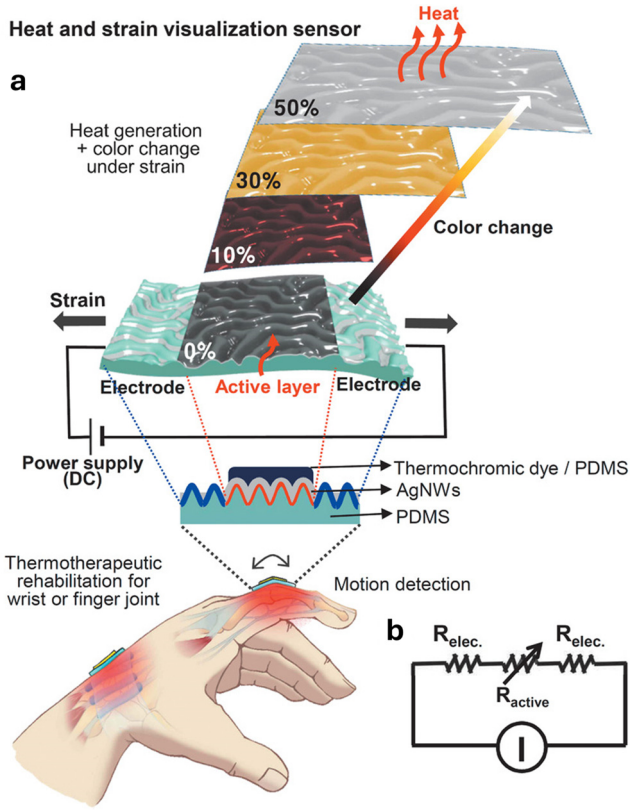

Fig. 18 Heat and strain visualization sensor employing wrinkled surfaces. (a) Schematic illustration of a stretchable device combining strain sensing with thermochromic visualization: the layered structure consists of wrinkled silver nanowire (AgNW) networks sandwiched between PDMS layers, with a thermochromic dye-PDMS composite as the active layer. The device demonstrates progressive color changes with increasing strain (0–50%) due to Joule heating generated by the AgNW network. Application as a thermotherapeutic rehabilitation device for wrist/finger joints is shown below. (b) Equivalent circuit diagram of the stretchable device showing the electrical resistance contributions from the electrodes (R_{elec}) and active layer (R_{active}). Adapted under the terms of the CC BY 4.0 mem.[321] © 2020 The Authors.

Recent work utilized cyclodextrin-based metal-organic framework (CD-MOF) nanoparticles to create precisely engineered nano-wrinkled polyamide membranes on polyethersulfone supports (PA/iCM/PES) (Fig. 20a).[332] This novel architecture, combining enhanced surface area with reduced membrane thickness, achieved a remarkable 617% increase in water permeance compared to conventional membranes while maintaining high selectivity (99% Na_2SO_4 rejection and 95% antibiotic rejection) (Fig. 20b and c). These developments highlight how controlled surface wrinkling offers a powerful platform for designing next-generation membrane materials with enhanced separation capabilities.

6 Higher order morphological patterns

The preceding sections have examined isotropic wrinkles from their fundamental formation mechanisms through characterization techniques to diverse applications. However, surface instabilities in bilayer systems can extend beyond regular sinusoidal profiles to generate more complex morphologies. Features, including folds, creases, cracks, and hierarchical structures, emerge when compressive strains exceed certain critical thresholds or when multiple instability modes are deliberately combined. Understanding and controlling these morphologies proves essential for advancing applications or mitigating undesirable outcomes in wrinkle-based technologies. This section examines three significant categories of higher-order surface patterns: folds and creases that form through surface self-contact, cracks that serve as either limiting factors or exploitable features, and hierarchical structures that integrate multiple length scales for enhanced functionality.

6.1 Folds and creases

When a bilayer system experiences mismatch strain below a critical threshold, the surface remains flat. Upon exceeding this threshold, various instability patterns emerge depending on system variables. Wang and Zhao[333] proposed a three-dimensional phase diagram mapping these surface instability modes (Fig. 21a).[333] The diagram uses three dimensionless parameters: mismatch strain (ε_M) between the film and substrate, film-to-substrate shear modulus ratio (μ_f/μ_s), and normalized interfacial adhesion energy ($\Gamma/(\mu_s H_f)$), where Γ represents the work required to detach the film from the unit substrate area and H_f is the film thickness. These parameters naturally emerge from the potential energy of the film-substrate system. The resulting phase space reveals distinct regions corresponding to wrinkles, creases, folds, period-doubling patterns, ridges, and delaminated buckles. This framework, validated through computational simulations, experiments, and biological observations, demonstrates that assuming substantial interfacial adhesion, various instability modes arise as systems with different modulus ratios experience increasing strain.

Creases and folds represent advanced morphologies that extend beyond smooth, periodic wrinkles. Creases manifest as sharp, self-contacting grooves that form abruptly on the surface once a critical strain is exceeded (Fig. 21b–d). Unlike the smooth undulations of wrinkles, creases appear as narrow, localized indentations resembling pinches or dimples, typically without regular wavelength spacing.[333,335] They signal that surface stress has concentrated into localized regions rather than being evenly distributed across the surface. Folds, in contrast, represent larger, more global out-of-plane deformations where the surface buckles upon itself, forming wave-like or crumpled structures (Fig. 21e–g).[176,333] Folds can evolve from pre-existing wrinkles through progressive strain: when wrinkle amplitude grows sufficiently large, neighboring peaks and troughs touch or overlap, creating self-contact with highly localized curvatures.

Crease formation has been extensively documented in swelling-responsive hydrogel systems. When constrained films swell upon solvent absorption, expansion perpendicular to the substrate generates biaxial compressive stress. Above the critical swelling ratio, the surface undergoes sudden localized

Open Access Article. Published on 31 March 2026. Downloaded on 4/22/2026 5:53:25 AM.
This article is licensed under a Creative Commons Attribution 3.0 Unported Licence.

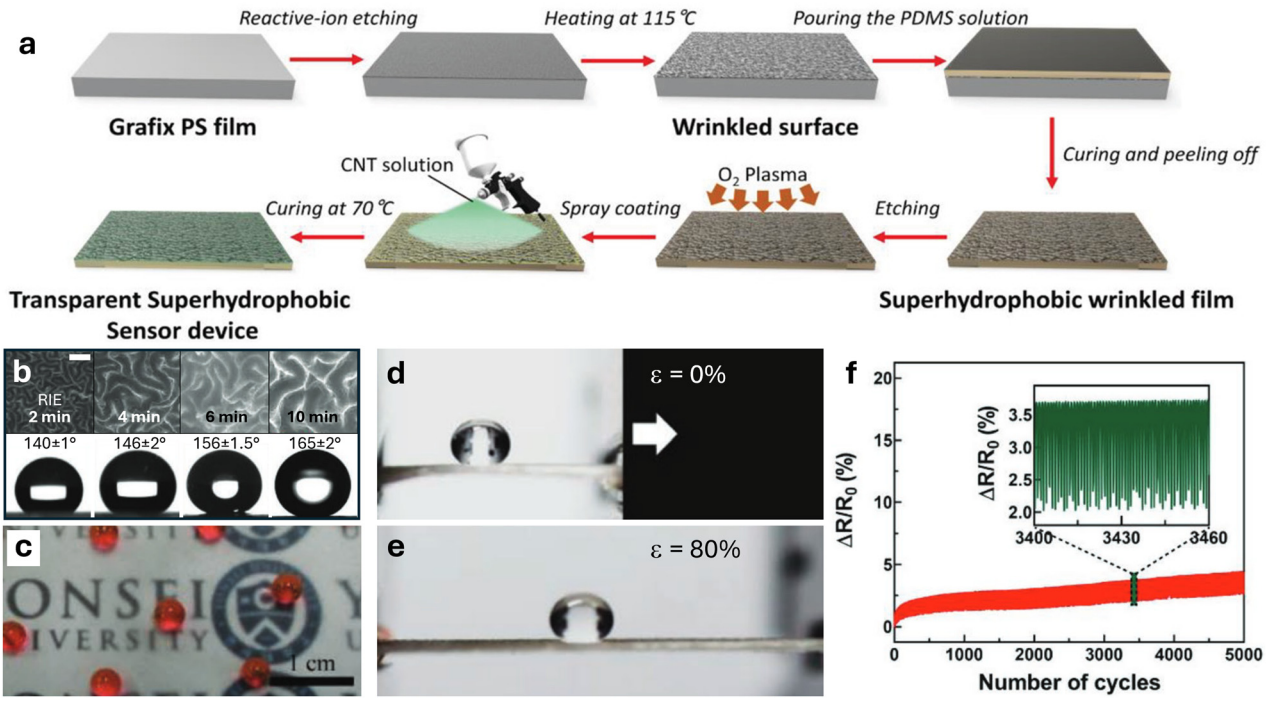

Fig. 19 Fabrication and characterization of a transparent superhydrophobic strain sensor based on wrinkled PDMS/CNT films. (a) Fabrication process involving reactive–ion etching of PS film, wrinkle formation, and sequential surface modifications to achieve the final transparent superhydrophobic device. (b) SEM images showing evolution of wrinkle morphology with increasing RIE treatment duration (2–10 min) and corresponding water contact angles demonstrating progressive enhancement of superhydrophobicity from 140° to 165°. Scale bar: 50 μm. (c) Demonstration of superhydrophobic behavior showing water droplets maintaining a spherical shape on the transparent surface. (d) and (e) Water droplet behavior on the sensor surface under different tensile strains: 0% and 80%, respectively. (f) Durability test showing normalized resistance change over 5000 stretching cycles at 10% strain (inset shows magnified view of cycles 3400–3460). Adapted with permission.[324] © 2019, Wiley-VCH.

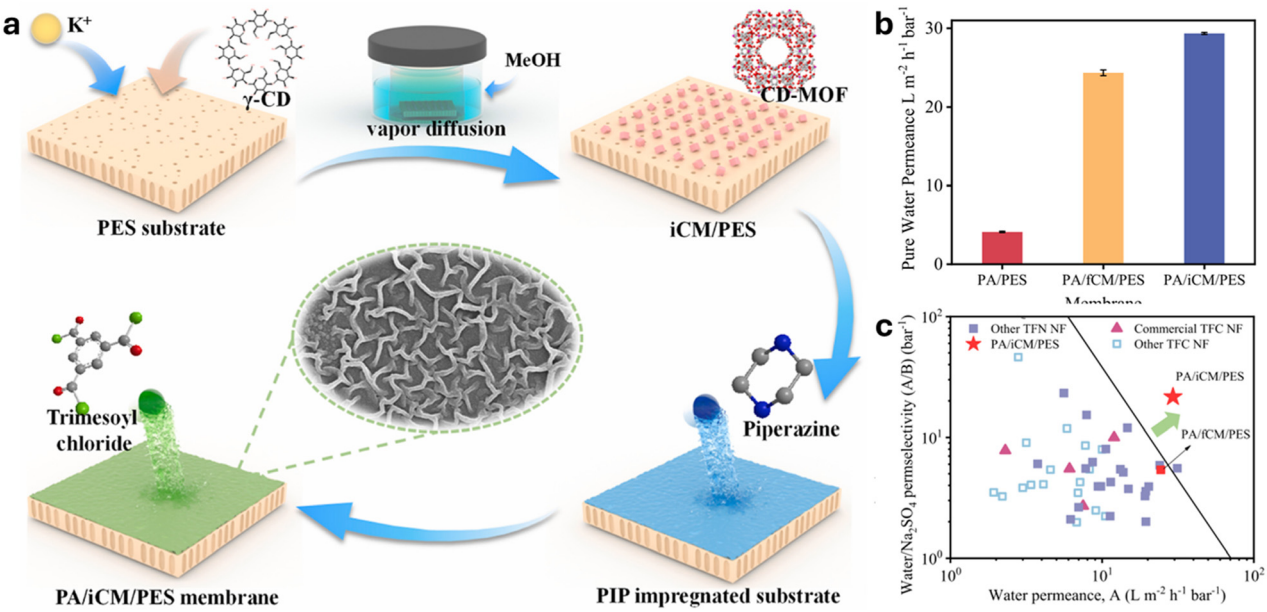

Fig. 20 Development and performance of wrinkled polyamide (PA) nanocomposite membranes for nanofiltration. (a) Schematic illustration of the membrane fabrication process: starting with a polyethersulfone (PES) substrate modified with γ-cyclodextrin (γ-CD), followed by methanol vapor diffusion to form cyclodextrin metal-organic frameworks (CD-MOF), and subsequent interfacial polymerization using trimesoyl chloride and piperazine to create the final PA/iCM/PES membrane. The SEM image (center) reveals the characteristic wrinkled surface morphology. (b) Pure water permeance (PWP) comparison between different membrane configurations, demonstrating enhanced performance with the incorporation of CD-MOF. (c) Performance comparison with existing thin-film nanofiltration (TFN) and thin-film composite (TFC) membranes, plotting water/Na_2SO_4 selectivity against water permeance, highlighting the superior performance of the wrinkled PA/iCM/PES membrane. Adapted with permission.[332] © 2024, Elsevier.

Open Access Article. Published on 31 March 2026. Downloaded on 4/22/2026 5:53:25 AM.
This article is licensed under a Creative Commons Attribution 3.0 Unported Licence.

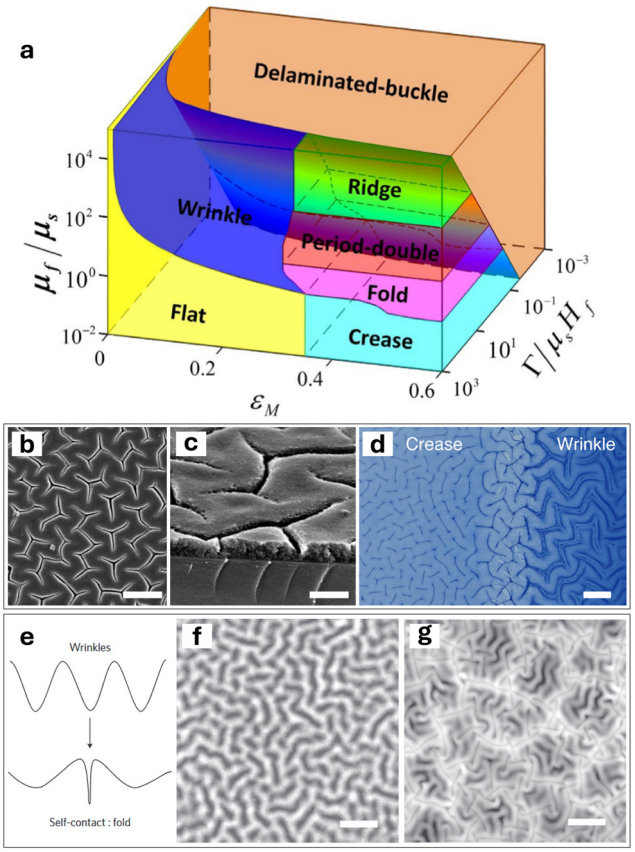

Fig. 21 Surface instability patterns and morphological transitions. (a) Phase diagram mapping instability patterns as functions of three dimensionless parameters: mismatch strain ε_M, film-to-substrate modulus ratio μ_f/μ_s, and normalized interfacial adhesion energy $\Gamma/(\mu_s H_f)$. Adapted under the terms of the CC BY 4.0 license.[333] © 2015 The Authors. (b, c) SEM image of a series of creases from the (b) top and (c) cross-sections in the silica/P2VP homopolymer film upon swelling. Scale bars: (b) 2 μm and (c) 500 nm. Adapted with permission.[334] © 2005, American Chemical Society. (d) Optical image showing the coexistence of creases and wrinkles in a thickness-gradient polyacrylamide hydrogel bilayer. Scale bar: 10 mm. Adapted under the terms of the CC BY 4.0 license.[153] © 2024 The Authors. (e) Schematic illustration showing the transition from wrinkles to folds through self-contact of adjacent wrinkle surfaces. (f) and (g) Morphological evolution under increasing compressive stress showing progressive development of complex wrinkle patterns, fabricated *via* UV exposure and ion irradiation. Scale bars: 5 μm. (e)–(g) Adapted with permission.[72] © 2012, Springer Nature.

collapse into creases. Hayward and coworkers[334] observed cuneiform-like creases in silica/homopolymer films (Fig. 21c), with spacing scaling linearly with film thickness. In PHEMA hydrogels, solvent quality controls morphology: water produces wrinkles while alcohols trigger wrinkle-to-crease transitions.[336] Ethanol swelling generates higher crease densities than water, indicating larger stresses.[337] Thickness gradients enable spatial control, with thicker regions developing creases and thinner regions exhibiting wrinkles (Fig. 21d).[153]

Folds evolve from wrinkles under progressive compression. Kim and coworkers[72,176] demonstrated this transition in ion-irradiated viscoelastic films, where increasing stress drove evolution from wrinkles to folds (Fig. 21e–g). When compressed beyond one-third of their wavelength, neighboring wrinkles annihilate to form deep crevices. These folds localized and trapped light, increasing polymer solar cell photocurrent by 47%. Similar transitions occur in metal–elastomer systems through stepwise deposition, with initial folds localizing stress and growing while eliminating neighboring wrinkles.[139] Thermoresponsive PNIPAM layers enable reversible fold formation for peristaltic motion and size-selective transport.[338]

6.2 Crack formation

Cracks represent surface tears in the stiff skin layer that appear as competing stress relaxation mechanisms, typically oriented along the direction of applied stress and transverse to surface undulations. While wrinkles relieve compressive stress through out-of-plane buckling, cracks release stress through in-plane fracture. For many applications employing wrinkled surfaces, cracks are undesirable as they restrict usable patterned areas, hinder reproducibility, and degrade function.[339,340] However, in certain contexts, controlled crack formation proves beneficial, finding applications in sensing, nanofluidic manipulation, and nanofabrication.[341–347]

Although crack formation is predominantly observed in mechanically stretched systems, cracks emerge across various induction methods, including metal deposition, swelling, plasma/UVO oxidation, and ion irradiation.[137,161,232,266,336,348] Understanding the conditions promoting crack formation and identifying process parameters to control it has been the focus of substantial research. Recent research elucidated how substrate thermal conductivity and film thickness influence crack

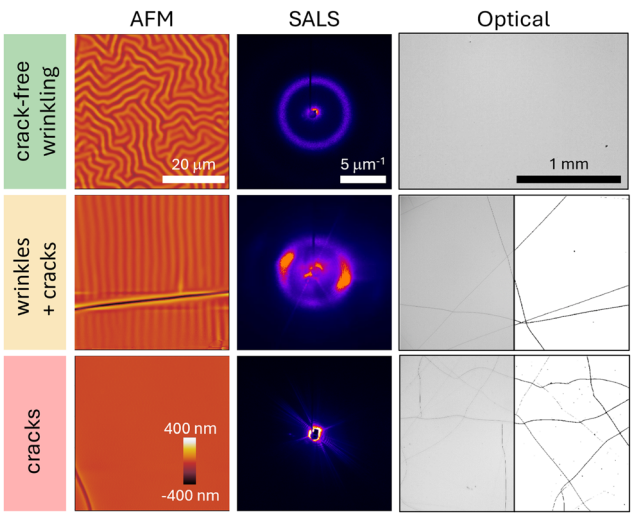

Fig. 22 Crack formation and suppression in plasma-oxidized PDMS films (H = 10.5 μm) controlled by substrate thermal conductivity. AFM topography (left), SALS diffraction patterns (center), and optical microscopy (right) reveal three distinct regimes: crack-free isotropic wrinkling on high thermal conductivity substrate (42 347 W m^{-2} K^{-1}) at the top, coexistence of wrinkles and cracks on intermediate thermal conductivity substrate (476 W m^{-2} K^{-1}) in the middle, and crack-dominated morphology on low thermal conductivity substrate (80 W m^{-2} K^{-1}) at the bottom exhibiting complete suppression of wrinkling. Adapted under the terms of the CC BY 4.0 license.[266] © 2024 The Authors.

Open Access Article. Published on 31 March 2026. Downloaded on 4/22/2026 5:53:25 AM.
This article is licensed under a Creative Commons Attribution 3.0 Unported Licence.

formation during plasma oxidation of PDMS,[266] identifying three distinct regimes (Fig. 22): crack-free isotropic wrinkling on high thermal conductivity substrates, coexistence of wrinkles and cracks on intermediate thermal conductivity substrates, and crack-dominated morphology with complete wrinkle suppression on low thermal conductivity substrates. Thin PDMS films (less than 100 μm) on substrates with high heat transfer coefficients (>1000 W m^{-2} K^{-1}) successfully suppress crack formation, yielding large-area crack-free wrinkled patterns. The substrate's thermal properties effectively control the thermal profile experienced during plasma treatment, enabling stress-free oxidized bilayer films through appropriate thermal design.

In addition to the thermal profile of the substrate, numerous other process parameters influence cracking. In plasma and UVO treatments, the choice of gas, pressure, exposure time, power, and dose all affect crack formation.[93,141,266,348,349] In metal deposition systems, film thickness plays a critical role: sufficiently thick films can develop crack patterns during deposition due to thermal tensile stress, which modifies local stress fields and alters wrinkle morphologies.[137] In swelling hydrogel systems, prolonged swelling time can cause fold depths to increase until compressive

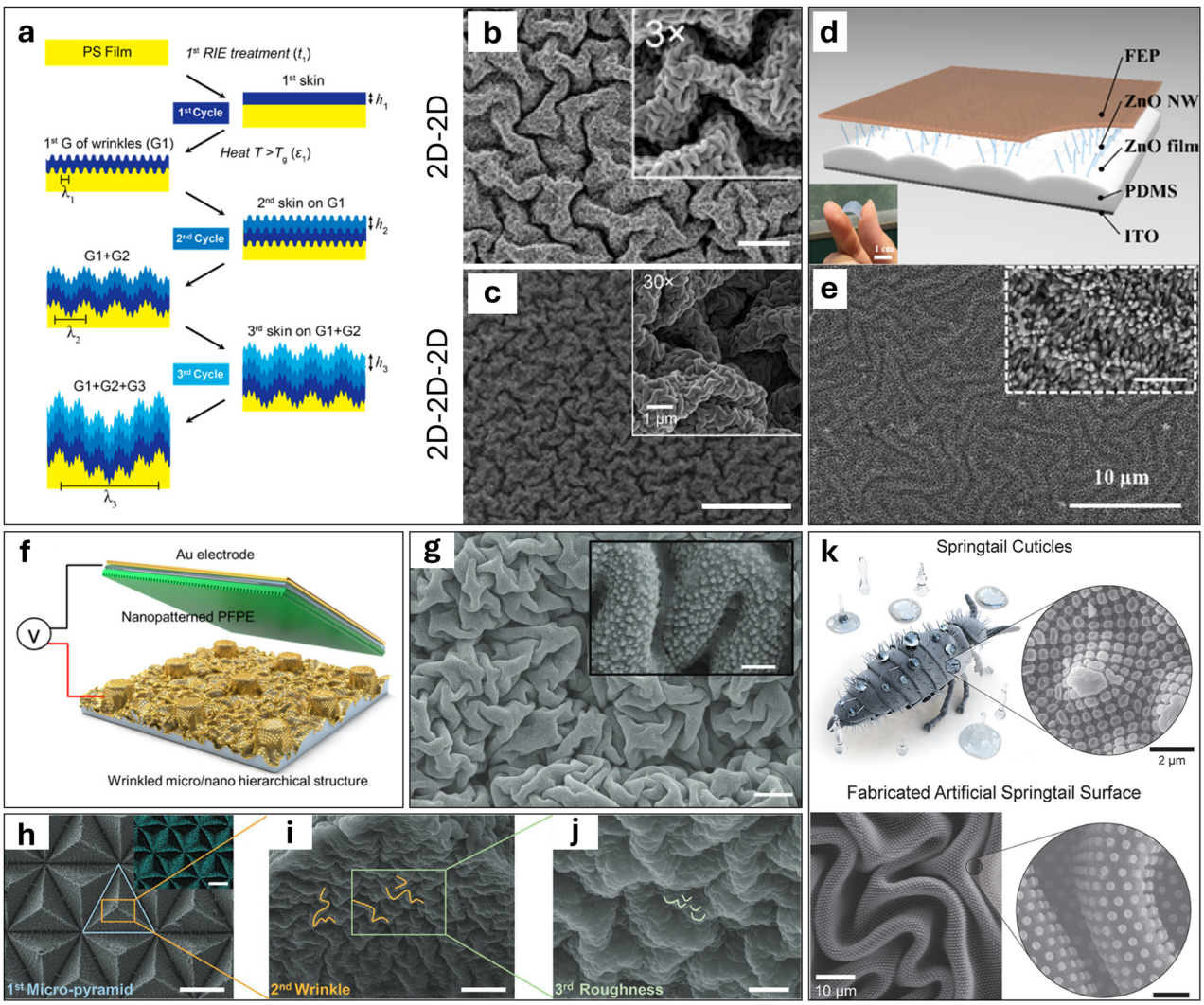

Fig. 23 Hierarchical wrinkle structures and their applications. (a) Sequential wrinkling process diagram showing the formation of multigenerational hierarchical features through controlled CHF_3 RIE plasma treatment and bi-axially relieved strain (2D). (b) and (c) SEM images demonstrating hierarchical wrinkle formation: (b) two-generation structure with different skin thicknesses (scale bar: 3 μm), (b) three-dimensional wrinkle patterns from sequential 2D–2D–2D processing (scale bar: 1 μm). (a)–(c) Adapted with permission.[271] © 2015, American Chemical Society. (d) and (e) PDMS/ZnO nanowire-based pressure sensor design: (d) schematic with the inset showing a flexible film, (e) SEM visualization of the hierarchical surface structure (scale bar: 10 μm). (d) and (e) Adapted with permission.[362] © 2024, American Chemical Society. (f) Schematic illustration of a superhydrophobic triboelectric nanogenerator incorporating wrinkled micro/nano hierarchical structures. Adapted with permission.[363] © 2021, Elsevier. (g) SEM images of a hierarchically structured polystyrene with gold nanoparticles. Scale bars: 1 μm (main image), 100 nm (inset). Adapted with permission.[364] © 2020, Wiley-VCH. (h)–(j) Progressive magnification of hierarchical structures showing: (h) micro-pyramid arrays (scale bar: 100 μm), (i) secondary nano-wrinkles (scale bar: 10 μm), and (j) surface roughness details (scale bar: 2 μm). (h)–(j) Adapted with permission.[365] © 2021, Wiley-VCH. (k) Natural inspiration and biomimetic replication of the springtail cuticle surface showing multi-scale structural features. Scale bar: 2 μm. Adapted with permission.[366] © 2024, American Chemical Society.

Open Access Article. Published on 31 March 2026. Downloaded on 4/22/2026 5:53:25 AM. This article is licensed under a Creative Commons Attribution 3.0 Unported Licence.

stresses overcome film-substrate bonding strength, transforming folds into cracks.[336] For ion irradiation techniques, excessive ion fluence leads to complex patterns and surface cracking.[232] Understanding crack formation mechanisms and their controlling parameters enables both suppression when cracks are detrimental and controlled generation when beneficial.

6.3 Hierarchical structures

Hierarchical structures featuring multiple length scales have garnered significant attention in both natural and engineered systems. These architectures typically combine microscale features providing mechanical stability with nanoscale elements imparting specific functionalities. Nature offers numerous examples, from lotus leaves exhibiting self-cleaning properties to gecko feet demonstrating remarkable adhesion capabilities.[350] This has inspired the development of engineered surfaces for applications ranging from metamaterials to drag reduction.[351,352]

Harnessing surface wrinkling phenomena has proven effective for generating hierarchical structures with highly dense curved features across multiple length scales.[353] Of particular interest is the formation of multigenerational wrinkles, where careful control of parameters like substrate modulus and film thickness enables creation of structures with multiple ordered generations.[354–358] Odom and coworkers[271] demonstrated the formation of three-dimensional hierarchical structures with up to three generations of wrinkles using sequential cycles of plasma-mediated skin formation on prestrained thermoplastic substrates (Fig. 23a–c). The wavelength and orientation of these wrinkles could be precisely controlled through strain direction and plasma treatment duration, enabling surfaces that transitioned between superhydrophobic and superhydrophilic states. This approach was extended to develop stretchable superhydrophobic surfaces and enhanced catalytic behavior by introducing five generations of wrinkles.[359,360] A recent study demonstrated MXene-based multiscale wrinkled surfaces with capabilities including bacterial inhibition, immune system regulation, and accelerated tissue regeneration.[361]

Recent advances have focused on combining wrinkles with other structural elements to enhance functionality, particularly in energy harvesting applications. Integration of wrinkles with zinc oxide nanowires (ZnO NW) enabled the development of high-performance triboelectric nanogenerators for pressure sensing (Fig. 23d and e).[362] The wrinkled morphology, formed through differential thermal contraction during ZnO deposition, provides increased contact area while nanowires contribute piezoelectric properties. This concept has been further developed to create self-healing triboelectric devices by incorporating self-healable PDMS matrices.[367] Superhydrophobic hierarchical structures combining wrinkled carbon nanotube networks with hydrogel matrices have also been developed for electronic skin applications, achieving stable water repellency (contact angles exceeding 156° even under 70% strain) and high sensitivity for underwater wearable sensing.[368] Ahn and coworkers[363] demonstrated integration of micropatterns, nanopatterns, and wrinkles on a single substrate (Fig. 23f) through a combination of nanotransfer, molding, and buckling effects. This allowed independent control of features at each scale and resulted in significantly enhanced triboelectric effects.

Controlled formation of hierarchical structures has also enabled significant advances in surface wettability. One approach combines nanoparticle deposition with wrinkles, where gold nanoparticles deposited on polystyrene films generate liquid-repellent surfaces that effectively suppress blood adhesion (Fig. 23g).[364] Another strategy involves creating micropyramid arrays through prepatterning followed by plasma treatment of fluorocarbon coatings, achieving robust superhydrophobicity with contact angles up to 172° and excellent resistance to mechanical abrasion (Fig. 23h–j).[365] Drawing inspiration from nature, significant efforts have focused on replicating springtail skin for its exceptional omniphobic properties.[369,370] By incorporating serif-T nanostructures (mushroom-shaped features) with wrinkles (Fig. 23k), Yun and coworkers[366] achieved remarkable repellency against low surface tension liquids, demonstrating contact angles exceeding 160° with ethanol. These developments in hierarchical structuring have extended to transparent thermal management, incorporation of quantum dots, and improved optical performance in quantum dot light-emitting diodes (QLEDs), highlighting the versatility of these approaches across diverse applications.[371,372]

7 Conclusions and outlook

Isotropic wrinkling patterns emerge through various formation mechanisms, and a range of fabrication approaches can be employed for their predictive design, tailored for a plethora of growing applications. In this review, we briefly reviewed the fundamentals governing wrinkle formation in bilayer systems, where mismatch in mechanical properties between a stiff film and a compliant substrate leads to surface patterns under compressive stress. The theoretical framework, rooted in energy minimization and force balance principles, establishes relationships between material properties and pattern characteristics. Geometric considerations involving Gaussian curvature explain why labyrinthine patterns, composed of locally one-dimensional segments arranged in zigzag networks, emerge as the energetically favorable morphology under isotropic compression.

Characterized by their labyrinthine morphology with short-range order but long-range disorder, isotropic wrinkling emerges as the default morphology under nondirectional stress conditions. Their prevalence across diverse experimental systems and length scales makes understanding their formation and control essential for a range of surface patterning technologies. We categorize fabrication approaches based on a stress induction mechanism: thermal methods including metal deposition, thermal annealing, plasma oxidation, temperature-responsive chemical reactions, and laser irradiation; light-based approaches spanning UV, visible, and NIR wavelengths; solvent-driven techniques encompassing liquid swelling, vapor exposure, and drying; mechanical approaches including biaxial, multi-axial,

Open Access Article. Published on 31 March 2026. Downloaded on 4/22/2026 5:53:25 AM. This article is licensed under a Creative Commons Attribution 3.0 Unported Licence.

and non-planar strain configurations; chemical methods *via* vapor deposition, ion irradiation, and pH modulation; and electrical strategies through dielectric instability and electrophoresis. Each approach offers distinct advantages in processability, pattern tunability, and material compatibility, enabling the selection of suitable strategies for specific applications.

Quantitative characterization of isotropic wrinkling patterns presents challenges compared to unidirectional (*e.g.*, striped) pattern counterparts. While cross-sectional analysis (normal to pattern orientation) applies to small regions of local alignment, the complex morphology of isotropic wrinkling demands more sophisticated approaches, analogous to those employed in the liquid crystals, ferromagnetic and superconducting films, or block-copolymer thin films. We thus considered, in addition to real- and reciprocal-space techniques, a range of spatial correlation analysis, including persistence length determination, orientation distribution analysis, fractal dimension calculations, defect type and density quantification, and convex hull analysis. Computational modeling through finite element simulations has provided valuable insights into pattern selection, coarsening dynamics, and energetic landscapes, complementing experimental observations and validating analytical predictions. A number of straightforward questions remain unanswered, including: are wavelength distributions in isotropic wrinkles equilibrium features, or rather the result of local minima or long-lived transient states? What dictates the size, shape, and distribution of locally-ordered domains? How are these related to pattern (line and point) defects, and how do these depend on material properties and inhomogeneities? How can 'isotropic' patterns be spatially modulated by external fields, encoding of material properties or defects? Can hybrid machine learning approaches and automated classification reveal underlying governing physics of pattern assembly in isotropic wrinkling, or are further data needed in well-controlled environments and with greater statistics and repeatability? To date, a universally accepted framework to describe and classify isotropic wrinkling patterns has not yet emerged, and we hope that our review will stimulate further computational and experimental efforts in this area.

The versatility of isotropic wrinkled surfaces has led to numerous applications, and we have illustrated a few representative domains including anti-counterfeiting through unique identification patterns exploiting minutiae features analogous to human fingerprints, adaptive camouflage utilizing dynamic wrinkle formation and erasure for on-demand visibility control, multifunctional electronic skins combining sensing with visual feedback for healthcare applications, water-repellent sensors maintaining functionality under mechanical deformation, and enhanced membrane separation with significantly improved water permeance and selectivity. Higher order patterns and failure modes, including creases, folds, or cracks, can lead to either limiting factors or exploitable features, and hierarchical structures combining multiple length scales can indeed enhance functionality in applications ranging from energy harvesting to liquid repellency. Furthermore, the susceptibility of wrinkling patterns to external fields and, indeed, the environment, has unlocked a range of sensing and encoding applications, and we expect further developments in stimuli-responsive isotropic wrinkling in functional surfaces and interfaces.

The design and fabrication of hybrid materials and composites, including graphene, MXenes, transition metal dichalcogenides, or metal-organic frameworks, also has the potential to unlock unprecedented combinations of mechanical flexibility, electrical conductivity, and optical properties that could expand functional capabilities of wrinkled surfaces. Synergistic integration of these materials with controlled wrinkling strategies could yield superior performance in applications ranging from energy storage and conversion, to flexible electronics, and sensing platforms. Predictive design for performance must however rest on strong theoretical or data-driven foundations. The transition from laboratory experiments to real-world implementation, at scale, presents another significant challenge. Many current fabrication approaches face scalability constraints, durability concerns, and elevated manufacturing costs. Future research should develop scalable manufacturing processes suitable for industrial production while maintaining precise control over wrinkle morphology. This may involve adapting techniques such as roll-to-roll processing, imprinting and pattern transfer, or exploring approaches like additive manufacturing with wrinkle-inducing post-treatments. Integration of isotropic wrinkled surfaces into next-generation devices for healthcare, flexible electronics, sustainable energy harvesting and storage, and emerging biomedical applications (antimicrobial interfaces, tissue engineering scaffolds, drug delivery systems), soft robotics (tactile sensing, actuator components), and beyond, will require interdisciplinary collaboration to address system-level challenges while preserving unique functional properties.

Conflicts of interest

There are no conflicts to declare.

Data availability

No primary research results, software or code have been included and no new data were generated or analysed as part of this review. All figures reproduced or adapted from previously published sources are included with appropriate permissions.

Acknowledgements

ZA thanks the Department of Chemical Engineering, Imperial College London for a PhD scholarship. We acknowledge funding from the European Union (HORIZON-CL4-2021-RESILIENCE-01-20) underwritten by UKRI (InnovateUK 10042469) for the Triple-A-COAT consortium, and EPSRC and P&G for funding the ANTENNA project (EP/V056891/1). JTC thanks the Royal Academy

 This journal is © The Royal Society of Chemistry 2026

Open Access Article. Published on 31 March 2026. Downloaded on 4/22/2026 5:53:25 AM. This article is licensed under a Creative Commons Attribution 3.0 Unported Licence.

of Engineering (RAEng, UK) for funding a Research chair, and the Royal Society (IES/R2/222241) for an international exchange grant.

Notes and references

1 L. M. Pismen, *Patterns and Interfaces in Dissipative dynamics*, Springer, 2006.
2 M. I. Rabinovich, A. B. Ezersky and P. D. Weidman, *The Dynamics of Patterns*, World Scientific, 2000.
3 D. Walgraef, *Spatio-Temporal Pattern Formation: with Examples from Physics, Chemistry, and Materials Science*, Springer Science & Business Media, 2012.
4 M. Cross and H. Greenside, *Pattern Formation and Dynamics in Nonequilibrium Systems*, Cambridge University Press, 2009.
5 P. R. Doob, *The Idea of the Labyrinth from Classical Antiquity through the Middle Ages*, Cornell University Press, 1992.
6 S. Echeverría-Alar and M. G. Clerc, *Phys. Rev. Res.*, 2020, **2**, 042036.
7 B. Reimann, R. Richter and I. Rehberg, *Phys. Rev. E: Stat., Nonlinear, Soft Matter Phys.*, 2002, **65**, 031504.
8 R. H. Siddique, G. Gomard and H. Hölscher, *Nat. Commun.*, 2015, **6**, 6909.
9 S. Lin, N. Chou, D. Bao, G. Zhang, C. Xiong, J. Fang and Y. M. Xie, *Comput. Struct.*, 2023, **276**, 106955.
10 S. Miyazawa, *Sci. Adv.*, 2020, **6**, eabb9107.
11 S. Echeverría-Alar, D. Pinto-Ramos, M. Tlidi and M. G. Clerc, *Phys. Rev. E*, 2023, **107**, 054219.
12 Q. X. Liu, P. M. J. Herman, W. M. Mooij, J. Huisman, M. Scheffer, H. Olff and J. van de Koppel, *Nat. Commun.*, 2014, **5**, 5234.
13 A. K. Leung, K. F. Leong and J. M. Lam, *Curr. Pediatr. Rev.*, 2019, **15**, 170–174.
14 A. Yochelis, Y. Tintut, L. L. Demer and A. Garfinkel, *New J. Phys.*, 2008, **10**, 055002.
15 M. Le Berre, E. Ressayre, A. Tallet, Y. Pomeau and L. Di Menza, *Phys. Rev. E: Stat., Nonlinear, Soft Matter Phys.*, 2002, **66**, 026203.
16 M. G. Clerc, S. Echeverría-Alar and M. Tlidi, *Phys. Rev. E*, 2022, **105**, L012202.
17 G. H. Gunaratne, Q. Ouyang and H. L. Swinney, *Phys. Rev. E: Stat. Phys., Plasmas, Fluids, Relat. Interdiscip. Top.*, 1994, **50**, 2802–2820.
18 C. Bowman and A. C. Newell, *Rev. Mod. Phys.*, 1998, **70**, 289–301.
19 D. A. Egolf, I. V. Melnikov and E. Bodenschatz, *Phys. Rev. Lett.*, 1998, **80**, 3228–3231.
20 Q. Ouyang and H. L. Swinney, *Chaos*, 1991, **1**, 411–420.
21 M. Seul, L. R. Monar, L. O'Gorman and R. Wolfe, *Science*, 1991, **254**, 1616–1618.
22 M. Seul and D. Andelman, *Science*, 1995, **267**, 476–483.
23 S. Jin, Y. Liu, Z. Deng, T. Wang, S. Xu, Y. Chen, X. Jiang, C. Liang, J. Hong, S. W. Cheong and X. Wang, *Adv. Mater.*, 2025, **37**, 2501935.
24 Z. Khattari and T. M. Fischer, *J. Phys. Chem. B*, 2002, **106**, 1677–1683.
25 I. R. Epstein and V. K. Vanag, *Chaos*, 2005, **15**, 047510.
26 P. Oswald, J. Baudry and S. Pirkl, *Phys. Rep.*, 2000, **337**, 67–96.
27 R. E. Rosensweig, M. Zahn and R. Shumovich, *J. Magn. Magn. Mater.*, 1983, **39**, 127–132.
28 M. Boltau, S. Walheim and U. Steiner, *Nature*, 1998, **391**, 877–879.
29 A. M. Turing, *Philos. Trans. R. Soc., B*, 1997, **237**, 37–72.
30 J. H. P. Dawes, *Historia Math.*, 2016, **43**, 49–64.
31 J. Swift and P. C. Hohenberg, *Phys. Rev. A: At., Mol., Opt. Phys.*, 1977, **15**, 319–328.
32 N. Stoop, R. Lagrange, D. Terwagne, P. M. Reis and J. Dunkel, *Nat. Mater.*, 2015, **14**, 337–342.
33 M. C. Cross and P. C. Hohenberg, *Rev. Mod. Phys.*, 1993, **65**, 851–1112.
34 G. Kozyreff and M. Tlidi, *Chaos*, 2007, **17**, 037103.
35 N. N. Hobgood, *Colpophyllia natans (Boulder Brain Coral) entire colony*, 2010, https://commons.wikimedia.org/wiki/File:Colpophyllia_natans_(Boulder_Brain_Coral)_entire_colony.jpg.
36 C. Chap, *Giant Puffer fish skin pattern*, 2012, https://commons.wikimedia.org/wiki/File:Giant_Puffer_fish_skin_pattern.JPG.
37 C. M. González-Henríquez and J. Rodríguez-Hernández, *Wrinkled Polymer Surfaces*, Springer International Publishing, 2019.
38 X. Chen, *Mechanical Self-Assembly: Science and Applications*, Springer Science & Business Media, 2012.
39 J. Rodríguez-Hernández, *Prog. Polym. Sci.*, 2015, **42**, 1–41.
40 W. Montagna, *The Structure and Function of Skin*, Elsevier, 2012.
41 J. Genzer and J. Groenewold, *Soft Matter*, 2006, **2**, 310–323.
42 E. Cerda and L. Mahadevan, *Phys. Rev. Lett.*, 2003, **90**, 074302.
43 S. Jerath, *Structural Stability Theory and Practice: Buckling of Columns, Beams, Plates, and Shells*, John Wiley & Sons, 2020.
44 F. Tardani, W. Neri, C. Zakri, H. Kellay, A. Colin and P. Poulin, *Langmuir*, 2018, **34**, 2996–3002.
45 Y. Takema, Y. Yorimoto, M. Kawai and G. Imokawa, *Br. J. Dermatol.*, 1994, **131**, 641–648.
46 C. L. Huang, Y. Wu, X. He, M. Dersch, X. Zhu and J. S. Popovics, *NDT&E Int.*, 2023, **137**, 102832.
47 M. Ginot, M. d'Ottavio, O. Polit, C. Bouvet and B. Castanié, *Compos. Struct.*, 2021, **273**, 114387.
48 J. M. Rotter, *Shell Buckling and Collapse Analysis for Structural Design*, Springer, 2002.
49 M. Maali, B. Bayrak, M. Kiliç, M. Sagiroglu and A. C. Aydin, *Int. J. Pressure Vessels Piping*, 2021, **191**, 104328.
50 D. Y. Khang, J. A. Rogers and H. H. Lee, *Adv. Funct. Mater.*, 2009, **19**, 1526–1536.
51 J. A. Rogers, T. Someya and Y. Huang, *Science*, 2010, **327**, 1603–1607.
52 E. P. Chan, E. J. Smith, R. C. Hayward and A. J. Crosby, *Adv. Mater.*, 2008, **20**, 711–716.

Open Access Article. Published on 31 March 2026. Downloaded on 4/22/2026 5:53:25 AM. This article is licensed under a Creative Commons Attribution 3.0 Unported Licence.

53 K. Efimenko, J. Finlay, M. E. Callow, J. A. Callow and J. Genzer, *ACS Appl. Mater. Interfaces*, 2009, **1**, 1031–1040.
54 L. Pellegrino, L. S. Kriem, E. S. J. Robles and J. T. Cabral, *ACS Appl. Mater. Interfaces*, 2022, **14**, 31463–31473.
55 W. H. Koo, Y. Zhe and F. So, *Adv. Opt. Mater.*, 2013, **1**, 404–408.
56 L. Tong, W. Zhou, Y. Zhao, X. Yu, H. Wang and P. K. Chu, *Colloids Surf., B*, 2016, **148**, 139–146.
57 J. Y. Chung, A. J. Nolte and C. M. Stafford, *Adv. Mater.*, 2011, **23**, 349–368.
58 G. L. Ferretti, M. Nania, O. K. Matar and J. T. Cabral, *Langmuir*, 2016, **32**, 2199–2207.
59 T. Ohzono, H. Monobe, K. Shiokawa, M. Fujiwara and Y. Shimizu, *Soft Matter*, 2009, **5**, 4658–4664.
60 H. Lama, H. Mao and J. T. Cabral, *Soft Matter*, 2025, **21**, 7125–7134.
61 P. Lei, Y. Bao, L. Gao, W. Zhang, X. Zhu, C. Liu and J. Ma, *Adv. Funct. Mater.*, 2024, **34**, 2313787.
62 A. Tan, L. Pellegrino and J. T. Cabral, *ACS Appl. Polym. Mater.*, 2021, **3**, 5162–5170.
63 A. Tan, Z. Ahmad, P. Vukusic and J. T. Cabral, *Molecules*, 2023, **28**, 1710.
64 N. Bowden, S. Brittain, A. G. Evans, J. W. Hutchinson and G. M. Whitesides, *Nature*, 1998, **393**, 146–149.
65 Z. Huang, W. Hong and Z. Suo, *Phys. Rev. E: Stat., Nonlinear, Soft Matter Phys.*, 2004, **70**, 030601.
66 Z. Y. Huang, W. Hong and Z. Suo, *J. Mech. Phys. Solids*, 2005, **53**, 2101–2118.
67 N. Liu, Q. Sun, Z. Yang, L. Shan, Z. Wang and H. Li, *Adv. Sci.*, 2023, **10**, 2207210.
68 N. Liu, Y. Lu, Z. Li, H. Zhao, Q. Yu, Y. Huang, J. Yang and L. Huang, *Langmuir*, 2024, **40**, 18837–18856.
69 J. D. Forster, H. Noh, S. F. Liew, V. Saranathan, C. F. Schreck, L. Yang, J. G. Park, R. O. Prum, S. G. J. Mochrie, C. S. O'Hern, H. Cao and E. R. Dufresne, *Adv. Mater.*, 2010, **22**, 2939–2944.
70 M. Li, D. Joung, B. Hughes, S. D. Waldman, J. A. Kozinski and D. K. Hwang, *Sci. Rep.*, 2016, **6**, 30463.
71 F. Liu, Q. Wang, F. Zhang, B. Yang, Y. Wu and H. Wang, *J. Environ. Chem. Eng.*, 2025, **13**, 118821.
72 J. B. Kim, P. Kim, N. C. Pégard, S. J. Oh, C. R. Kagan, J. W. Fleischer, H. A. Stone and Y. L. Loo, *Nat. Photonics*, 2012, **6**, 327–332.
73 Y. Chen, M. Kadic, S. Guenneau and M. Wegener, *Phys. Rev. Lett.*, 2020, **124**, 235502.
74 R. Rezakhaniha, A. Agianniotis, J. T. C. Schrauwen, A. Griffa, D. Sage, C. V. C. Bouten, F. N. van de Vosse, M. Unser and N. Stergiopulos, *Biomech. Model. Mechanobiol.*, 2012, **11**, 461–473.
75 C.-M. Chen and S. Yang, *Polym. Int.*, 2012, **61**, 1041–1047.
76 S. Zhong, W. Liang, H. Zhong, Y. Zou, S. Lu, R. Chen, Z. Yuan and X. Chen, *Mater. Today Chem.*, 2025, **47**, 102892.
77 A. Schweikart and A. Fery, *Microchim. Acta*, 2009, **165**, 249–263.
78 S. Yang, K. Khare and P. C. Lin, *Adv. Funct. Mater.*, 2010, **20**, 2550–2564.
79 P. J. Yoo, *Electron. Mater. Lett.*, 2011, **7**, 17–23.
80 H. Hou, J. Yin and X. Jiang, *Acc. Chem. Res.*, 2019, **52**, 1025–1035.
81 M. A. Sarabia-Vallejos, F. E. Cerda-Iglesias, D. A. Pérez-Monje, N. F. Acuña-Ruiz, C. A. Terraza-Inostroza, J. Rodríguez-Hernández and C. M. González-Henríquez, *Polymers*, 2023, **15**, 612.
82 Y. Yang, Y. Liu, Y. Chen, L. Wang and W. Feng, *Adv. Energy Sustainability Res.*, 2024, **5**, 2300289.
83 Y. Zhang, L. Zhang, Z. Ren, W. Liu, L. Xu, H. Ji, J. Sun, Y. Wang, D. Liu and Y. Li, *Nano Res.*, 2025, **18**, 94907725.
84 H. Izawa, *Polym. J.*, 2017, **49**, 759–765.
85 N. R. Visaveliya, C. W. Leishman, K. Ng, N. Yehya, N. Tobar, D. M. Eisele and J. M. Köhler, *Adv. Mater. Interfaces*, 2017, **4**, 1700929.
86 Y. Tan, B. Hu, J. Song, Z. Chu and W. Wu, *Nano-Micro Lett.*, 2020, **12**, 101.
87 Z. Zhang, L. Zhao and J. Shi, *Front. Mech. Eng.*, 2022, **8**, 910415.
88 J. Ahn, H. Han, J. H. Ha, Y. Jeong, Y. Jung, J. Choi, S. Cho, S. Jeon, J.-H. Jeong and I. Park, *Adv. Mater.*, 2024, **36**, 2300871.
89 G. Lee, M. Zarei, Q. Wei, Y. Zhu and S. G. Lee, *Small*, 2022, **18**, 2203491.
90 S. Cui, D. Han, G. Chen, S. Liu, Y. Xu, Y. Yu and L. Peng, *ACS Appl. Mater. Interfaces*, 2024, **17**, 11397–11414.
91 Y. Cui, *IEEE Trans. Electron Devices*, 2016, **63**, 3372–3384.
92 D. Feng, X. Su, R. Chen, H. Chen, Y. Yang, S. Lu, Z. Yuan and X. Chen, *Nano Today*, 2025, **65**, 102843.
93 M. Bullough and Y. Cui, *Soft Matter*, 2012, **8**, 3304–3307.
94 P. C. Lin and S. Yang, *Appl. Phys. Lett.*, 2007, **90**, 241903.
95 H. C. Jeong, H. G. Park, J. H. Lee and D. S. Seo, *ACS Appl. Mater. Interfaces*, 2015, **7**, 23216–23222.
96 A. Chiche, C. M. Stafford and J. T. Cabral, *Soft Matter*, 2008, **4**, 2360.
97 I. D. Rowland and T. N. Howe, *Vitruvius: Ten books on architecture*, Cambridge Univ. Press, Cambridge, 1st edn, 2001.
98 P. van Musschenbroek, *Physicæ Experimentales et Geometricæ*, Samuelem Luchtmans, 1729.
99 L. Euler, *De Curvis Elasticis*, Bousquet, Lausanne, 1744.
100 S. Timoshenko, *History of Strength of Materials*, Dover, 1983.
101 M. A. Biot, *Proc. R. Soc. London, Ser. A*, 1957, **242**, 444–454.
102 M. A. Biot, *Mechanics of Incremental Deformations*, 1965.
103 L. D. Landau, L. P. Pitaevskii, A. M. Kosevich and E. M. Lifshitz, *Theory of Elasticity*, Elsevier, 1959.
104 H. G. Allen, *Analysis and Design of Structural Sandwich Panels*, Elsevier, 1969.
105 R. Huang, *J. Mech. Phys. Solids*, 2005, **53**, 63–89.
106 A. L. Volynskii, S. Bazhenov, O. V. Lebedeva and N. F. Bakeev, *J. Mater. Sci.*, 2000, **35**, 547–554.
107 E. Cerda, K. Ravi-Chandar and L. Mahadevan, *Nature*, 2002, **419**, 579–580.
108 H. Jiang, D. Y. Khang, J. Song, Y. Sun, Y. Huang and J. A. Rogers, *Proc. Natl. Acad. Sci. U. S. A.*, 2007, **104**, 15607–15612.

 This journal is © The Royal Society of Chemistry 2026

Open Access Article. Published on 31 March 2026. Downloaded on 4/22/2026 5:53:25 AM. This article is licensed under a Creative Commons Attribution 3.0 Unported Licence.

109 A. Tan, L. Pellegrino, Z. Ahmad and J. T. Cabral, *Adv. Opt. Mater.*, 2022, **10**, 2200964.
110 J. S. Lee, H. Hong, S. J. Park, S. J. Lee and D. S. Kim, *Microelectron. Eng.*, 2017, **176**, 101–105.
111 A. Das, A. Banerji and R. Mukherjee, *ACS Appl. Mater. Interfaces*, 2017, **9**, 23255–23262.
112 S. Yu, L. Ma, Y. Sun, C. Lu, H. Zhou and Y. Ni, *Langmuir*, 2019, **35**, 7146–7154.
113 S. Yu, Y. Ni, L. He and Q. L. Ye, *ACS Appl. Mater. Interfaces*, 2015, **7**, 5160–5167.
114 S. Timoshenko and S. Woinowsky-Krieger, *Theory of Plates and Shells*, McGraw-Hill, 1959.
115 X. Chen and J. W. Hutchinson, *J. Appl. Mech.*, 2004, **71**, 597–603.
116 M. Nania, F. Foglia, O. K. Matar and J. T. Cabral, *Nanoscale*, 2017, **9**, 2030–2037.
117 J. Y. Chung, A. J. Nolte and C. M. Stafford, *Adv. Mater.*, 2009, **21**, 1358–1362.
118 L. Pellegrino, A. Tan and J. T. Cabral, *Phys. Rev. Lett.*, 2022, **128**, 058001.
119 L. Pellegrino, S. Khodaparast and J. T. Cabral, *Soft Matter*, 2020, **16**, 595–603.
120 B. A. Glatz, M. Tebbe, B. Kaoui, R. Aichele, C. Kuttner, A. E. Schedl, H.-W. Schmidt, W. Zimmermann and A. Fery, *Soft Matter*, 2015, **11**, 3332–3339.
121 S. Nikravesh and Y. L. Shen, *Nanomaterials*, 2022, **12**, 3505.
122 E. Flores-Johnson, T. J. Rupert, K. J. Hemker, D. S. Gianola and Y. Gan, *Extreme Mech. Lett.*, 2015, **4**, 175–185.
123 E. A. Matsumoto, D. A. Vega, A. D. Pezzutti, N. A. Garca, P. M. Chaikin and R. A. Register, *Proc. Natl. Acad. Sci. U. S. A.*, 2015, **112**, 12639–12644.
124 M. P. Do Carmo, *Differential Geometry of Curves and Surfaces*, Dover, 2016.
125 B. Audoly and Y. Pomeau, *Elasticity and Geometry*, World Scientific, 2000.
126 C. F. Gauss, *Disquisitiones Generales Circa Superficies Curvas*, Dieterich, 1828.
127 Y. Xia and G. M. Whitesides, *Angew. Chem., Int. Ed.*, 1998, **37**, 550–575.
128 Y. Xia, J. A. Rogers, K. E. Paul and G. M. Whitesides, *Chem. Rev.*, 1999, **99**, 1823–1848.
129 B. D. Gates, Q. Xu, M. Stewart, D. Ryan, C. G. Willson and G. M. Whitesides, *Chem. Rev.*, 2005, **105**, 1171–1196.
130 S. Li, J. Zhang, J. He, W. Liu, Y. Wang, Z. Huang, H. Pang and Y. Chen, *Adv. Sci.*, 2023, **10**, 2304506.
131 P. J. Yoo and H. H. Lee, *Macromolecules*, 2005, **38**, 2820–2831.
132 E. P. Chan, S. Kundu, Q. Lin and C. M. Stafford, *ACS Appl. Mater. Interfaces*, 2011, **3**, 331–338.
133 H. Hou, J. Yin and X. Jiang, *Adv. Mater.*, 2016, **28**, 9126–9132.
134 N. Bowden, W. T. S. Huck, K. E. Paul and G. M. Whitesides, *Appl. Phys. Lett.*, 1999, **75**, 2557–2559.
135 Z. Ahmad, G. Tyagi, S. Xiang, J. Heng, P. Patrcio, P. I. Teixeira, C. M. Stafford, J. F. Douglas and J. T. Cabral, *Adv. Funct. Mater.*, 2025, **35**, 2509167.
136 S. Yu, Y. Guo, H. Li, C. Lu, H. Zhou and L. Li, *ACS Appl. Mater. Interfaces*, 2022, **14**, 11989–11998.
137 S. Yu, Y. Sun, Y. Ni, X. Zhang and H. Zhou, *ACS Appl. Mater. Interfaces*, 2016, **8**, 5706–5714.
138 S. A. Raut, N. Vinx, D. Tromont, P. Leclère, D. Cossement, R. Snyders and D. Thiry, *Langmuir*, 2024, **40**, 14633–14640.
139 F. Wang, S. Xiao, S. Luo, Y. Fu, B. H. Skallerud, H. Kristiansen, M. Cui, C. Zhong, S. Liu, Y. Zhuo, J. He and Z. Zhang, *ACS Appl. Nano Mater.*, 2023, **6**, 4097–4104.
140 Y. Shao and M. A. Brook, *J. Mater. Chem.*, 2010, **20**, 8548–8556.
141 M. D. Casper, A. Gözen, M. D. Dickey, J. Genzer and J. P. Maria, *Soft Matter*, 2013, **9**, 7797–7803.
142 P. Yoo, K. Suh, S. Park and H. Lee, *Adv. Mater.*, 2002, **14**, 1383–1387.
143 P. J. Yoo, K. Y. Suh, H. Kang and H. H. Lee, *Phys. Rev. Lett.*, 2004, **93**, 034301.
144 P. J. Yoo and H. H. Lee, *Langmuir*, 2008, **24**, 6897–6902.
145 T. Okayasu, H. L. Zhang, D. G. Bucknall and G. A. D. Briggs, *Adv. Funct. Mater.*, 2004, **14**, 1081–1088.
146 E. P. Chan, K. A. Page, S. H. Im, D. L. Patton, R. Huang and C. M. Stafford, *Soft Matter*, 2009, **5**, 4638–4641.
147 P. J. Yoo and H. H. Lee, *Phys. Rev. Lett.*, 2003, **91**, 154502.
148 F. Iacopi, S. H. Brongersma and K. Maex, *Appl. Phys. Lett.*, 2003, **82**, 1380–1382.
149 J. Kim and H. H. Lee, *J. Polym. Sci., Part B: Polym. Phys.*, 2001, **39**, 1122–1128.
150 E. P. Chan, Q. Lin and C. M. Stafford, *J. Polym. Sci., Part B: Polym. Phys.*, 2012, **50**, 1556–1561.
151 J.-Y. Park, H. Y. Chae, C.-H. Chung, S. J. Sim, J. Park, H. H. Lee and P. J. Yoo, *Soft Matter*, 2010, **6**, 677–684.
152 N. M. Hoinka, C. Ostwald and T. Fuhrmann-Lieker, *Sci. Rep.*, 2020, **10**, 1–8.
153 S. Nagashima, W. Uchiyama, S. Hayashi, S. Matsubara and D. Okumura, *Mech. Eng. J.*, 2024, **11**, 24–00350.
154 F. Fringuelli and A. Taticchi, *The Diels–Alder Reaction: Selected Practical Methods*, John Wiley & Sons, 2002.
155 F. A. Bayley, J. L. Liao, P. N. Stavrinou, A. Chiche and J. T. Cabral, *Soft Matter*, 2014, **10**, 1155.
156 M. Nania, O. K. Matar and J. T. Cabral, *Soft Matter*, 2015, **11**, 3067–3075.
157 K. Efimenko, W. E. Wallace and J. Genzer, *J. Colloid Interface Sci.*, 2002, **254**, 306–315.
158 D. B. H. Chua, H. T. Ng and S. F. Y. Li, *Appl. Phys. Lett.*, 2000, **76**, 721–723.
159 A. Tserepi, E. Gogolides and K. Tsougeni, *J. Appl. Phys.*, 2005, **98**, 113502.
160 K. Tsougeni, A. Tserepi, G. Boulousis, V. Constantoudis and E. Gogolides, *Plasma Processes Polym.*, 2007, **4**, 398–405.
161 H. T. Evensen, H. Jiang, K. W. Gotrik, F. Denes and R. W. Carpick, *Nano Lett.*, 2009, **9**, 2884–2890.
162 A. Tserepi, E. Gogolides, V. Constantoudis, G. Cordoyiannis, I. Raptis and E. S. Valamontes, *J. Adhes. Sci. Technol.*, 2003, **17**, 1083–1091.
163 Y. Xiang, B. Dejkoski, P. Fulmek and U. Schmid, *Polymer*, 2023, 125915.

Open Access Article. Published on 31 March 2026. Downloaded on 4/22/2026 5:53:25 AM. This article is licensed under a Creative Commons Attribution 3.0 Unported Licence.

164 G. Nasti, S. Sanchez, I. Gunkel, S. Balog, B. Roose, B. D. Wilts, J. Teuscher, G. Gentile, P. Cerruti, V. Ambrogi, C. Carfagna, U. Steiner and A. Abate, *Soft Matter*, 2017, **13**, 1654–1659.
165 D. Gerchman, P. H. Acunha Ferrari, O. Baranov, I. Levchenko, A. S. Takimi and K. Bazaka, *J. Colloid Interface Sci.*, 2024, **668**, 319–334.
166 K. Mondal, Y. Liu, T. Shay, J. Genzer and M. D. Dickey, *ACS Appl. Polym. Mater.*, 2020, **2**, 1848–1855.
167 X. Wang, K. Hu, J. Wang, X. Han, X. Li, F. Xu, Y. Cao and C. Lu, *Adv. Funct. Mater.*, 2024, 2418881.
168 C. Xue, Y. Zhang, L. Li, Y. Hu, C. Chen, Y. Song, H. You, R. Li, J. Li, D. Wu and J. Chu, *ACS Appl. Mater. Interfaces*, 2021, **13**, 23210–23219.
169 D. Chandra and A. J. Crosby, *Adv. Mater.*, 2011, **23**, 3441–3445.
170 H. Zhang, X. Feng, Y. Wu and Z. Wu, *Prog. Org. Coat.*, 2024, **197**, 108856.
171 H. Hou, F. Li, Z. Su, J. Yin and X. Jiang, *J. Mater. Chem. C*, 2017, **5**, 8765–8773.
172 B. Wang, J. Wang, X. Han and C. Lu, *Coatings*, 2022, **12**, 608.
173 C. Zong, Y. Zhao, H. Ji, X. Han, J. Xie, J. Wang, Y. Cao, S. Jiang and C. Lu, *Angew. Chem., Int. Ed.*, 2016, **55**, 3931–3935.
174 F. Li, H. Hou, J. Yin and X. Jiang, *Sci. Adv.*, 2018, **4**, eaar5762.
175 W. Yuan, X. Deng, Z. Wang, T. Ma, S. Yan, X. Gao, J. Li, X. Ma, J. Yin, K. Hu, W. Zhang and X. Jiang, *Adv. Mater.*, 2024, **36**, 2400849.
176 P. Kim, M. Abkarian and H. A. Stone, *Nat. Mater.*, 2011, **10**, 952–957.
177 M. Li, N. Hakimi, R. Perez, S. Waldman, J. A. Kozinski, D. Kun Hwang, M. Li, N. Hakimi, R. Perez, S. Waldman, D. K. Hwang, S. Waldman Li Ka and J. A. Kozinski, *Adv. Mater.*, 2015, **27**, 1880–1886.
178 S. K. Park, Y. J. Kwark, S. Nam, J. Moon, D. W. Kim, S. Park, B. Park, S. Yun, J. I. Lee, B. Yu and K. U. Kyung, *Mater. Lett.*, 2017, **199**, 105–109.
179 H. Zhang and Z. Wu, *RSC Adv.*, 2022, **12**, 33945–33954.
180 H. Zhang, X. Feng, Y. Wu and Z. Wu, *Prog. Org. Coat.*, 2024, **189**, 108241.
181 J. Wang, Q. Shao, W. Wang, Z. Ma, L. Wu, R. Song, H. Liang, Y. Dong, M. Tahir, Z. Hu, X. Huang and L. He, *Chem. Eng. J.*, 2024, **498**, 155679.
182 D. Wang, L. Xu, L. Zhang, L. Zhang and A. Zhang, *Chem. Eng. J.*, 2021, **420**, 127679.
183 J. Bai, K. Hu, L. Zhang, Z. Shi, W. Zhang, J. Yin and X. Jiang, *Macromolecules*, 2022, **55**, 3563–3572.
184 R. Xu, T. Ma, J. Li, S. Dong, S. Zhou, W. Yuan, S. Yan, Y. Quan, M. Xu, K. Li, J. Qian and X. Jiang, *ACS Nano*, 2025, **19**, 33510–33522.
185 Y. Tokudome, K. Suzuki, T. Kitanaga and M. Takahashi, *Sci. Rep.*, 2012, **2**, 683.
186 D. Yamaoka, M. Hara, S. Nagano and T. Seki, *Macromolecules*, 2015, **48**, 908–914.
187 J. Wang, J. Xie, C. Zong, X. Han, J. Zhao, S. Jiang, Y. Cao, A. Fery and C. Lu, *ACS Appl. Mater. Interfaces*, 2017, **9**, 37402–37410.
188 X. Han, Y. Xu, Y. Han, Y. Wang, J. Wang, X. Li, F. Wu, B. Wang and C. Lu, *Polym. Degrad. Stab.*, 2024, **228**, 110924.
189 J. Bai, Z. Shi, X. Ma, J. Yin and X. Jiang, *Macromol. Rapid Commun.*, 2022, **43**, 2200055.
190 L. Xu, U. Azhar, Z. Chen, Q. Niu, J. Chen, X. Zhao, S. Zhang and C. Zong, *RSC Adv.*, 2020, **10**, 3416–3423.
191 C. Zong, U. Azhar, C. Zhou, J. Wang, L. Zhang, Y. Cao, S. Zhang, S. Jiang and C. Lu, *Langmuir*, 2019, **35**, 2601–2609.
192 L. Yuan, J. Chen, Y. Li, G. Luo, Z. Gao, C. Zhou, H. Li, P. Xu and C. Zong, *Langmuir*, 2023, **39**, 2787–2796.
193 L. Zhang and X. Jiang, *Adv. Funct. Mater.*, 2024, **34**, 2408932.
194 E. Liu, L. Li, J. Wang, X. Han, X. Li, F. Xu, Y. Cao and C. Lu, *Adv. Funct. Mater.*, 2023, **33**, 2300182.
195 L. Zhou, L. Yang, Y. Liu, Z. Xu, J. Yin, D. Ge and X. Jiang, *Adv. Opt. Mater.*, 2020, **8**, 2000234.
196 T. Ma, J. Bai, T. Li, S. Chen, X. Ma, J. Yin and X. Jiang, *Proc. Natl. Acad. Sci. U. S. A.*, 2021, **118**, e2114345118.
197 T. Tanaka, S.-T. Sun, Y. Hirokawa, S. Katayama, J. Kucera, Y. Hirose and T. Amiya, *Nature*, 1987, **325**, 796–798.
198 E. P. Chan and A. J. Crosby, *Soft Matter*, 2006, **2**, 324.
199 H. S. Kim and A. J. Crosby, *Adv. Mater.*, 2011, **23**, 4188–4192.
200 S. Zeng, R. Li, S. G. Freire, V. M. M. Garbellotto, E. Y. Huang, A. T. Smith, C. Hu, W. R. T. Tait, Z. Bian, G. Zheng, D. Zhang and L. Sun, *Adv. Mater.*, 2017, **29**, 1700828.
201 H. J. Bae, S. Bae, C. Park, S. Han, J. Kim, L. N. Kim, K. Kim, S. H. Song, W. Park and S. Kwon, *Adv. Mater.*, 2015, **27**, 2083–2089.
202 M. Guvendiren, S. Yang and J. A. Burdick, *Adv. Funct. Mater.*, 2009, **19**, 3038–3045.
203 M. Guvendiren and J. A. Burdick, *Biomaterials*, 2010, **31**, 6511–6518.
204 A. Gallardo, N. Lujan, H. Reinecke, C. García, A. D. Campo and J. Rodriguez-Hernandez, *Langmuir*, 2017, **33**, 1614–1622.
205 E. Martinez-Campos, A. Gallardo, N. Lujan, A. Santos-Coquillat, H. Reinecke, A. D. Campo and J. Rodriguez-Hernandez, *ACS Appl. Bio Mater.*, 2019, **2**, 654–664.
206 J. Gu, X. Li, H. Ma, Y. Guan and Y. Zhang, *Polymer*, 2017, **110**, 114–123.
207 Y. F. Chuang, M. K. Wei, F. Yang and S. Lee, *J. Polym. Res.*, 2021, **1**, 3.
208 E. P. Chan and A. J. Crosby, *Adv. Mater.*, 2006, **18**, 3238–3242.
209 K. Wu, Y. Sun, H. Yuan, J. Zhang, G. Liu and J. Sun, *Nano Lett.*, 2020, **20**, 4129–4135.
210 W. Guo, C. M. Reese, L. Xiong, P. K. Logan, B. J. Thompson, C. M. Stafford, A. V. Ievlev, B. S. Lokitz, O. S. Ovchinnikova and D. L. Patton, *Macromolecules*, 2017, **50**, 8670–8677.

 This journal is © The Royal Society of Chemistry 2026

Open Access Article. Published on 31 March 2026. Downloaded on 4/22/2026 5:53:25 AM. This article is licensed under a Creative Commons Attribution 3.0 Unported Licence.

211 C. M. Reese, W. Guo, B. J. Thompson, P. K. Logan, C. M. Stafford and D. L. Patton, *Macromolecules*, 2020, **53**, 4552–4559.
212 D. Breid and A. J. Crosby, *Soft Matter*, 2009, **5**, 425–431.
213 D. Breid and A. J. Crosby, *Soft Matter*, 2011, **7**, 4490–4496.
214 S. K. Basu, A. M. Bergstreser, L. F. Francis, L. E. Scriven and A. V. McCormick, *J. Appl. Phys.*, 2005, **98**, 063507.
215 S. J. Kwon, J.-G. Park and S. H. Lee, *J. Chem. Phys.*, 2004, **122**, 031101.
216 S. Zhu, Y. Liu, W. Guo, J. Fan, X. Jiang and J. Li, *Adv. Funct. Mater.*, 2023, **33**, 2301850.
217 C. M. González-Henríquez, D. H. Sagredo-Oyarce, M. A. Sarabia-Vallejos and J. Rodríguez-Hernández, *Polymer*, 2016, **101**, 24–33.
218 C. M. González-Henríquez, D. F. Veliz-Silva, M. A. Sarabia-Vallejos, A. del Campo-García and J. Rodríguez-Hernández, *Molecules*, 2019, **24**, 751.
219 J. Zhu, P. Zhu, H. Sun, X. Zhao, Y. Ye, X. Sun, Z. Yu, Y. Tan and F. Jiang, *Adv. Funct. Mater.*, 2026, e10262.
220 H. Izawa, Y. Miyazaki, T. Yonemura, N. Ito, Y. Okamoto, S. Ifuku, M. Morimoto and H. Saimoto, *Polym. J.*, 2019, **51**, 675–683.
221 J. Lee, H. Park, S. Kim, C. Liu, Z. Li and K. Sim, *Nat. Commun.*, 2025, **16**, 2225.
222 J. Yin, J. L. Yagüe, D. Eggenspieler, K. K. Gleason and M. C. Boyce, *Adv. Mater.*, 2012, **24**, 5441–5446.
223 Q. Wang, W. Wang, C. Lu, L. Hu, Y. Ni and S. Yu, *Extreme Mech. Lett.*, 2024, **68**, 102145.
224 R. Li, H. Yi, X. Hu, L. Chen, G. Shi, W. Wang and T. Yang, *Sci. Rep.*, 2013, **3**, 1–6.
225 J. Yin, J. L. Yagüe, M. C. Boyce and K. K. Gleason, *ACS Appl. Mater. Interfaces*, 2014, **6**, 2850–2857.
226 Q. Wang, S. Yu, Q. Ye, B. Yang, Y. Zhang, X. Wang and L. Li, *Langmuir*, 2024, **40**, 2102–2110.
227 H. Li, B. Sheng, H. Wu, Y. Huang, D. Zhang and S. Zhuang, *Materials*, 2018, **11**, 1571.
228 R. N. Enright and L. C. Bradley, *Adv. Funct. Mater.*, 2022, **32**, 2204887.
229 M. Kim, L. C. Bradley and A. J. Crosby, *ACS Appl. Polym. Mater.*, 2025, **7**, 7072–7078.
230 P. Christian, H. M. A. Ehmann, O. Werzer and A. M. Coclite, *Soft Matter*, 2016, **12**, 9501–9508.
231 Y. C. Chen, Y. W. Luo, C. Y. Huang, Y. L. Li, T. L. Chen, T. Y. Xu and H. Y. Hsueh, *Small*, 2024, **20**, 2311679.
232 M. W. Moon, S. H. Lee, J. Y. Sun, K. H. Oh, A. Vaziri and J. W. Hutchinson, *Scr. Mater.*, 2007, **57**, 747–750.
233 J. Won, H. C. Jeong, J. H. Lee, D. H. Kim, D. W. Lee, B. Y. Oh, Y. Liu and D. S. Seo, *Langmuir*, 2020, **36**, 3952–3957.
234 M. Yang, S. Chen, Z. Zhang, L. Cheng, J. Zhao, R. Bai, W. Wang, W. Gao, W. Yu, X. Jiang and X. Yan, *Nat. Commun.*, 2024, **15**, 5760.
235 M. Aghito, G. Hernandéz Rodríguez, C. Antonini and A. M. Coclite, *Langmuir*, 2024, **40**, 13017–13024.
236 F. Muralter, A. M. Coclite and O. Werzer, *J. Phys. Chem. C*, 2019, **123**, 24165–24171.
237 Y. Rahmawan, M. W. Moon, K. S. Kim, K. R. Lee and K. Y. Suh, *Langmuir*, 2010, **26**, 484–491.
238 P. Samyn, M. P. Laborie, A. P. Mathew, A. Airoudj, H. Haidara and V. Roucoules, *Langmuir*, 2012, **28**, 1427–1438.
239 S. M. George, *Chem. Rev.*, 2010, **110**, 111–131.
240 G. Wang, Z. Wang, J. Ren, Z. Wu and Y. Duan, *npj Flexible Electron.*, 2025, **9**, 94.
241 S. Keren, E. Yachnin, N. Cohen and T. Segal-Peretz, *ACS Appl. Mater. Interfaces*, 2025, **17**, 34529–34537.
242 G. S. Sodhi and J. Kaur, *Forensic Sci. Int.*, 2001, **120**, 172–176.
243 M.-W. Moon, S. H. Lee, J.-Y. Sun, K. H. Oh, A. Vaziri and J. W. Hutchinson, *Proc. Natl. Acad. Sci. U. S. A.*, 2007, **104**, 1130–1133.
244 S. Lee, E. Byeon, S. Jung and D.-G. Kim, *Sci. Rep.*, 2018, **8**, 14063.
245 P. Kumar, D. Rani, S. Bera, M. Sabapathy and S. Sarkar, *Appl. Surf. Sci.*, 2025, **692**, 162677.
246 J. H. Lee, H. C. Jeong, J. Won, D. H. Kim, D. W. Lee, I. H. Song, J. Y. Oh, D. H. Kim, Y. Liu and D. S. Seo, *J. Phys. Chem. C*, 2020, **124**, 8378–8385.
247 S. Faruque Ahmed, S. Nagashima, J. Y. Lee, K. R. Lee, K. S. Kim and M. W. Moon, *Carbon*, 2014, **76**, 105–112.
248 S. F. Ahmed, G. H. Rho, K. R. Lee, A. Vaziri and M. W. Moon, *Soft Matter*, 2010, **6**, 5709–5714.
249 H. G. Park, H. C. Jeong, Y. H. Jung and D. S. Seo, *Sci. Rep.*, 2015, **5**, 12356.
250 P. Siriworakoonchai, N. Pussadee and C. Chaiwong, *Plasma Chem. Plasma Process.*, 2023, **43**, 315–327.
251 H. C. Jeong, H. G. Park, J. H. Lee, Y. H. Jung, S. B. Jang and D. S. Seo, *Sci. Rep.*, 2015, **5**, 8641.
252 T. K. Shih, J. R. Ho, C. F. Chen, W. T. Whang and C. C. Chen, *Appl. Surf. Sci.*, 2007, **253**, 9381–9386.
253 M. Watanabe and K. Mizukami, *Macromolecules*, 2012, **45**, 7128–7134.
254 T. Ma, T. Li, L. Zhou, X. Ma, J. Yin and X. Jiang, *Nat. Commun.*, 2020, **11**, 1811.
255 S. Yan, M. Yang, X. Deng, G. Liu, X. Gao, S. Chen, L. Cheng, T. Li, T. Ma, M. Xu, J. Li, Z. Zhang, L. Yang, W. Yu, X. Yan and X. Jiang, *J. Am. Chem. Soc.*, 2025, **147**, 12766–12776.
256 E. Schäffer, T. Thurn-Albrecht, T. P. Russell and U. Steiner, *Nature*, 2000, **403**, 874–877.
257 Q. Wang, M. Tahir, J. Zang and X. Zhao, *Adv. Mater.*, 2012, **24**, 1947–1951.
258 Q. Wang and X. Zhao, *Phys. Rev. E: Stat., Nonlinear, Soft Matter Phys.*, 2013, **88**, 042403.
259 R. Huang, *Appl. Phys. Lett.*, 2005, **87**, 151911.
260 D. van den Ende, J. D. Kamminga, A. Boersma, T. Andritsch and P. G. Steeneken, *Adv. Mater.*, 2013, **25**, 3438–3442.
261 I.-T. Lin, Y. S. Choi, C. Wojcik, T. Wang, S. Kar-Narayan and S. K. Smoukov, *Mater. Today*, 2020, **41**, 51–61.
262 M. Kato, Y. Tsuboi, A. Kikuchi and T. A. Asoh, *J. Phys. Chem. B*, 2016, **120**, 5042–5046.
263 M. Kato, T.-A. Asoh and H. Uyama, *Chem. Commun.*, 2019, **55**, 4170–4173.

Open Access Article. Published on 31 March 2026. Downloaded on 4/22/2026 5:53:25 AM. This article is licensed under a Creative Commons Attribution 3.0 Unported Licence.

264 T.-A. Asoh and Y. Kashihara, *Adv. Mater. Interfaces*, 2025, **12**, e00555.
265 K. Tsougeni, A. Tserepi, G. Boulousis, V. Constantoudis and E. Gogolides, *Jpn. J. Appl. Phys.*, 2007, **46**, 744–750.
266 Z. Ahmad, B. P. M. R, H. Barr and J. T. Cabral, *Nano Lett.*, 2024, **25**, 740–746.
267 C. Harrison, C. M. Stafford, W. Zhang and A. Karim, *Appl. Phys. Lett.*, 2004, **85**, 4016–4018.
268 C. M. Stafford, C. Harrison, K. L. Beers, A. Karim, E. J. Amis, M. R. VanLandingham, H.-C. Kim, W. Volksen, R. D. Miller and E. E. Simonyi, *Nat. Mater.*, 2004, **3**, 545–550.
269 S. Cai, D. Breid, A. J. Crosby, Z. Suo and J. W. Hutchinson, *J. Mech. Phys. Solids*, 2011, **59**, 1094–1114.
270 J. Groenewold, *Phys. A*, 2001, **298**, 32–45.
271 W. K. Lee, C. J. Engel, M. D. Huntington, J. Hu and T. W. Odom, *Nano Lett.*, 2015, **15**, 5624–5629.
272 A. Guerra, Z. Wang, S. Mathews, A. D. Rey and K. De France, *Langmuir*, 2025, **41**, 25230–25241.
273 T. Ohzono and M. Shimomura, *Phys. Rev. B: Condens. Matter Mater. Phys.*, 2004, **69**, 132202.
274 G. P. Alexander, B. Chen, E. A. Matsumoto and R. D. Kamien, *Rev. Mod. Phys.*, 2012, **84**, 497–514.
275 A. Jangizehi, F. Schmid, P. Besenius, K. Kremer and S. Seiffert, *Soft Matter*, 2020, **16**, 10809–10859.
276 A. Reddy, X. Feng, E. L. Thomas and G. M. Grason, *Macromolecules*, 2021, **54**, 9223–9257.
277 D. Boyer and J. Viñals, *Phys. Rev. E: Stat., Nonlinear, Soft Matter Phys.*, 2001, **64**, 050101.
278 R. E. Jones and G. H. Gunaratne, *J. Stat. Phys.*, 1998, **93**, 427–447.
279 S. K. Basu, A. V. McCormick and L. E. Scriven, *Langmuir*, 2006, **22**, 5916–5924.
280 S. H. Im and R. Huang, *J. Appl. Mech.*, 2005, **72**, 955–961.
281 R. Huang and S. H. Im, *Phys. Rev. E: Stat., Nonlinear, Soft Matter Phys.*, 2006, **74**, 026214.
282 A. Cutolo, V. Pagliarulo, F. Merola, S. Coppola, P. Ferraro and M. Fraldi, *Mater. Des.*, 2020, **187**, 108314.
283 S. Nikravesh, D. Ryu and Y. L. Shen, *Sci. Rep.*, 2021, **11**, 16449.
284 S. Seok, H. Park and J. Kim, *Micromachines*, 2024, **15**, 543.
285 J. Zavodnik and M. Brojan, *Comput. Methods Appl. Mech. Eng.*, 2025, **433**, 117529.
286 Y. F. Lai, J. Y. Ho, J. R. Chen, Y. F. Tsai and H. Y. Hsueh, *ACS Appl. Mater. Interfaces*, 2025, **17**, 54314–54324.
287 R. Dantinne, S. A. Raut, A. Chauvin, C. Bittencourt, P. Leclère and D. Thiry, *ACS Appl. Nano Mater.*, 2025, **8**, 18008–18017.
288 A. Kumar, N. Thomas and P. Swaminathan, *ACS Appl. Nano Mater.*, 2025, **8**, 4625–4635.
289 S. Swaminathan, M. Bullough, Q. Li, A. Zhou and Y. Cui, *J. R. Soc. Interface*, 2014, **11**, 20130893.
290 A. Beber, C. Taveneau, M. Nania, F.-C. Tsai, A. Di Cicco, P. Bassereau, D. Lévy, J. T. Cabral, H. Isambert, S. Mangenot and A. Bertin, *Nat. Commun.*, 2019, **10**, 420.
291 F. E. Rodríguez-Umanzor, M. N. Alarcón-Núñez, M. A. Sarabia-Vallejos, N. A. Cohn-Inostroza, E. Martínez-Campos, R. Cue-López, J. Rodríguez-Hernández, C. A. Terraza and C. M. González-Henríquez, *Appl. Mater. Today*, 2025, **44**, 102777.
292 S. Y. Ryu, J. H. Seo, H. Hafeez, M. Song, J. Y. Shin, D. H. Kim, Y. C. Jung and C. S. Kim, *J. Phys. Chem. C*, 2017, **121**, 9191–9201.
293 N. Sekine, C.-H. Chou, W. L. Kwan and Y. Yang, *Org. Electron.*, 2009, **10**, 1473–1477.
294 C. S. Chen, P. C. Yang, Y. M. Shen, S.-Y. Ma, S. C. Shiu, S. C. Hung, S. H. Lin and C. F. Lin, *Sol. Energy Mater. Sol. Cells*, 2012, **101**, 180–185.
295 H.-Y. Park, D. Lim, K.-D. Kim and S.-Y. Jang, *J. Mater. Chem. A*, 2013, **1**, 6327–6334.
296 B. J. Richardson, X. Wang, A. Almutairi and Q. Yu, *J. Mater. Chem. A*, 2015, **3**, 5563–5571.
297 B. Osmani, H. Deyhle, T. Töpper, T. Pfohl and B. Müller, *Adv. Mater. Technol.*, 2017, **2**, 1700105.
298 R. Jiang, J. Pu, Y. Wang, J. Chen, G. Fu, X. Chen, J. Yang, J. Shen, X. Sun, J. Ding and X. Xu, *Interdiscip. Mater.*, 2024, **3**, 414–424.
299 T. Kwak, H. Yang, J. Chung, M. Kim, S. Jung, G. Park and F. S. Kim, *Macromol. Res.*, 2024, **33**, 49–55.
300 I. Y. Bu, *Mater. Lett.*, 2014, **122**, 55–57.
301 S. Lei, Z. He, C. Hu, G. Zhang, X. Zhu, J. Li, K. Wang and H. Yu, *Adv. Opt. Mater.*, 2024, **13**, 2401843.
302 C. Zhao, Z. He, Y. Zhou, W. Xiong, L. He, Y. Wu, S. Tan, Z. Zhang, Y. Liu and A. Pan, *Appl. Surf. Sci.*, 2025, **686**, 162214.
303 Z. He, R. Cai, J. Liu, X. Wu, A. Yu, X. Zhu, J. Li, K. Wang, Y. Shi and H. Yu, *Opt. Lett.*, 2025, **50**, 5330–5333.
304 R. Liu, Y. Sun, Y. Sun, H. Li, M. Chen, L. Long, J. Gong, B. Lv and Y. Ni, *Carbohydr. Polym.*, 2024, **334**, 122035.
305 Y. Sun, R. Liu, L. Long and Y. Sun, *Sci. Rep.*, 2024, **14**, 13275.
306 L. Skedung, M. Arvidsson, J. Y. Chung, C. M. Stafford, B. Berglund and M. W. Rutland, *Sci. Rep.*, 2013, **3**, 2617.
307 S. Yan, K. Hu, S. Chen, T. Li, W. Zhang, J. Yin and X. Jiang, *Nat. Commun.*, 2022, **13**, 7434.
308 H. Huang, J. Y. Chung, A. J. Nolte and C. M. Stafford, *Chem. Mater.*, 2007, **19**, 6555–6560.
309 Y. Wang, B. J. Kim, B. Peng, W. Li, Y. Wang, M. Li and F. G. Omenetto, *Proc. Natl. Acad. Sci. U. S. A.*, 2019, **116**, 21361–21368.
310 H. Mao, Z. Ahmad, L. Xin, H. Lama, P. Fan, P. Shields, S. Eyley, W. Thielemans and J. T. Cabral, *ACS Nano*, 2025, **20**, 823–834.
311 J. Yin and M. C. Boyce, *Nature*, 2015, **520**, 164–165.
312 M. Ma, Z. Jiang, T. Ma, X. Gao, J. Li, M. Liu, J. Yan and X. Jiang, *Adv. Funct. Mater.*, 2024, **34**, 2405239.
313 J. T. Cabral and J. S. Higgins, *Prog. Polym. Sci.*, 2018, **81**, 1–21.
314 J. S. Higgins and J. T. Cabral, *Macromolecules*, 2020, **53**, 4137–4140.
315 M. Xie, G. Lin, D. Ge, L. Yang, L. Zhang, J. Yin and X. Jiang, *ACS Mater. Lett.*, 2019, **1**, 77–82.
316 H. C. Guo, J. Chen, B. L. Feng, H. L. Zhang, X.-Y. Yang, L. Wang, P. M. Xu, H. Li and C. Y. Zong, *Chin. J. Polym. Sci.*, 2025, **43**, 1114–1124.
317 K. Liang, W. Feng, Y. Liu, J. Zhang, F. Tian, Y. Yao, X. Jiang and S. Lin, *ACS Appl. Mater. Interfaces*, 2025, **17**, 21866–21874.

 This journal is © The Royal Society of Chemistry 2026

Open Access Article. Published on 31 March 2026. Downloaded on 4/22/2026 5:53:25 AM. This article is licensed under a Creative Commons Attribution 3.0 Unported Licence.

318 L. Phan, R. Kautz, E. M. Leung, K. L. Naughton, Y. Van Dyke and A. A. Gorodetsky, *Chem. Mater.*, 2016, **28**, 6804–6816.
319 R. Hanlon, *Curr. Biol.*, 2007, **17**, R400–R404.
320 Y. Zhang, D. Liu, Z. Ren, W. Liu, B. Wang, S. Song, T. Hao, L. Xu, H. Ji, J. Sun, L. Zhang and Y. Li, *Chem. Eng. J.*, 2024, **499**, 155960.
321 G. Lee, G. Y. Bae, J. H. Son, S. Lee, S. W. Kim, D. Kim, S. G. Lee and K. Cho, *Adv. Sci.*, 2020, **7**, 2001184.
322 H. Guo, Z. Chu, L. Fu, Y. Lv, X. Liu, X. Fan and W. Zhang, *Chem. Eng. J.*, 2024, **495**, 153684.
323 Y. Lv, Z. Chu, D. Huang, X. Fan and W. Zhang, *Small*, 2024, **21**, 2407390.
324 B. N. Sahoo, J. Woo, H. Algadi, J. Lee and T. Lee, *Adv. Mater. Technol.*, 2019, **4**, 1900230.
325 A. Cassie and S. Baxter, *Trans. Faraday Soc.*, 1944, **40**, 546–551.
326 S. Arunachalam, Z. Ahmad, R. Das and H. Mishra, *Adv. Mater. Interfaces*, 2020, **7**, 2001268.
327 L. Xu, S. Shao, X. Lu, D. Wang, A. Zhang and J. Zhang, *Chem. Eng. J.*, 2024, **496**, 153454.
328 Z. Tan, S. Chen, X. Peng, L. Zhang and C. Gao, *Science*, 2018, **360**, 518–521.
329 Z. Li, Y. Xu, L. Shen, R. Li, Y. Jiao, H. Lin and C. Y. Tang, *Desalination*, 2023, **564**, 116801.
330 B. Dai, Y. Hu, Y. Ding, L. Shen, R. Li, D. Zhao, Y. Jiao, Y. Xu and H. Lin, *Desalination*, 2024, **570**, 117083.
331 X. Wang, Y. Yang, Z. Li, T. Li, C. Niu and R. Wang, *J. Membr. Sci.*, 2025, **717**, 123567.
332 J. Yu, L. Zhang, L. Shen, R. Li, D. Zhao, H. Lin, Y. Xu and Y. Jiao, *J. Membr. Sci.*, 2024, **694**, 122413.
333 Q. Wang and X. Zhao, *Sci. Rep.*, 2015, **5**, 8887.
334 R. C. Hayward, B. F. Chmelka and E. J. Kramer, *Macromolecules*, 2005, **38**, 7768–7783.
335 M. H. Essink, M. A. van Limbeek, A. Pandey, S. Karpitschka and J. H. Snoeijer, *Soft Matter*, 2023, **19**, 5160–5168.
336 M. Guvendiren, J. A. Burdick and S. Yang, *Soft Matter*, 2010, **6**, 5795–5801.
337 A. VanZanten, S. Y. Chen, M. M. Driscoll and C. R. Szczepanski, *Soft Matter*, 2024, **20**, 6742–6753.
338 Y. Tokudome, H. Kuniwaki, K. Suzuki, D. Carboni, G. Poologasundarampillai and M. Takahashi, *Adv. Mater. Interfaces*, 2016, **3**, 1500802.
339 P. Kim, Y. Hu, J. Alvarenga, M. Kolle, Z. Suo and J. Aizenberg, *Adv. Opt. Mater.*, 2013, **1**, 381–388.
340 A. K. Epstein, D. Hong, P. Kim and J. Aizenberg, *New J. Phys.*, 2013, **15**, 095018.
341 J. Lee, W. Shim, E. Lee, J. S. Noh and W. Lee, *Angewandte Chemie*, 2011, **123**, 5413–5417.
342 B. Park, J. Kim, D. Kang, C. Jeong, K. S. Kim, J. U. Kim, P. J. Yoo and T. I. Kim, *Adv. Mater.*, 2016, **28**, 8130–8137.
343 D. Huh, K. L. Mills, X. Zhu, M. A. Burns, M. D. Thouless and S. Takayama, *Nat. Mater.*, 2007, **6**, 424–428.
344 K. H. Nam, I. H. Park and S. H. Ko, *Nature*, 2012, **485**, 221–224.
345 R. Seghir and S. Arscott, *Sci. Rep.*, 2015, **5**, 14787.
346 D. Kang, P. V. Pikhitsa, Y. W. Choi, C. Lee, S. S. Shin, L. Piao, B. Park, K. Y. Suh, T. I. Kim and M. Choi, *Nature*, 2014, **516**, 222–226.
347 S. Li, P. Xiao, J. Lin, J. Wu, X. Zhang, J. Li and T. Chen, *Nano Lett.*, 2025, **25**, 15864–15873.
348 N. Y. Adly, H. Hassani, A. Q. Tran, M. Balski, A. Yakushenko, A. Offenhäusser, D. Mayer and B. Wolfrum, *Soft Matter*, 2017, **13**, 6297–6303.
349 J. L. Fritz and M. J. Owen, *J. Adhes.*, 2006, **54**, 33–45.
350 W. G. Bae, H. N. Kim, D. Kim, S. H. Park, H. E. Jeong and K. Y. Suh, *Adv. Mater.*, 2014, **26**, 675–700.
351 J. Henzie, M. H. Lee and T. W. Odom, *Nat. Nanotechnol.*, 2007, **2**, 549–554.
352 Y. C. Jung and B. Bhushan, *ACS Nano*, 2009, **3**, 4155–4163.
353 W. K. Lee and T. W. Odom, *ACS Nano*, 2019, **13**, 6170–6177.
354 S. Yu, Y. Sun, Y. Du and H. Zhou, *Thin Solid Films*, 2018, **660**, 353–357.
355 K. Wu, H. Z. Yuan, S. J. Li, J. Y. Zhang, G. Liu and J. Sun, *Scr. Mater.*, 2019, **162**, 456–459.
356 H. Xu, T. Shi, G. Liao and Q. Xia, *Front. Mech. Eng.*, 2019, **14**, 235–240.
357 E. S. Kim, S. H. Kim, S. J. Lee, J. H. Lee, M. Byeon, D. H. Suh and W. J. Choi, *Polymer*, 2021, **212**, 123087.
358 Y. Yan, C. Wang, Y. He, Q. Zhao, J. Huang, L. Ran, X. Liu, Y. Li and L. Li, *J. Electron. Mater.*, 2025, **54**, 1739–1747.
359 W. K. Lee, W. B. Jung, S. R. Nagel and T. W. Odom, *Nano Lett.*, 2016, **16**, 3774–3779.
360 W. B. Jung, K. M. Cho, W. K. Lee, T. W. Odom and H. T. Jung, *ACS Appl. Mater. Interfaces*, 2018, **10**, 1347–1355.
361 M. Asadi Tokmedash, J. Robins, J. S. VanEpps, M. Kim and J. Min, *Adv. Healthcare Mater.*, 2025, e02451.
362 L. Gu, Y. Wang, M. Yang, H. Xu, W. Zhang, Z. Ren, L. Meng, N. Cui and J. Liu, *ACS Appl. Mater. Interfaces*, 2024, **16**, 3901–3910.
363 J. Ahn, Z. J. Zhao, J. Choi, Y. Jeong, S. Hwang, J. Ko, J. Gu, S. Jeon, J. Park, M. Kang, D. V. Del Orbe, I. Cho, H. Kang, M. Bok, J. H. Jeong and I. Park, *Nano Energy*, 2021, **85**, 105978.
364 S. M. Imani, R. Maclachlan, Y. Chan, A. Shakeri, L. Soleymani and T. F. Didar, *Small*, 2020, **16**, 2004886.
365 W. Zhang, J. Gao, Y. Deng, L. Peng, P. Yi, X. Lai and Z. Lin, *Adv. Funct. Mater.*, 2021, **31**, 2101068.
366 G. T. Yun, Y. Kim, H. Ahn, M. Kim, G. M. Jang, S. G. Im, W. B. Jung and H. T. Jung, *ACS Nano*, 2024, **18**, 5622–5631.
367 J. Liu, J. Xu, Y. Wang, Z. Li, M. Li, N. Cui, F. Zhao, L. Meng and L. Gu, *Chem. Eng. J.*, 2024, **495**, 153601.
368 Y. Ding, Y. Wang, H. Zhang, Z. Jia and J. Wang, *Chem. Eng. J.*, 2025, **520**, 166249.
369 R. Das, S. Arunachalam, Z. Ahmad, E. Manalastas and H. Mishra, *J. Membr. Sci.*, 2019, **588**, 117185.
370 R. Das, Z. Ahmad, J. Nauruzbayeva and H. Mishra, *Sci. Rep.*, 2020, **10**, 7934.
371 D. Guzmán-De La Cerda, P. P. Jofré-Ulloa, E. Benavente, C. González-Henríquez, F. Celis, J. Rodríguez-Hernández, E. Martinez-Campos, G. Vera-Rojas and J. P. Melo-Sanguinetti, *ACS Omega*, 2025, **10**, 3322–3331.
372 S. Li, Z. Liu, X. Pan, H. Wang, M. Li, J. Hu, Y. Ding, Y. Sun and Z. Chen, *ACS Appl. Mater. Interfaces*, 2025, **17**, 6793–6804.